Mathematical Modeling of Mean Flow Stress (MFS) during Hot Strip Rolling for HSLA Steels

by

Faisal Alghamdi

Department of Mining and Materials Engineering

McGill University, Montreal, Canada

December 2013

A thesis submitted to McGill University in partial fulfillment of the requirements of the degree of Master of Science.

ABSTRACT

Based on experimental results using hot torsion, the effect of 'time gap', i.e. the time between roughing and finishing in a hot rolling schedule simulation, on mean flow stress (MFS) behavior for high-strength-low-alloyed (HSLA) steels was investigated. Two types of hot deformation were studied: an 'average' schedule with constant interpass time, in which each pass is identical but the temperature is decreasing at a constant rate throughout the rolling schedule simulation. In this type of schedule, two different interpass times of 5 and 30 seconds were used to study the influence of precipitation hardening on the MFS behavior. For the 5 seconds interpass time, where solute drag is main mechanism responsible for preventing recrystallization, a new method was proposed to determine the temperature of no recrystallization (T_{nr}). The second type is based on an average schedule of 5 seconds interpass time but with incorporating time gaps of 10, 20 and 45 seconds at two different temperature ranges, i.e. above and below the temperature of no recrystallization (T_{nr}). Through the analysis of MFS vs. 1000/T diagrams, the results indicated phenomena such as static recrystallization and/or precipitation hardening take place during this time gap.

A mathematical model for MFS prediction was developed and validated with hot torsion data. The evolution of grain size, precipitate weight fraction and the effect of fractional softening on strain accumulation were also predicted by the model. The model is able to predict the critical strain per pass and therefore the fractional softening associated to dynamic recrystallization. Generally, there is a good agreement between the experimental and predicted mean flow stress over the whole deformation schedule. However, some discrepancy on the MFS values was observed for the first few passes of finishing stage especially when precipitation hardening is more likely to occur. Finally, several points are suggested to accommodate this discrepancy for future work.

RÉSUMÉ

A l'aide des résultats d'expériences qui utilisent la torsion à chaud, l'effet causé par «l'écart chronologique » est analysé (ex. le délai entre l'ébauchage et le finissage du schéma de laminage à chaud et le comportement de la contrainte d'écoulement moyenne des aciers à haute résistance mécanique). Deux types de déformation à chaud ont été étudiés : un schéma moyen au temps d'interpasse constante, dans lequel chaque passe est identique, dont la température diminue à un rythme régulier au cours du programme de laminage. Dans ce type de schéma, un intervalle de 5 et de 30 secondes sont utilisés afin d'étudier l'influence du durcissement structural sur le comportement de la contrainte d'écoulement moyenne. Aux 5 secondes d'interpasse, où le dragage est le mécanisme responsable qui empêche la recristallisation, une nouvelle méthode est proposée pour déterminer la température à laquelle la recristallisation n'est plus complète (Tnr). Pour ce qui est du 30 secondes d'interpasse, l'expérience s'inspire du schéma aux 5 secondes d'interpasse, en y ajoutant des intervalles de 10, 20 et 45 secondes à deux niveaux de température (ex. Au-dessus et en dessous de la température à laquelle la recristallisation n'est plus complète (Tnr). Selon les résultats d'analyse de la contrainte d'écoulement moyenne dans les diagrammes de 1000/T, des phénomènes tels que la recristallisation posttectonique et/ou le durcissement structural ont eu lieu durant ce temps d'attente.

Un modèle mathématique servant à prédire la contrainte d'écoulement moyenne est développé et validé avec les données des expériences qui utilisent la torsion à chaud. L'évolution de la taille de grain, la fraction massive de précipité et l'effet d'adoucissement sur la déformation accumulée peuvent tous être calculés par le modèle. Ce dernier est capable de mesurer la déformation critique au cours d'une passe et ainsi, déduire l'adoucissement associé à la recristallisation syntectonique. En général, au niveau de la contrainte d'écoulement moyenne, l'hypothèse et le résultat d'expérience du schéma de déformation se rejoignent en grande partie. Toutefois, quelques divergences sur celle-ci sont observées durant les premières passes du finissage surtout lorsqu'un durcissement structural est plus susceptible à se produire. Finalement, plusieurs points sont suggérés dans le but de combler ces lacunes dans les expériences à venir.

ACKNOWLEDGEMENTS

First and foremost, I would like to thank God. You have given me the power to believe in myself and pursue my dreams.

I would like to thank my wife Maram. Her support, encouragement, quiet patience and love were the backbone of this work. Also, I thank my parents for their supplications, support and faith in me.

I would like to convey my sincere gratitude to my supervisor Professor Stephen Yue for his support, encouragement and motivation since the first day until the end of my Master's Degree. It was a great honor for me being accepted as one of his graduate students.

I would like to convey my gratitude to my employer, Saudi Basic Industries Corporation (SABIC) for awarding me the scholarship to pursue my higher education.

I would like to extend my sincere thanks to McGill University and the Department of Mining and Materials Engineering for supporting this work.

I take this opportunity to thank my colleagues, Mr. Huseyin Aydin and Mr. Vladimir Basabe who supported me in accomplishing this experimental part of this work. A special thanks goes out to Mr. Jack Adel for translating the abstract to French. Also, sincere thanks to Mr. Ahmad Kaiser Hamid for his support, motivation and friendship throughout my entire time at McGill University.

NOMENCLATURE

σ	Stress (MPa)	Z	Zener-Hollomon Parameter
MFS	Mean Flow Stress (MPa)	$\mathrm{Q_d}$	Activation Energy for Deformation (J/mol)
σ_{SS}	Steady State Stress (MPa)	X	Fractional softening due to SRX/MDRX
ε	Strain	X_{DRX}	Fractional softening due to DRX
$\dot{\varepsilon}$	Strain rate (1/s)	X_p	Precipitated Fraction
ε_p	Peak Strain	K_s	Supersaturation Ratio
ε_c	Critical Strain	k_s	Solubility Product
$\varepsilon_{0.5}$	Strain for 50% Recrystallization	n	Avrami Exponent
t	Time (s)	d	Grain Size (μm)
t_{ip}	Interpass Time (s)	K_{acc}	Rate of Recovery
$t_{0.5\ Rex}$	Time Required for the Completion of 50% Recrystallization (s)	R	Gas Constant (8.314J J K^{-1} mol^{-1})
$\mathrm{t}_{0.05ps}$	Start Time for 5% Precipitation (s)	r	Gauge Radius (m)
T	Temperature (K)	θ	Twist Angle (Rad)
T_{nr}	Temperature of No Recrystallization	L	Gauge Length (m)

TABLE OF CONTENTS

LIST OF FIGURES

LIST OF TABLES

CHAPTER-1

INTRODUCTION

1.1 Introduction

Rolling process is one of the most important deformation processes in steel industry. Rolled products are used in buildings, pipelines, automobiles, home appliances, and in many other industries. With the severe specifications and growing demand for higher quality steels imposed by end users, continuous improvement and development of hot strip process is required.

Development of high quality steels is accomplished by the proper design of steel chemistry which includes studying the effects of alloy additions in steels. Furthermore, designing optimized rolling schedules contributes along with alloy additions in achieving the required steel microstructure and properties. Understanding how steel of a certain chemical composition behaves under hot deformation is important in designing rolling schedules. Therefore, mathematical modelling is used to explain the hot deformation behavior of steels including metallurgical events occurring during and after hot rolling such as strain accumulation, recovery and recrystallization. Mathematical modelling can be used in providing valuable information for process optimization and control.

1.2 Advantages of Mathematical Modeling

Various mathematical models have been developed by many researchers to clearly describe hot deformation behavior by linking the material flow stress with the operating variables, metallurgical events and steel chemistry. These models are results of experimental studies that might be limited to certain operating conditions and/or steel compositions. Additionally, models must be tested, validated and compared with the industrial data to be applicable. Mathematical modeling of hot rolling offers many advantages such as [1]:

- Minimizing the need for costly industrial trials.
- Improvement of rolling practices and developing new schedules.

- Saving hundreds of hours of lost time in designing, implementing, testing and analyzing plant trials.
- Understanding the individual and combined influence of using different rolling parameters such as strain or strain rate on the microstructures and mechanical properties of the final product.
- Predicting variables such as precipitation starting time, or grain size that cannot be measured during rolling.

1.3 Mathematical Models for Hot Rolling

Hodgson [1] listed some examples of established mathematical models with respect to model type as follows:

1. Empirical models:

   This type is used to describe the relations between process variables and parameters of interest using simple regression. Empirical models usually provide fast, simple and relatively accurate calculations depending on assumptions made. An example is introduced by Schey [2] in which the calculation of roll separating forces is simply achieved by manual calculations, spread sheets or simple computer programs.

2. One-dimensional models:

   They are more accurate than empirical models in predicting the roll separating forces and roll torques. The classical Orowan [3] approach is the base for this type of models, additional examples include:

   - Bland and Ford [4] technique for cold rolling.
   - Sims' model [5] for hot rolling, usually used as a first approximation.
   - Cook and McCrum [6] model in which roll flattening is taken into account, and hence accuracy is enhanced.
   - Sellars [7, 8] models to describe the microstructural evolution such as amount of static, dynamic and meta-dynamic recrystallization, grain size and strain.

3. Artificial neural networks (ANN).

4. Extremum theorems.

1.4 Thesis Objectives

The objective of this study is to develop a mathematical model for mean flow stress (**MFS**) during hot strip rolling for high-strength low-alloy (**HSLA**) steels. This requires an extensive review of the developed mathematical models proposed by other researchers including models for MFS prediction and for different metallurgical phenomena, such as recovery, recrystallization, precipitation and work hardening, during hot strip rolling. Special attention is given to the effect of using different time gaps, i.e. the time between roughing and finishing in a hot rolling schedule simulation, on the behaviour of mean flow stress.

According to published data [9], torsion tests indicate that there is ambiguity in the MFS behavior when time gap was used. Calvo et al. [9] reported a lower than expected MFS value in the first pass of finishing; the reasons for this were unclear although this may be correlated with grain coarsening according to author [9]. However, the investigated steels contained Ti, which should restrict grain coarsening. Furthermore, a sharp rise in the MFS value was observed for the second finishing pass which might be related to precipitation occurred during the time gap.

In this present investigation, hot torsion will be used to study the effect of time gap on the MFS behavior using different deformation schedules for two HSLA steels. Firstly, the MFS behaviour will be studied using an ‘average’ deformation schedule in which strain per pass, strain rate, interpass time and cooling rate are kept constant. Secondly, different time gaps, similar to the industrial schedules, will be incorporated into these average schedules to investigate the MFS behavior during finishing. Finally, a mathematical model will be developed, based on the obtained results, which takes into account different metallurgical phenomena.

CHAPTER-2

HOT ROLLING PROCESS

2.1 Objective of Rolling Process

The primary objective of Hot Strip Mill **(HSM)** is to reduce thickness of semi-finished steel slabs by rolling them through multiple rolling mill stands. Typical 4-high rolling mill consists of two work rolls, supported by two larger back-up rolls rotating in opposite directions. The strip is drawn by these rolls into the roll gap and forced through to the exit which causes reduction in thickness. The material's mechanical and metallurgical properties alter as these events progress. A schematic 4-high mill rolling stand is shown in Figure 2.1.

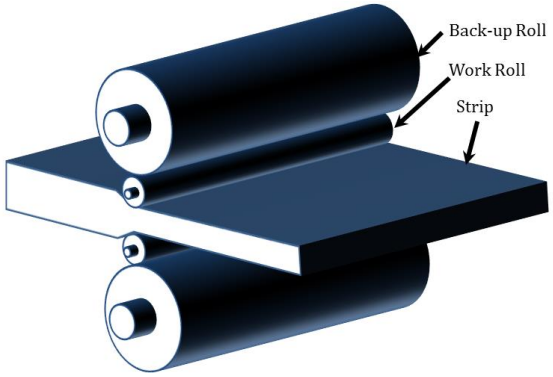

Figure 2.1: Schematic of four-high rolling mill stand.

2.2 Basic Components in Hot Strip Mill

2.2.1 Reheating furnace

The reheating stage comes after the casting process in the case of cold or warm charging. The slabs are dispatched to the reheating furnace and heated up to 1200 – 1250°C to dissolve the alloying elements and to remove the cast dendritic structures. The optimum selection of reheating temperature is essential to avoid extra operating cost associated with high temperature and to minimize formation of hard precipitates which affect the metallurgical developments caused by low reheating temperature [10, 11].

2.2.2 Roughing mill

Reheated slabs are descaled by highly pressurized water jets and transferred to the roughing mill. The slabs are reduced in several passes to around 75% of its primary thickness. In each pass, the reduction results in an increase in strip width which is controlled by vertical edge roller. The rolling speed of roughing mill is between 1 to 5 m/sec and roll diameters are around 1000 mm. The roll materials are generally cast steel or tool steel. There are different roughing mill configurations such as single stand reversing mill and multi-stand roughing train. Roughing stands are either two-high or four-high configuration. The roughing temperature is usually high allowing the slab to be fully recrystallized so there is almost no significance influence on the grain structure. The strip is then transferred to the coil box through the transfer bar table and usually the thickness at this stage is referred to as the transfer bar thickness [10, 11].

2.2.3 Coil box

As the transfer bars exits the roughing mill, it enters the coil box that is placed between roughing and finishing stages. The main objective of the coil box is to reduce the mill length. There are other several advantages such as breaking the scale, homogenizing the coil temperature providing uniform mechanical properties and increasing the productivity. The ends of transfer bars are cropped upon uncoiling and descaled before entering the finishing stands [10, 11].

2.2.4 Finish rolling

The finishing train typically consists of five to seven stands that are capable of reducing the thickness to 4-1 mm or even below. As in roughing mill, the roll configuration is usually four-high. When the coil reaches the appropriate temperature, it carefully enters first stand and continuously rolled through finishing stands. Frequently, higher reduction is employed at the last stand causing the strip speed to be as high as 10–20 m/s [10, 11].

2.2.5 Cooling

As the strip exits the finishing mill, it is cooled by water curtain on the run-out table under controlled conditions. The objective of cooling is to reduce the temperature from around 850°C to the coiling temperature which is about 580°C. Additionally, it is important for the precise control of microstructure. The length of the run-out table is between 150 to 200 m. The flow rates are 20,000-50,000 GPM, 5000-20,000 GPM for the top and bottom surface of the steel, respectively. At the end of cooling stage, the strip is coiled by a coiler and allowed to cool down to be ready for shipping [10, 11].

2.3 Theory of Strip Rolling

Figure 2.2 demonstrates the geometry of strip and work rolls including all forces acting during rolling that are needed for mathematical modeling of hot strip rolling.

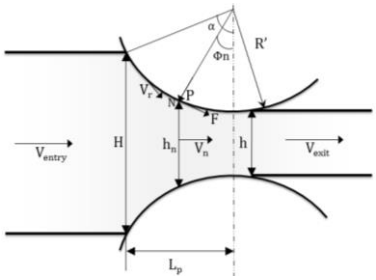

Figure 2.2: Work roll geometry and applied forces.

As the strip of thickness **H** enters the roll gap, it is reduced to **h** thickness by a pair of rotating work rolls with a specified speed $\mathbf{V_r}$ and therefore the rolled strip exits the roll gap with speed $\mathbf{V_{exit}}$. The metal is conserved as an elongation in the rolling direction by the law of conservation of mass, that is [10, 11]:

$$wHV_{entry} = whV_{exit} \qquad \text{(Eq. 2.1)}$$

Therefore, the strip exit speed must be higher than the entrance speed $\mathbf{V_{entry}}$ as the strip width **w** is assumed to be constant. At one point along the arc of contact, the strip speed is equal to work roll speed. This point is called the neutral or no slip point and its presence is due to the frictional forces **F** exerted on the strip along the arc of contact, discussed also in **section 2.3.3**. There is also the radial force known as rolling load **P**. The specific rolling load **p** is defined as the rolling load divided by the area of contact [10, 11].

$$p = P/wL_p \quad \text{(Eq. 2.2)}$$

The projected length of the arc of contact $\mathbf{L_p}$ is given by [10]:

$$L_p = \sqrt{R'(H-h)} \quad \text{(Eq. 2.3)}$$

The roll radius R is often corrected to R' to include the effect of roll flattening, see **section 2.3.1** for more details.

The bite angle or contact angle $\boldsymbol{\alpha}$ is based on the principle that states "for the work piece to enter the throat of the roll, the component of the friction force must be equal or greater than the horizontal component of the normal force" [10].

$$F\cos\alpha = P\sin\alpha \quad \text{(Eq. 2.4)}$$

$$\frac{F}{P} = \frac{\sin\alpha}{\cos\alpha} = \tan\alpha \quad \text{(Eq. 2.5)}$$

$$F = \mu P \quad \text{(Eq. 2.6)}$$

$$\mu \geq \tan\alpha \quad \text{(Eq. 2.7)}$$

From geometric point of view, the bite angle can be expressed by [12]:

$$\alpha = \cos^{-1}\left[1 - \frac{(H-h)}{2R'}\right] \quad \text{(Eq. 2.8)}$$

The effective strain in hot strip rolling is expressed by [12]:

$$\varepsilon_{eff} = 1.155\ln(H/h) \quad \text{(Eq. 2.9)}$$

The average strain rate can be determined as [12]:

$$\dot{\varepsilon} = \varepsilon_{eff}/t \quad \text{(Eq. 2.10)}$$

The time required for the application of strain is approximately equal to the time needed for the roll to move an angular distance $\boldsymbol{\alpha}$ and is given by [12]:

$$t = \frac{\alpha}{2\pi}\frac{60}{N} \quad \text{(Eq. 2.11)}$$

2.3.1 Hitchcock Equation for the Flattened Work Roll Radius

The work rolls undergo elastic deformation during rolling process and therefore the rolls are flattened by the rolling loads. As a result, the roll radius increases and pressure distribution is not elliptical in the contact zone due to the flattened rolls as shown in Figure 2.3.

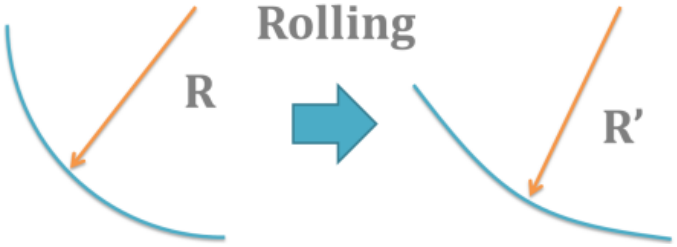

Figure 2.3: Effect of flattening on the work rolls.

Hitchcock [13] developed an equation to estimate the radius of curvature or the flattened roll, designated as R', where R' is given by:

$$R' = R\left[1 + \frac{CP}{w(H-h)}\right] \qquad \text{(Eq. 2.12)}$$

Where:

R: Roll radius [mm], **H**: Entry thickness [mm], **h**: Exit thickness [mm], **P**: Roll separating force [N], **w**: Strip width [mm] and **C**: a constant and is given by [13]:

$$C = \frac{16(1-v^2)}{\pi E} \qquad \text{(Eq. 2.13)}$$

Where:

E: Young's modulus [MPa] and **v**: Poisson's ratio for the work roll material.

From the above equations, the incremental change of roll radius due to flattening can be minimized by using rolls with higher Young's modulus E.

2.3.2 Redundant Strain Calculation in Strip Rolling

Redundant strain is present in all industrial deformation processes and it affects the deformation characteristics of metals. It is independent of the work material and is only a function of strip geometry of the contact zone. Siciliano et al. [14] derived an equation to calculate the redundant strain for the case of strip rolling based on an expression for strip drawing. According to Siciliano et al. [14], the redundant strain is about 10% of the homogeneous strain.

The redundant strain for strip rolling is expressed as:

$$\varepsilon_r = \frac{H - h}{4\sqrt{4R'^2 sin^2(\alpha/2) - [(H-h)^2/4]}} \quad \text{(Eq. 2.14)}$$

2.3.3 Forward Slip Ratio Calculation

The forward slip is a factor that describes the relative speed of the work rolls and the strip. It is also an indication of frictional conditions in the roll gap. The strip speed is slower than tangential speed of the work roll between the entrance and the neutral point; this is often referred as backward slip. Forward slip occurs between the neutral point and the exit when the strip speed is faster and the frictional forces on the strip hinder its motion. With reference to Figure 2.2, the neutral point, N is at an angle, $\emptyset_n$ where the strip and the tangential work roll speeds are equivalent and therefore no slip region is reached. In order to precisely estimate the strain rates and interpass times, the value of strip exit speed has to be corrected to include the effect of forward slip.

The forward slip factor is a function of the neutral angle, exit thickness of the strip and the work roll radius. It is given by [14]:

$$\gamma = \left(\frac{2R'}{h} cos\, \emptyset_n - 1\right)(1 - cos\, \emptyset_n) \quad \text{(Eq. 2.15)}$$

The neutral angle can be calculated using the following equation [14]:

$$\emptyset_n = \sqrt{\frac{h}{R'}} \quad tan\left[\frac{\pi}{8}\sqrt{\frac{h}{R'}}ln(1-r) + \frac{1}{2}tan^{-1}\left(\sqrt{\frac{r}{1-r}}\right)\right] \qquad \text{(Eq. 2.16)}$$

Where r is the reduction ratio of strip thickness, defined by [14]:

$$r = \frac{H-h}{H} \qquad \text{(Eq. 2.17)}$$

The strip thickness at the neutral point, h_n, is given by [14]

$$h_n = 2R'[1 - cos(\emptyset_n)] + h \qquad \text{(Eq. 2.18)}$$

The exit strip speed V_{exit} can therefore be expressed by [14]:

$$V_{exit} = (1+\gamma) \times V_r \qquad \text{(Eq. 2.19)}$$

$$V_r = 2\pi RN \qquad \text{(Eq. 2.20)}$$

Chapter-3

MODELING AND CALCULATION OF MEAN FLOW STRESS (MFS)

3.1 Definition of Mean Flow Stress (MFS)

The mean flow stress is a mathematical term used to describe the metal's resistance to deformation. Modeling of mean flow stress (MFS) during hot strip rolling can be helpful in understanding how the material responds or behaves to hot deformation. For example, phenomena such as static recrystallization (SRX), dynamic recrystallization (DRX), meta-dynamic recrystallization (MRX), strain accumulation, and phase transformation might be identified from the MFS behavior during rolling [15].

The MFS is the most significant factor for developing accurate models required for precise set-up and control of a hot strip mill (HSM). It is challenging to develop a common model for all steel grades because of its sensitivity to process parameters and composition [16].

The MFS for each rolling pass can be computed by integrating the area under the stress strain curve as shown in Figure 3.1 and then normalizing by the strain. The MFS for each pass is given by [12]:

$$MFS = \frac{1}{\varepsilon_f - \varepsilon_i} \int_{\varepsilon_i}^{\varepsilon_f} \sigma \, d\varepsilon \qquad \text{(Eq. 3.1)}$$

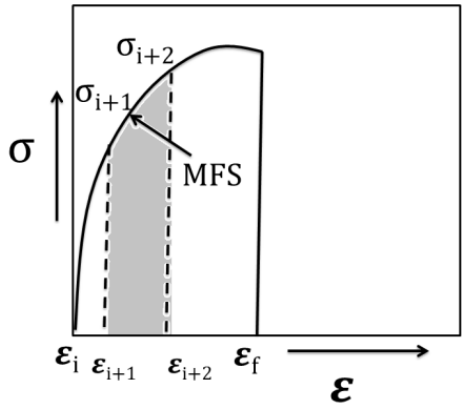

Figure 3.1: Graphical representation of MFS.

MFS can be approximated by summing the product of average stress and the strain change for each data reading of the entire pass, and then normalizing by the strain as follows [12]:

$$\boldsymbol{MFS} = \frac{1}{\varepsilon_f - \varepsilon_i}\sum_{\varepsilon_i}^{\varepsilon_f} \sigma_{\,avg}\Delta\varepsilon \qquad \text{(Eq. 3.2)}$$

$$\boldsymbol{MFS} = \frac{1}{\varepsilon_\mathrm{f} - \varepsilon_\mathrm{i}}\left[\frac{(\sigma_i + \sigma_{i+1})}{2}(\varepsilon_{i+1} - \varepsilon_i) + \frac{(\sigma_{i+1} + \sigma_{i+2})}{2}(\varepsilon_{i+2} - \varepsilon_{i+1}) + \cdots + \frac{(\sigma_f + \sigma_{f-1})}{2}(\varepsilon_f - \varepsilon_{f-1})\right] \qquad \text{(Eq. 3.3)}$$

Where ε_f and ε_i are the upper and lower strain limits, respectively.

3.2 MFS Calculations based on Rolling Load Data

3.2.1 Classical Orowan Model

Many numerical methods have been proposed to describe the mean flow stress using the finite element approach. However, these methods consume long time and therefore it is not efficient for the on-line prediction of MFS. Orowan [3] suggested a method to compute the roll pressure distribution using mechanical approach but it needs complicated numerical integration to describe the non-uniform deformation correlated with variable friction coefficients. As a result, many researchers have proposed theories that are based on approximations of Orowan method to compute the roll pressure distribution [5, 17].

3.2.2 Sims Method

Sims [5] proposed a model to simplify the calculation of rolling load under the following assumptions:

- Angles in the roll gap are so small which lead to the approximation of $sin\Phi \approx tan\Phi \approx \Phi$

- The product of the angular variable and the interfacial shear stress is relatively negligible compared to other terms
- Sticking friction occurs between the strip and the work roll.
- The Hitchcock radius can be used in Sims approach to include the effect of roll flattening.
- The rolled material is rigid-ideally plastic.

Sims method is commonly used in steel industry because of its simplicity. MFS can be computed by knowing the entry and exit thickness of the strip, its width, rolling force and work roll radius. MFS equation introduced by Sims is given by [5]:

$$MFS_{Sims} = \frac{P}{\frac{2}{\sqrt{3}} w L_p Q_p} \quad \text{(Eq. 3.4)}$$

Q_p is a geometrical factor defined by:

$$Q_p = \sqrt{\frac{r}{1-r}} \left[\frac{\pi}{2} tan^{-1}\left(\sqrt{\frac{r}{1-r}}\right) - \sqrt{\frac{R'}{h_1}} ln\left(\frac{h_n}{h_1}\sqrt{\frac{1}{1-r}}\right)\right] - \frac{\pi}{4} \quad \text{(Eq. 3.5)}$$

3.2.3 Ford and Alexander Method

Further simplification of Sims model was suggested by Ford & Alexander [17] based on the calculation of the mean shear yield strength and neglecting the effect of roll flattening. It is given by:

$$\bar{\tau}_{YS} = \frac{P/w}{\sqrt{R(h_0 - h_1)}\left[1.57 + \frac{\sqrt{R(h_0 - h_1)}}{(h_0 - h_1)}\right]} \quad \text{(Eq. 3.6)}$$

MFS_{Sims} and $\bar{\tau}_{YS}$ are correlated by the following relationship [14]:

$$MFS_{Sims} = \left(\sqrt{3} \times \bar{\tau}_{YS}\right) \quad \text{(Eq. 3.7)}$$

3.2.4 Friction-Hill Model

Friction hill model is based on the approximation of plane strain compression of a slab. The mean flow stress is given by [18]:

$$MFS_{Friction-Hill} = \frac{\sqrt{3}P}{2\left[\frac{1}{Q}(e^{Q}-1)wL_p\right]} \quad \text{(Eq. 3.8)}$$

Where

$$Q = \mu L_p/\bar{h} \quad \text{(Eq. 3.9)}$$

$$\bar{h} = (h_0 + h_1)/2 \quad \text{(Eq. 3.10)}$$

3.3 MFS Prediction Using Constitutive Relations

3.3.1 Analysis of MFS during Hot Rolling

Boratto et al. [19] were the first to analyze the MFS curves to determine the transformation temperatures of steel rolling (A_{r3}, A_{r1}, and T_{nr}). The analysis of mean flow stress (MFS) behavior as a function of the inverse of absolute temperature allows the identification of the microstructural changes which include SRX, DRX, MDRX, strain accumulation and phase transformation. Figure 3.2 demonstrates the microstructural changes in a hypothetical five-pass schedule. At the first pass, SRX occurs allowing full softening between passes in the low slope region. While strain is accumulated after the second pass as a result of low temperature rolling which leads to partial softening. Then, the accumulated strain reaches a critical value for DRX initiation providing no precipitation. This leads to MDRX between the third and fourth passes [20].

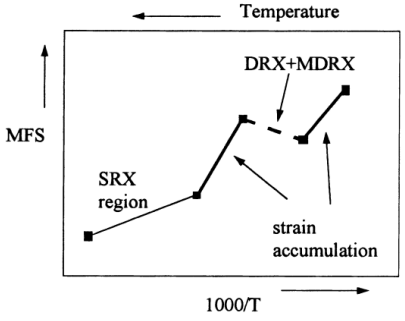

Figure 3.2: Microstructural changes in a hypothetical five passes. [20]

Based on the analysis of MFS behavior, controlled rolling schedule is designed according the microstructural requirements. Siciliano and Jonas [20] summarized the main types of controlled rolling which are:

1. Recrystallization Controlled Rolling (RCR): rolling is carried out above T_{nr} to achieve full softening between passes.
2. Conventional Controlled Rolling (CCR): rolling is carried out below T_{nr} with the presence of precipitations to produce "pancaked" austenite grains; this is followed by SRX or DRX.
3. Dynamic Recrystallization Controlled Rolling (DRCR): rolling is carried out below T_{nr} with induced DRX in one or more passes by applying large strain at high strain rate or by strain accumulation. This type is used for intense grain refinement caused by DRX and with the absence of SRX.

Figure 3.3 show the three different types with a hypothetical five-pass schedule. These types are used in accordance with process limitations to design a proper rolling schedule.

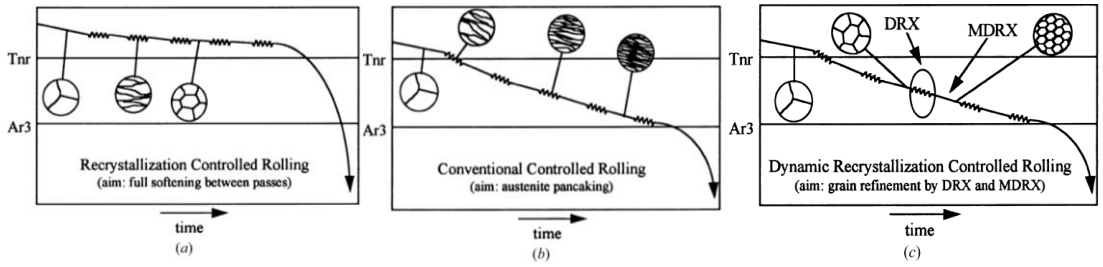

Figure 3.3: The main types of controlled rolling. a) recrystallization controlled rolling, (b) conventional controlled rolling, and (c) dynamic recrystallization controlled rolling [20].

3.3.2 MFS Equations Based only on Static Recrystallization (SRX)

Misaka and Yoshimoto [21] developed a constitutive equation that determines the MFS as a function of carbon level, strain and strain rate assuming complete static recrystallization between passes. The MFS in the following equation is expressed in von Mises form and in units of kgf/mm^2.

$$MFS_{Misaka} = exp\left(A + \frac{B}{T+273}\right)\varepsilon^{0.21}\dot{\varepsilon}^{0.13} \quad \text{(Eq. 3.11)}$$

$$A = 0.126 - 1.75\,[C] + 0.594\,[C]^2$$

$$B = 2851 + 2968\,[C] - 1120\,[C]^2$$

[C]: carbon concentration in wt%, T: temperature in °C, ε: strain, and ε̇: strain rate in sec^{-1}. The equation is applicable for a carbon level of 1.2%, temperature range 750–1200 °C, reduction ~50% and strain rate of 30–200 s^{-1}.

Devadas et al. [22] observed that Misaka's model over predicts the flow stress as compared to measured data from a cam-plastometer for a low alloy steel.

Siciliano et al. [14] updated Misaka's model by adding a multiplying factor to take the Mn content into account. This factor, f, was determined using the MFS values calculated from the industrial data for two Mn levels over the temperature range where only SRX occurs and was fitted to the equation. The new updated Misaka equation is expressed by:

$$MFS^{*}_{Misaka} = f.MFS_{Misaka} \quad \text{(Eq. 3.12)}$$

The factor, f, is expressed by:

$$f = 0.780 + 0.137[Mn] \quad \text{(Eq. 3.13)}$$

The validity of the previous equation was tested for Mn concentrations ranging from 0.27 to 1.08.

Minami et al. [15] added other terms to include the solution strengthening effects of Nb, and Ti:

$$f = 0.768 + 0.51[Nb] + 0.137[Mn] + 4.217[Ti] \quad \text{(Eq. 3.14)}$$

Equation 3.14 is valid over the following concentration ranges: [Nb]:0.020-0.080%, [Mn]:0.35-1.33%, and [Ti]:0-0.024%

Kirihata et al. [23] developed the previous equation to take alloy addition into account.

$$f = 0.835 + 0.51[Nb] + 0.098[Mn] + 0.128[Cr]^{0.8} + 0.144[Mo]^{0.3} + 0.175[V] + 0.01[Ni] \quad \text{(Eq. 3.15)}$$

The relevant compositional range is: [C]:0.20-0.47%, [Mn]:0.52-0.76%, [Nb]:0.0-0.016%, [Cr]:0.0-1.38%, [Mo]:0.0-0.97%, [V]:0.0-0.12%, and [Ni]:0.0-0.46%.

Shida [24] modeled the flow stress behavior of the steels in austenite, ferritic and in the two-phase regions of 8 grades of C-Mn steel.

$$\sigma = \sigma_d f_\varepsilon f_{\dot{\varepsilon}} \quad \text{(Eq. 3.16)}$$

Where, σ_d is a function of carbon content and deformation temperature while f_ε and $f_{\dot{\varepsilon}}$ are functions of strain and strain rate, respectively.

$$\sigma_d = 0.28\, exp\left(\frac{5.0}{T} - \frac{0.01}{C + 0.05}\right) \quad \text{(Eq. 3.17)}$$

$$T = (T[°C] + 273)/1000 \quad \text{(Eq. 3.18)}$$

$$f_\varepsilon = 1.3\left(\frac{\varepsilon}{0.2}\right)^n - 0.3\left(\frac{\varepsilon}{0.2}\right) \quad \text{(Eq. 3.19)}$$

$$f_{\dot{\varepsilon}} = \left(\frac{\dot{\varepsilon}}{10}\right)^m \quad \text{(Eq. 3.20)}$$

$$n = 0.41 - 0.07C \quad \text{(Eq. 3.21)}$$

$$m = (-0.019C + 0.126)T + (0.076C - 0.05) \quad \text{(Eq. 3.22)}$$

The equation was tested for the following experimental range: [C]: 0.01-0.8%, strain rate: 0.2-30 s^{-1}, temperature: 650-1200°C, and true strain up to 0.60.

Biglou et al. [25] used torsion tests to develop an MFS equation for a steel containing [C]:0.07%, [Mn]:l.30%, [Nb]:0.076%, and [Ti]:0.24%. The MFS is expressed in MPa, and is a function of the temperature, T in Kelvin:

$$MFS = 166.66 + 391.2\left(\frac{1000}{T}\right) \quad \text{(Eq. 3.23)}$$

Karjalainen et al. [26] also used torsion tests and derived another MFS equation for steels containing [C]: 0.05-0.90%, [Mn]: 1.20-1.57%, [Nb]: 0.011-0.046%, [Ti]: 0.001-0.142%, [V]: 0-0.082%, [Ni]: 0.03-0.7%:

$$MFS = -255 + \frac{380000}{T} \quad \text{(Eq. 3.24)}$$

Johnson and Cook [27] developed a constitutive equation for the flow stress as function of the strain, strain rate and temperature. The equation consists of three distinct functions which include five material constants determined by experimental data. The equation is expressed as:

$$\sigma = [A + B\varepsilon^n][1 + Cln\dot{\varepsilon}^*][1 - T^{*m}] \quad \text{(Eq. 3.25)}$$

Lee and Yeh [28] suggested the constitutive relation of the alloy steel using Johnson–Cook equation [27]

$$\sigma = [A + B\varepsilon^n][1 + Cln(\dot{\varepsilon}/\dot{\varepsilon}_0)]\{1 - [(T - T_0)/(T_m - T_0)]^m\} \quad \text{(Eq. 3.26)}$$

3.3.3 MFS Equations Based on Dynamic Recrystallization (DRX)

Kim et al [29] developed a constitutive equation by modifying the Voce's equation [30] to estimate the flow stress curve using hot torsion and compression tests for medium carbon and low alloy steel. The dynamic recrystallization as well as the dynamic softening were taken into account as the total flow stress is given by [29]:

$$\sigma_{\text{total}} = \sigma_{(\text{WH+DRV})} - \sigma_{\text{DRX}} \quad \text{(Eq. 3.27)}$$

The first term in Equation 3.27 accounts for two important metallurgical phenomena namely work hardening (WH), and dynamic recovery (DRV). Within the region of WH+DRV, the flow stress curve can be expressed by the following equation [29, 31, 32]

$$\sigma_{(WH+DRV)} = \sigma_p m[1 - exp(-C\varepsilon)] \quad \text{(Eq. 3.28)}$$

The second term accounts for the drop in flow stress as a result of DRX and it is given by [31-33]:

$$\varepsilon > \varepsilon_c \qquad \sigma_{DRX} = (\sigma_P - \sigma_{SS})\left[\frac{X_{DRX} - X_{\varepsilon_p}}{1 - X_{\varepsilon_p}}\right] \quad \text{(Eq. 3.29)}$$

$$\varepsilon < \varepsilon_c \qquad \sigma_{DRX} = 0 \quad \text{(Eq. 3.30)}$$

Where X_{DRX} is the volume fraction of DRX at a certain strain and it given as follows:

$$X_{DRX} = 1 - exp\left[-\left(\frac{\varepsilon - \varepsilon_c}{\varepsilon^*}\right)^{m'}\right] \quad \text{(Eq. 3.31)}$$

Where:

C	Coefficient	X_{ε_p}	Volume fraction of DRX at peak strain.
m	work hardening exponent	m'	Avrami's constant [34].
σ_p	Peak stress	ε_c	Critical strain for initiating of DRX.
σ_{SS}	Steady state stress	ε^*	Strain for maximum softening rate [32, 33]

The previous parameters such as $C, m, \varepsilon_c,$ and σ_p were evaluated in Kim's work and expressed as functions of *Z*/*A* [29]. These equations were tested and verified for the temperature range of 900–1100 °C , strain rate range of 0.05–5 s^{-1} and for a steel that contains [C]=0.04, [Mn]=0.67, [Si]=0.21, [Cr]=0.97, [Mo]=0.15, [P]=0.045, and [S]=0.030wt%

Laasraoui and Jonas [35] derived a formula based on the dislocation theory to describe the strain hardening behavior. The flow behavior was described by a hyperbolic sine equation that correlates strain rate, temperature, and steady state stress. The flow stress was given in the following expressions

$$\dot{\varepsilon} = A[sinh(\alpha\sigma_{SS}^*)]^{n'} \, exp(-Q/RT) \quad \text{(Eq. 3.32)}$$

$$\sigma = \left[{\sigma_{SS}^*}^2 + \left(\sigma_0^2 - {\sigma_{SS}^*}^2\right) e^{-\Omega e}\right]^{0.5} \quad \text{(Eq. 3.33)}$$

$$\sigma_0 = \alpha\mu b\sqrt{\rho_0} \quad \text{(Eq. 3.34)}$$

$$\sigma_{SS} = \alpha\mu b\sqrt{U/\Omega} \quad \text{(Eq. 3.35)}$$

Further details and clarification of these equations are given in a paper published by Laasraoui and Jonas [35].

As Misaka equation over predicts the flow stress at high strain levels, Siciliano et al. [14] added a second term into the modified Misaka equation to take the dynamic softening due to recrystallization into account and it is expressed by:

$$\mathrm{MFS_{Siciliano}} = \mathrm{MFS^*_{Misaka}} \times 9.8 \times \left(1 - \mathrm{X_{dyn}}\right) + \mathrm{K}\sigma_{\mathrm{ss}}\mathrm{X_{dyn}} \quad \text{(Eq. 3.36)}$$

K is a fitting parameter to convert from stress to MFS, K is reported as 1.14 for Nb steel and the factor of 9.8 to convert from kgf/mm^2 to MPa [14].

Chapter-4

METALLURGICAL EVENTS IN HOT ROLLING

4.1 Recovery

Recovery is a softening mechanism that involves rearrangement of dislocations and other defects to be strain free and thus stable thermodynamically. There is no microstructure change involved since grain boundary motion is not present in recovery. The drop in internal stress is associated with the reduction and rearrangement of dislocations which can reduce the yield stress by up to 40% [36]. At high temperature range, the rate of recovery is higher compared to lower temperature range because of greater thermal activation. Additionally, the rate of recovery increases as the dislocation density increases by increasing the strain or strain rate.

In hot deformation, metals experience dynamic and static restoration processes in the form of recovery and recrystallization as demonstrated in Figure 4.1 [37]. The dynamic restoration is driven by thermal activation during hot deformation. It impacts generally the shape and magnitude of stress-strain curve. While the static restoration is driven by stored energy after hot deformation and it determines the microstructure submitted to the following process.

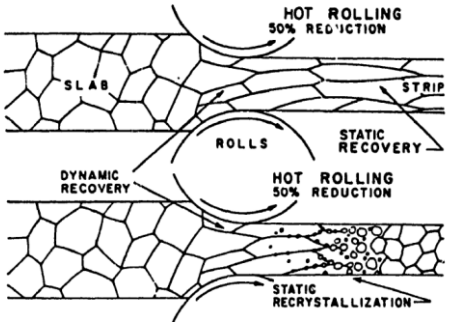

Figure 4.1: Recovery and recrystallization in hot rolling. [37]

Metals of high stacking fault energy such as ferrite experience high dynamic recovery even at large strains leading to a decrease of the driving force in the unrecrystallized regions and hence poor recrystallization. While low stacking fault energy metals such as austenite, have poor recovery and therefore a critical strain is attainable at which nucleation of recrystallization takes place. Therefore, both static and dynamic recovery are commonly neglected in austenite regions.

4.2 Recrystallization

Recrystallization is the nucleation and growth of new strain-free grains replacing the deformed grains. It also involves migration of high angle boundaries that annihilates dislocations [38]. High angle boundaries have misorientations of more than 10-15° [39]. Cahn [40] summarized the laws of recrystallization as follows:

i. Recrystallization starts when the applied or accumulated strain reaches a critical value.
ii. An increase in the amount of deformation and/or interpass time decreases the temperature needed for recrystallization.
iii. The recrystallized grain size is a function of the amount of deformation and holding temperature. Smaller recrystallized grain sizes can be produced by increasing the strain and lowering the holding temperature.
iv. Grain growth occurs when recrystallization is completed at high holding temperature.

The rate of recrystallization is a function of stored energy, density of nucleation sites and temperature [41]. The stored energy can be increased with increasing strain and strain rate and with decreasing deformation temperature. The amount of strain plays a major role in estimating the time for 50% recrystallization [42-44]. Additionally, strain rate influences rate of recrystallization as it affects the flow stress and the stored energy. The density of nucleation sites is influenced by the grain size; smaller grain size leads to higher density and thus faster recrystallization rate. Lastly, the effect of temperature is high on the recrystallization rate and follows Arrhenius law as suggested by Djaic and

Jonas [45]. McQueen and Jonas [38] suggested that recrystallization rate would increase by about one order of magnitude if the holding temperature is raised by 50°C.

4.2.1 Dynamic Recrystallization

The occurrence of DRX has been studied and understood by many researchers, their findings as follows:

- DRX is initiated when the applied strain exceeds a critical value causing rapid softening [46].
- Some researchers suggested the DRX can also take place in short interstand distances due to strain accumulation in HSM [47, 48].
- Others have reported that Z must be smaller than a limiting value Z_{lim} and $\boldsymbol{\varepsilon} > \boldsymbol{\varepsilon}_c$ to allow the occurrence of DRX [49, 50].
- At low strain rate, multiple peak behavior appears in the stress-strain curve as a result of grain coarsening while single peak behavior is associated with grain refinements [51]. These two behavior s were modeled by Luton and Sellars [52]. Additionally, the multiple peak behavior was explained by McQueen and Jonas [38] and Sellars and Tegart [53].
- The resultant rapid softening and intense grain refinement by DRX considerably influence the flow behavior and rolling loads in the following passes [46].
- DRX kinetics are greatly faster than SRX [1].

4.2.2 Dynamic Recrstallization Kinetics

The drop in the MFS due to DRX at high strains by the volume fraction of the dynamically recrystallized grains can be described by Avrami equation as follows:

$$X_{dyn} = 1 - exp\left[-0.693\left(\frac{\varepsilon - \varepsilon_c}{\varepsilon_m - \varepsilon_c}\right)^2\right] \qquad \text{(Eq. 4.1)}$$

Where, X_{DRX} is dynamic recrystallization fraction, ε the true strain, ε_c the critical strain for the onset of DRX, and ε_m the strain for the maximum softening rate during dynamic recrystallization.

According to Senuma et al. [54], the fractional softening due to dynamic recrystallization is as follows:

$$X_{dyn} = 1 - exp\left[-0.693\left(\frac{\varepsilon - \varepsilon_c}{\varepsilon_{0.5}}\right)^2\right] \quad \text{(Eq. 4.2)}$$

Where, $\varepsilon_{0.5}$ is the strain for 50% completion of recrystallization

The volume fraction of dynamic recrystallization with constant strain rate is generally a function of strain at different temperatures. Table 4.1 lists some equations to calculate the fractional softening due to DRX.

Table 4.1: Equations to describe DRX Kinetics for different steels.

Steel Type	Equation	Reference
C-Mn	$X_{dyn} = 1 - exp\{-0.693[(\varepsilon - \varepsilon_c)/\varepsilon_{0.5}]^2\}$ $\varepsilon_{0.5} = 1.144 \times 10^{-3} d_0^{0.25} \dot{\varepsilon}^{0.05} exp(6420/T)$	**[54, 55]** (Eq. 4.3)
CMVN Steel	$X_{dyn} = 1 - exp\{-0.693[(\varepsilon - \varepsilon_c)/\varepsilon_{0.5}]^2\}$ $\varepsilon_{0.5} = 3.5 \times 10^{-6} d_0^{0.25} \dot{\varepsilon}^{0.32} exp(141000/RT)$	**[23]** (Eq. 4.4)
Nb, Nb-Mo, Nb-Ti	$X_{dyn} = 1 - exp(-2.50(\varepsilon - \varepsilon_c)^{1.5})$ $\varepsilon_{ss} - \varepsilon_c = 1.16 \times 10^{-3} \frac{\{1 + 20([Nb] + 0.02[Ti] + \Delta \times 0.035)\}}{1.78}$ $\times d_0^{0.26} \left[\dot{\varepsilon}. exp\left(\frac{325000}{RT}\right)\right]^{0.197}$ For Steels containing Mo: $\Delta = 1$ otherwise : $\Delta = 0$	**[56]** (Eq. 4.5)
C-Mn-Cr	$X_{dyn} = 1 - exp\{-18.2 \times 10^4 d_0^{-0.5} Z^{-0.2} (\varepsilon - \varepsilon_c)^{1.5}\}$	**[57]** (Eq. 4.6)

A Critical and Peak Strains

During hot strip rolling, DRX is initiated at a critical strain at sufficiently high temperature causing rapid softening and intense grain refinement. This softening phenomenon is accompanied with a drop in flow stress with increasing strain affecting the rolling loads at the subsequent deformation passes. However, this drop in flow stress

does not occur immediately after reaching the critical strain making the determination of the onset of DRX quite difficult as shown in Figure 4.2. Rather, stress continues to increase because the hardening rate of unrecrystallized parts is higher than softening rate associated with DRX progress. After reaching a defined peak stress and strain, flow stress drops until steady stress is attained indicating a balance in the rates of hardening and softening. Some materials with dynamic recovery (DRV) as the only softening mechanism, peak stresses are not detectable [14, 58].

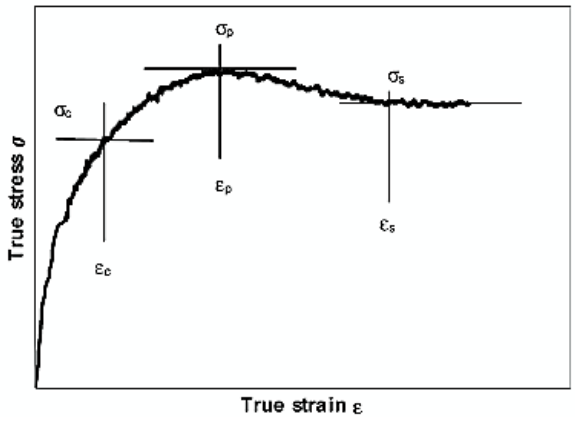

Figure 4.2: Stress-strain curve at constant strain rate. [58]

As listed in Table 4.2, various equations are available to estimate the peak strain ($\boldsymbol{\varepsilon}_p$), which is commonly used to calculate the critical strain ($\boldsymbol{\varepsilon}_c$). The peak strain ($\boldsymbol{\varepsilon}_p$) is a function of the initial grain size, temperature and strain rate as follows [59]:

$$\varepsilon_c(Z) = a\, d_0^b Z^c \qquad \text{(Eq. 4.7)}$$

Pereda et al. [56] proposed a generalized model for the calculation of the peak strain in Nb, Nb-Ti and Nb-Mo steels:

$$\varepsilon_p = 3.7 \times 10^{-3} \frac{\{1 + 20([Nb] + 0.02[Ti] + \Delta \times 0.035)\}}{1.78} \times d_0^{0.147} Z^{0.155} \qquad \text{(Eq. 4.8)}$$

Where $\Delta = 0$ for Nb and Nb-Ti steels and $\Delta = 1$ for Nb-Mo steels. The equation was tested for the following range: [C]: 0.05-0.1, [Mn]:1.42-1.57, [Si]:0.04-0.31, [Nb]:0.028-0.035, [Mo]:0.15-0.31, [Al]:0.023-0.039, and [Ti]:0.005-0.007.

Table 4.2 : Equations to predict the peak strain for different steels.

Steel Type	Equation	References
Nb	$\varepsilon_p = \frac{(1+20[Nb])}{1.78} \times 2.8 \times 10^{-4} d_0^{0.5} \left[\dot{\varepsilon}.exp\left(\frac{375000}{RT}\right)\right]^{0.17}$	**[60, 61]** (Eq. 4.9)
0.056Nb-0.158Mo	$\varepsilon_p = 6.9 \times 10^{-4} d_0^{0.5} Z^{0.25}$	**[62]** (Eq. 4.10)
0.058Nb-0.283Mo	$\varepsilon_p = 1.8 \times 10^{-3} d_0^{0.5} Z^{0.11}$	**[62]** (Eq. 4.11)
0.059Nb-0.161Mo 0.21Ni	$\varepsilon_p = 1.3 \times 10^{-3} d_0^{0.5} Z^{0.13}$	**[62]** (Eq. 4.12)
0.059Nb-0.156Mo 0.5Ni	$\varepsilon_p = 1.2 \times 10^{-3} d_0^{0.5} Z^{0.10}$	**[62]** (Eq. 4.13)
0.061Nb-0.157Mo 0.3Cr	$\varepsilon_p = 1.1 \times 10^{-3} d_0^{0.5} Z^{0.13}$	**[62]** (Eq. 4.14)
0.062Nb-0.155Mo 0.61Cr	$\varepsilon_p = 8.3 \times 10^{-4} d_0^{0.5} Z^{0.17}$	**[62]** (Eq. 4.15)
0.03Nb-0.151Mo	$\varepsilon_p = 5.8 \times 10^{-4} d_0^{0.5} Z^{0.16}$	**[62]** (Eq. 4.16)
Nb	$\varepsilon_p = 0.0016\, d_0^{0.5} \left[\dot{\varepsilon}.exp\left(\frac{241000}{RT}\right)\right]^{0.17}$	**[23]** (Eq. 4.17)
Nb, Nb-Ti, Nb-Mo	$\varepsilon_p = 3.7 \times 10^{-3} \frac{\{1+20([Nb]+0.02[Ti]+\Delta \times 0.035)\}}{1.78} \times d_0^{0.147} \left[\dot{\varepsilon}.exp\left(\frac{325000}{RT}\right)\right]^{0.155}$ For Steels containing Mo: $\Delta = 1$ otherwise : $\Delta = 0$	**[56]** (Eq. 4.18)
C-Mn	$\varepsilon_p = 5.5 \times 10^{-4} d_0^{0.5} Z^{0.1}$	**[57]** (Eq. 4.19)
Nb	$\varepsilon_p = 7.51 \times 10^{-4} Z^{0.23}$	**[63]** (Eq. 4.20)

The $\boldsymbol{\varepsilon}_c/\boldsymbol{\varepsilon}_p$ ratio often ranges between 0.65-0.86 [64] and is commonly taken as 0.8 for plain C-Mn steels, and 0.65 for Nb steels [65]. Hodgson and Collinson [66] observed that the carbon addition decreases the $\boldsymbol{\varepsilon}_c/\boldsymbol{\varepsilon}_p$ ratio. According to Sakui et al. [67], the critical strain is around $0.7\boldsymbol{\varepsilon}_p$ while Rossard [68] suggested that $\boldsymbol{\varepsilon}_c$ is approximately $0.833\boldsymbol{\varepsilon}_p$. Generally, the equation used to describe the critical strain is as follows:

$$\varepsilon_c = C\varepsilon_p \qquad \text{(Eq. 4.21)}$$

Sellars and Davies [64] reported that the peak strain increases with Zener-Hollomon parameter. The $\boldsymbol{\varepsilon}_c/\boldsymbol{\varepsilon}_p$ ratio approaches unity at high Z value resulting in the absence of DRX.

Ryan and McQueen [69] observed the presence of inflections associated with peak stresses in constant rate flow curve as expressed by strain hardening rate:

$$\theta = (\partial\sigma/\partial\varepsilon)_{\dot{\varepsilon}} \qquad \text{(Eq. 4.22)}$$

Poliak and Jonas [58] concluded that the absence of peak stress does not indicate the absence of DRX. The DRX initiation can be detected from the plot of strain hardening rate again stress. Inflections are stronger indication of the presence of DRX compared to peak stress. On the basis of Ryan and McQueen [69], the point at which the work hardening rate equals zero ($\theta = 0$) represents the peak stress θ-σ curve [70]. The critical stress is the highest point in the plot of the derivative of the strain hardening rate (dθ/dσ) against stress. The critical strain, therefore, can be determined using the value of critical stress in the stress-strain curve [71].

Siciliano et al. [20] developed an equation to estimate $\varepsilon_c/\varepsilon_p$ ratio for Nb steel as follows:

$$\varepsilon_c/\varepsilon_p = 0.8 - 13Nb_{eff} + 112Nb_{eff}^2 \qquad \text{(Eq. 4.23)}$$

$$Nb_{eff} = Nb - \frac{Mn}{120} + \frac{Si}{94} \qquad \text{(Eq. 4.24)}$$

B Steady State Stress

The steady state stress is a strain independent value and is defined according to Roucoules et al. [72] by the following expression:

$$\sigma_{ss} = A_{ss} Z^{q_{ss}} = A_{ss}[\dot{\varepsilon} \exp(Q_d/RT)]^{q_{ss}} \quad \text{(Eq. 4.25)}$$

This equation is also used for the characterization of hot deformation behavior at different temperatures and strain rates and activation energy of austenite, Q_d, of steels [53, 59, 70]. The factor, A, is dependent on the chemical composition and initial grain size and q is the power law exponent.

Kirihata et al. [23] proposed a model to estimate the steady state stress for CMVN steel as follows:

$$\sigma_{ss} = 1.18 \left[\dot{\varepsilon} \exp\left(\frac{330000}{RT}\right)\right]^{0.15} \quad \text{(Eq. 4.26)}$$

Both constants, A_{ss} and q_{ss}, can be determined using experimental tests and by utilizing the natural logarithm correlations that exist between, σ_{ss}, $\dot{\varepsilon}$, and $\frac{1}{T}$ as follows [53, 59, 70]:

$$ln(\sigma_{ss}) = ln(A) + q ln(\dot{\varepsilon}) + q(Q_d/RT) \quad \text{(Eq. 4.27)}$$

Then, by taking partial derivatives of both sides with respect to:

- Strain rate at constant deformation temperature gives the value of q:

$$\left[\frac{\partial\, ln(\sigma_{ss})}{-ln(\dot{\varepsilon})}\right]_T = -q \quad \text{(Eq. 4.28)}$$

- Reciprocal of T at constant $\dot{\varepsilon}$, gives the value of Q_d:

$$\left[\frac{\partial\, ln(\sigma_{ss})}{\partial\left(\frac{1}{T}\right)}\right]_{\dot{\varepsilon}} = q\frac{Q_d}{R} \quad \text{(Eq. 4.29)}$$

C Strain for Maximum Dynamic Softening

The strain, (ε_m), at which the rate of dynamic softening is maximized, can be determined experimentally by plotting work hardening rate against the true strain. The strains, (ε_m), are the minimum points in work hardening rate against the true strain curve.

Shaban and Eghbali [70] observed that decreasing deformation temperature and/or increasing strain rate, increases the value of ε_m. Additionally, work hardening rate increases after ε_m and reaches zero in case of full DRX [71]. Many researchers use the term, $\varepsilon_{0.5}$, strain for 50% completion of DRX instead of ε_m in modeling the recrystallization kinetics [14, 15, 59, 61, 71, 73, 74]. According to Yada [55], $\varepsilon_{0.5}$ is a function of the initial grain size, d_0, strain rate, $\dot{\varepsilon}$, and temperature,T. Stewart et al. [71] reported that the strain for maximum dynamic softening can be expressed as function of Zener-Hollomon parameter as follows:

$$\varepsilon_m \propto Z^{q_m} \quad \text{or} \quad \varepsilon_m = a\, Z^b \qquad \text{(Eq. 4.30)}$$

Where A_m and q_m are material constants and Zener-Hollomon exponent.

Kim et al. [29] used the equation associated with the Arrhenius-type temperature sensitivity term proposed by Sellars and Tegart [53] to describe, ε_m , to be a function of dimensionless parameter for AISI 4140 steel, Z/A as follows:

$$\varepsilon_m = 0.528\ (Z/A)^{0.1675} \qquad \text{(Eq. 4.31)}$$

4.2.3 Static and Meta-dynamic Recrystallization

Static (SRX) and meta-dynamic (MDRX) recrystallization are softening mechanisms which commonly take place after deforming the steels at high temperatures. They both occur between passes during interpass time in hot strip rolling. Static recrystallization only occurs when prestrain exceeds a critical value and after incubation time the SRX nuclei formed.

Djaic and Jonas [42], first detected the kinetics of MDRX and found that it depends only on strain rate. These findings were verified later by other researchers [42, 75-77]. In MDRX, the dynamically formed nuclei resulted from exceeding the critical strain continue to grow statically during the interpass time. There is no nucleation interval since the nuclei already formed by DRX. Nucleation for static recrystallization can occur in the regions that do have dynamic nuclei.

4.2.4 Kinetics of SRX and MDRX

The kinetics of SRX and MDRX can be generally described by Avrami equation [34] as given below:

$$X_{SRX/MDRX} = 1 - exp\left[-0.693 \times \left(t/t_{0.5\,SRX/MDRX}\right)^{n}\right] \qquad \text{(Eq. 4.32)}$$

Where $t_{0.5}$ is the time to reach 50% recrystallization by SRX or MDRX. Extensive research has been done to model the time for the completion of 50% recrystallization for SRX as well as MDRX which are generally expressed by:

$$t_{0.5,MRX} = a\,\varepsilon^{b}\dot{\varepsilon}^{c}\,d_0^{d}exp\left(\frac{q}{T}\right) \qquad \text{(Eq. 4.33)}$$

$$t_{0.5,MDRX} = A_{MDRX}\dot{\varepsilon}^{p}exp\left(\frac{Q_{MDRX}}{RT}\right) \qquad \text{(Eq. 4.34)}$$

<u>Observations on the occurrence of SRX:</u>

- Finer grain size means higher density of nucleation sites and that leads to shorter $t_{0.5,SRX}$.
- Higher strain rate results in finer grain size; however, the exponent s is not greatly affected and it lies between 0 to -0.2
- The grain size exponent s is usually taken as 2; however it has been reported as 1.7 for Nb steel [78].
- Activation energy for SRX is independent of strain [64].
- SRX is not present for strain higher than the transitional strain $\boldsymbol{\varepsilon}_T$ which is found to be equal to 1.7 $\boldsymbol{\varepsilon}_p$ for Nb steel [79].
- The presence of Nb significantly retards the static recrystallization [78].
- It has been observed that the strain exponent q depends on the initial grain size and can be expressed as $q = 5.6d_0^{-0.15}$ for Nb, Ti, and Nb-Ti steels [80].

<u>Observations on the occurrence of MDRX:</u>

- Slight dependence on the chemical composition and temperature [81].

- Density of nucleation sites remains almost constant once the applied strain exceeds a peak value [72].
- At the steady-state region, MDRX entirely replaces SRX. The stored energy becomes independent of strain and the initial grain size. It is only influenced by the strain rate and temperature of deformation and holding [43, 45].
- MDRX is faster than SRX by about an order of magnitude since it does not require an incubation period [38].

According to Luton et al. [82], Bai et al. [83] and Uranga et al. [79], there are three different recrystallization regions that depend on the amount of the applied strain as shown in Figure 4.3 [74].

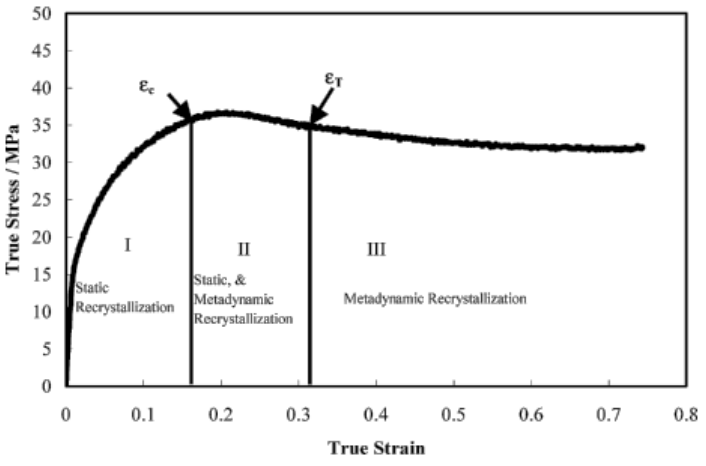

Figure 4.3: Recrystallization regions with regard to the applied strain. [74]

1. Region I ($\boldsymbol{\varepsilon}<\boldsymbol{\varepsilon}_c$): Only pure static recrystallization can occur and the fractional softening can be calculated using the listed equation in Table 4.3.
2. Region II ($\boldsymbol{\varepsilon}_c <\boldsymbol{\varepsilon}<\boldsymbol{\varepsilon}_T$): Static as well as metadynamic recrystallization can occur. The total fractional softening can computed using Table 4.3 ,4.4 and the following expressions [74]:

$$X_F^{SRX} = X_{SRX}/(X_{SRX} + X_{MDRX}) \quad \text{(Eq. 4.35)}$$

$$X_F^{MDRX} = X_{MDRX}/(X_{SRX} + X_{MDRX}) \quad \text{(Eq. 4.36)}$$

3. Region III ($\boldsymbol{\varepsilon}>\boldsymbol{\varepsilon}_T$): Only pure metadynamic recrystallization can occur and the fractional softening can be calculated using the listed equation in Table 4.4.

Table 4.3: Equations to describe SRX Kinetics for different steels.

Steel Type	Equation	References
Nb, Ti, and Nb-Ti	$X_{SRX} = 1 - exp[-0.693(t/t_{0.5\,SRX})]$ $t_{0.5\,SRX} = 9.92 \times 10^{-11} d_0 \varepsilon^{-5.6 d_0^{-0.15}} exp\left(\frac{180000}{RT}\right)\ exp\left[\left(\frac{275000}{RT} - 185\right) \times ([Nb] + 0.37[Ti])\right]$	**[80]** (Eq. 4.37)
Nb	$X_{SRX} = 1 - exp[-0.693(t/t_{0.5\,SRX})]$ $t_{0.5\,SRX} = 1.27 \times 10^{-18} \varepsilon^{-3.81} \dot{\varepsilon}^{-0.36} exp\left(\frac{404000}{RT}\right)$	**[35]** (Eq. 4.38)
Nb	$X_{SRX} = 1 - exp[-0.693(t/t_{0.5\,SRX})]$ $t_{0.5\,SRX} = (-5.24 + 550[Nb]) \times 10^{-18}\ \varepsilon^{(-4+77[Nb])} d_0^2 exp\left(\frac{330000}{RT}\right)$	**[75, 77]** (Eq. 4.39)
Nb-Ti	$X_{SRX} = 1 - exp[-0.288(t/t_{0.25\,SRX})]$ $for\ T > 990°C$ $t_{0.25\,SRX} = 1.5 \times 10^{-18} d_0^2 (\varepsilon - 0.025)^{-2.8} exp(30\ [Nb]) exp\left(\frac{300000}{RT}\right)$ $for\ T < 990°C$ $t_{0.25\,SRX} = 1.5 \times 10^{-18} d_0^2 (\varepsilon - 0.025)^{-2.8} exp(30\ [Nb]) exp\left(\frac{885000}{RT}\right)$	**[84]** (Eq. 4.40)
0.056Nb-0.158Mo	$t_{0.5\,SRX} = 2.1 \times 10^{-16} \varepsilon^{-3.1} \dot{\varepsilon}^{-0.43} d_0^2 exp\left(\frac{246000}{RT}\right)$	**[62]** (Eq. 4.41)
0.058Nb-0.283Mo	$t_{0.5\,SRX} = 6.0 \times 10^{-17} \varepsilon^{-3.1} \dot{\varepsilon}^{-0.43} d_0^2 exp\left(\frac{280000}{RT}\right)$	**[62]** (Eq. 4.42)
0.059Nb-0.161Mo 0.21Ni	$t_{0.5\,SRX} = 3.3 \times 10^{-16} \varepsilon^{-3.1} \dot{\varepsilon}^{-0.43} d_0^2 exp\left(\frac{261000}{RT}\right)$	**[62]** (Eq. 4.43)
0.059Nb-0.156Mo 0.5Ni	$t_{0.5\,SRX} = 7.4 \times 10^{-16} \varepsilon^{-3.1} \dot{\varepsilon}^{-0.43} d_0^2 exp\left(\frac{253000}{RT}\right)$	**[62]** (Eq. 4.44)
0.061Nb-0.157Mo 0.3Cr	$t_{0.5\,SRX} = 7.6 \times 10^{-15} \varepsilon^{-3.1} \dot{\varepsilon}^{-0.43} d_0^2 exp\left(\frac{230000}{RT}\right)$	**[62]** (Eq. 4.45)
0.062Nb-0.155Mo 0.61Cr	$t_{0.5\,SRX} = 5.8 \times 10^{-14} \varepsilon^{-3.1} \dot{\varepsilon}^{-0.43} d_0^2 exp\left(\frac{207000}{RT}\right)$	**[62]** (Eq. 4.46)

0.03Nb-0.151Mo	$t_{0.5\,SRX} = 4.0 \times 10^{-16}\varepsilon^{-3.1}\dot{\varepsilon}^{-0.43}d_0^2 exp\left(\frac{246000}{RT}\right)$	**[62]** (Eq. 4.47)
CMVN Steel	$X_{SRX} = 1 - exp[-0.693(t/t_{0.5\,SRX})]$ $t_{0.5\,SRX} = 1.57 \times 10^{-14}d_0^2\varepsilon^{-2.9}exp\left(\frac{271000}{RT}\right)$	**[23]** (Eq. 4.48)
C-Mn	$X_{SRX} = 1 - exp[-0.693(t/t_{0.SRX})^{0.9}]$ $t_{0.5\,SRX} = 9.25 \times 10^{-13}d_0^2\varepsilon^{-0.14}\dot{\varepsilon}^{-2}exp\left(\frac{140500}{RT}\right)$	**[57]** (Eq. 4.49)

Table 4.4: Equations to describe MDRX Kinetics for different steels.

Steel Type	Equation	References
Nb	$X_{MDRX} = 1 - exp[-0.693(t/t_{0.MDRX})]$ $t_{0.5\,MDRX} = 1.77 \times 10^{-6}\varepsilon^{-3.81}\dot{\varepsilon}^{-0.62}exp\left(\frac{153000}{RT}\right)$	**[76]** (Eq. 4.50)
Nb	$X_{MDRX} = 1 - exp[-0.693(t/t_{0.MDRX})^{1.1}]$ $t_{0.5\,MDRX} = 1.1Z^{-0.8}exp\left(\frac{230000}{RT}\right)$	**[1]** (Eq. 4.51)
Nb and C-Mn	$X_{MDRX} = 1 - exp[-0.693(t/t_{0.MDRX})^{1.1}]$ $t_{0.5\,MDRX} = 0.4Z^{-0.8}exp\left(\frac{240000}{RT}\right)$	**[85]** (Eq. 4.52)
0.056Nb-0.158Mo	$t_{0.5\,MDRX} = 8.4 \times 10^{-9}\dot{\varepsilon}^{-0.84}exp\left(\frac{186000}{RT}\right)$	**[62]** (Eq. 4.53)
0.058Nb-0.283Mo	$t_{0.5\,MDRX} = 1.0 \times 10^{-9}\dot{\varepsilon}^{-0.84}exp\left(\frac{209000}{RT}\right)$	**[62]** (Eq. 4.54)
0.059Nb-0.161Mo 0.21Ni	$t_{0.5\,MDRX} = 8.7 \times 10^{-9}\dot{\varepsilon}^{-0.84}exp\left(\frac{188000}{RT}\right)$	**[62]** (Eq. 4.55)
0.059Nb-0.156Mo 0.5Ni	$t_{0.5\,MDRX} = 1.1 \times 10^{-8}\dot{\varepsilon}^{-0.84}exp\left(\frac{187000}{RT}\right)$	**[62]** (Eq. 4.56)
0.061Nb-0.157Mo 0.3Cr	$t_{0.5\,MDRX} = 4.7 \times 10^{-8}\dot{\varepsilon}^{-0.84}exp\left(\frac{168000}{RT}\right)$	**[62]** (Eq. 4.57)

0.062Nb-0.155Mo 0.61Cr	$t_{0.5\,MDRX} = 2.4 \times 10^{-7}\dot{\varepsilon}^{-0.84} exp\left(\frac{148000}{RT}\right)$	**[62]** (Eq. 4.58)
0.03Nb-0.151Mo	$t_{0.5\,MDRX} = 4.3 \times 10^{-8}\dot{\varepsilon}^{-0.84} exp\left(\frac{160000}{RT}\right)$	**[62]** (Eq. 4.59)
Mo	$t_{0.5\,MDRX} = 6.66 \times 10^{-6}\dot{\varepsilon}^{-0.61} exp\left(\frac{123000}{RT}\right)$	**[72]** (Eq. 4.60)
Nb	$t_{0.5\,MDRX} = 4.42 \times 10^{-7}\dot{\varepsilon}^{-0.59} exp\left(\frac{153000}{RT}\right)$	**[72]** (Eq. 4.61)
Ti	$t_{0.5\,MDRX} = 8.90 \times 10^{-6}\dot{\varepsilon}^{-0.83} exp\left(\frac{125000}{RT}\right)$	**[72]** (Eq. 4.62)
CMVN Steel	$X_{MDRX} = 1 - exp[-0.693(t/t_{0.MDRX})]$ $t_{0.5\,MDRX} = 1.84Z^{-0.86} exp\left(\frac{271000}{RT}\right)$	**[23]** (Eq. 4.63)
C-Mn	$X_{MDRX} = 1 - exp[-0.693(t/t_{0.MDRX})^{1.1}]$ $t_{0.5\,MDRX} = 1.35 \times 10^{-12}\dot{\varepsilon}^{-0.25} exp\left(\frac{128000}{RT}\right)$	**[57]** (Eq. 4.64)

4.3 Effect of Alloying Elements

Sang-Hyun Cho et al. [62] studied the effects of alloying elements on the activation energy for DRX, SRX, and MDRX for seven chemical compositions of steels using regression analysis. The derived model for the activation energy for DRX is as follows:

$$Q_{DRX} = 297 + 641[\%Nb] + 123[\%Mo] + 1[\%Ni] - 111[\%Cr] \qquad \text{(Eq. 4.65)}$$

The predicted activation energy values were very comparable with hot torsion tests according to this equation, as shown in Figure 4.4.

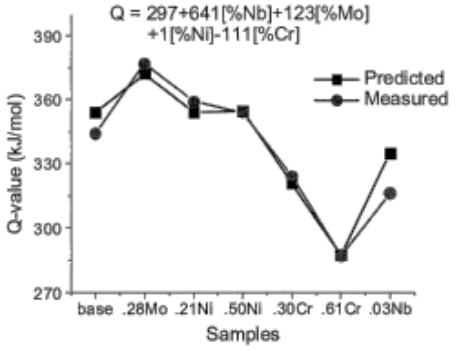

Figure 4.4: Comparison between the predicted and measured activation energies. [62]

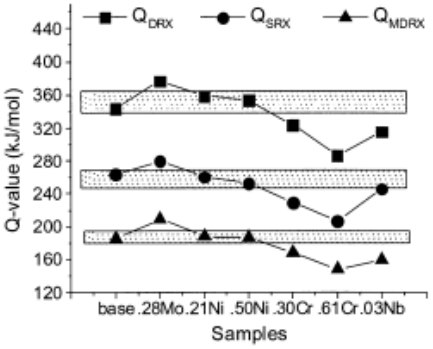

Figure 4.5: Predicted activation energies for DRX, SRX and MDRX for different steels. [62]

Similarly, the equations for activation energy for SRX and MDRX were also derived from the available data presented in Figure 4.5, as follows:

$$Q_{SRX} = 210 + 641[\%Nb] + 123[\%Mo] + 1[\%Ni] - 111[\%Cr] \quad \text{(Eq. 4.66)}$$

$$Q_{MDRX} = 130 + 641[\%Nb] + 123[\%Mo] + 1[\%Ni] - 111[\%Cr] \quad \text{(Eq. 4.67)}$$

4.4 Evolution of Grain Size

4.4.1 Recrystallized Grain Size

Many researchers have modeled the grain size for statically, meta-dynamically and dynamically recrystallized grains. The equations describing the recrystallized grain size are generally given by:

$$d_{sx} = a\varepsilon^b \dot{\varepsilon}^c d_0^d exp\left(\frac{q}{T}\right) \quad \text{(Eq. 4.68)}$$

$$d_{dx} = aZ^b \quad \text{(Eq. 4.69)}$$

$$d_{mx} = aZ^b \quad \text{(Eq. 4.70)}$$

The statically recrystallized grain size d_{SRX} is a function of the initial grain size and prior strain. While grain sizes produced by DRX and MDRX are dependent on Zener-Hollomon parameter [31, 86].

Observations regarding grain size produced by SRX:

- A small initial grain size produces higher dislocation density and nucleation rate leading to finer grain size [64].
- The final grain size decreases with increasing the applied strain.
- The dependence of SRX grain size on strain rate is weak [87].
- SRX grain size is independent of Z [87].

Observations regarding grain size produced by DRX:

- The dynamically recrystallized grain size d_{DRX} above the steady state strain can be decreased by increasing strain rate and decreasing deformation temperature [31].
- It is independent of initial grain size and a function of only temperature and strain rate [32, 88].
- DRX grain size increases as Z decreases [56].

Observations regarding grain size produced by MDRX:

- Larger grain compared to ones produced by DRX using the same strain rate [85].
- Finer grain size than grains produced by SRX [56].
- MDRX is highly influenced by temperature and strain rate while strain has insignificant effect on the grain size[87].

Table 4.5: Equations to estimate grain size after SRX for different steels.

Steel Type	Equation	References
Nb	$d_{SRX} = 1.1 d_0^{0.67} \varepsilon^{-0.67}$	**[7, 64]** (Eq. 4.71)
Ti-V	$d_{SRX} = 4.3 + 195.7 d_0^{0.15} \varepsilon^{-0.57} \left[exp\left(\frac{-350000}{RT}\right)\right]^{-0.11}$	**[89]** (Eq. 4.72)
Nb	$d_{SRX} = 472 d_0^{0.277} \varepsilon^{-0.7} \dot{\varepsilon}^{-0.1}\ exp\left(\frac{-48597}{RT}\right)$	**[90]** (Eq. 4.73)
C-Mn	$d_{SRX} = d_0^{0.4} \varepsilon^{-0.5} exp\left(\frac{45000}{RT}\right)$	**[91]** (Eq. 4.74)

Table 4.6: Equations to estimate grain size after DRX for different steels.

Steel Type	Equation	References
Nb steel	$d_{DRX} = 6.28 \times 10^{5} Z^{-0.35}$	**[63]** (Eq. 4.75)
C-Mn	$d_{DRX} = 1.6 \times 10^{4} Z^{-0.23}$	**[91]** (Eq. 4.76)
Nb	$d_{DRX} = 812 \times Z^{-0.13}$	**[56]** (Eq. 4.77)
Nb-0.31Mo	$d_{DRX} = 770 \times Z^{-0.13}$	**[56]** (Eq. 4.78)
Nb-0.15Mo	$d_{DRX} = 580 \times Z^{-0.13}$	**[56]** (Eq. 4.79)

Table 4.7: Equations to estimate grain size after MDRX for different steels.

Steel Type	Equation	References
Nb	$d_{MDRX} = 1370\varepsilon^{-0.67} exp\left(\frac{-45000}{RT}\right)$	**[92]** (Eq. 4.80)
Nb	$d_{MDRX} = 1400 \times \left\{\dot{\varepsilon}. exp\left(\frac{375000}{RT}\right)\right\}^{-0.13}$	**[76]** (Eq. 4.81)
Nb and C-Mn	$d_{MDRX} = 6.8 \times 10^4 Z^{-0.27}$	**[85]** (Eq. 4.82)
Mo	$d_{MDRX} = 1.66 \times 10^3 Z^{-0.16}$	**[72]** (Eq. 4.83)
Nb	$d_{MDRX} = 1.37 \times 10^3 Z^{-0.13}$	**[72]** (Eq. 4.84)
Ti	$d_{MDRX} = 3.97 \times 10^4 Z^{-0.42}$	**[72]** (Eq. 4.85)
C-Mn	$d_{MDRX} = 2.6 \times 10^4 Z^{-0.23}$	**[91]** (Eq. 4.86)

4.4.2 Partial Recrystallization

In the case of partial recrystallization between passes, some amount of strain is retained and must be added to the following pass. The accumulated strain can be calculated as follows [20]:

$$\varepsilon_i^a = \varepsilon_i + K_{acc}(1 - X_{i-1})\varepsilon_{i-1} \quad \text{(Eq. 4.87)}$$

K_{acc} is a constant linked to the rate of recovery and ranging from 0.5 to 1, which is high to low recovery rate [75].

Additionally, the resultant grain size is an average value of the partially recrystallized grains and the original grains. It can be calculated using the following expression [8, 75, 93]:

$$d_{0_{i+1}} = d_{i,rex} X_i^{4/3} + d_{0_i}(1 - X_i)^2 \quad \text{(Eq. 4.88)}$$

4.4.3 Grain Growth

Grain growth or coarsening is a mechanism that occurs during reheating of metals or after a complete recrystallization leading to reduction in grain boundary area, and therefore larger grain sizes. It is driven by the amount of energy stored in the grain boundaries when the material is held at a high temperature. Grain growth is a function of the initial grain size, time, temperature and the activation energy for grain growth. The general equation of isothermal grain growth is given by:

$$d^m = d_0^m + Kt \times exp\left(-\frac{Q_{gg}}{RT}\right) \quad \text{(Eq. 4.89)}$$

Where d_o is the initial grain size, commonly replaced by the grain size after the completion of 95% of recrystallization since grain growth can practically occur in fully recrystallized regions [93]. The grain size associated with grain growth is represented by d at time, t and temperature, T. The factor K is to include the specific energy of grain boundaries, and Q_{gg} is the grain growth activation energy.

The constant, m is the growth exponent and equal to 2 in theory. However, experimental observations concluded that this value is true for rapid growth rate associated with very short interpass times, i.e. less than one second [77]. After one second, the growth rate decreases and the value of m was found to be equal to 7 in several models [77]. For interpass times longer than 1000 seconds, Ouchi et al. [94] found that grain growth becomes insignificant.

With reference to Table 4.8, various models were proposed that take into account different grain growth rates following SRX, and DRX [77, 95]. This difference in kinetics of SRX and MDRX following DRX is associated with the absence of nucleation in MDRX as grains are produced and fully formed at the very beginning of the interpass time. While newly nucleated grains in SRX have a faster growth rate compared to fine grains formed by MDRX .

Table 4.8: Equations to estimate grain growth for different steels.

Steel Type	Equation	References
Nb	$d^{4.5} = d_0^{4.5} + 4.1 \times 10^{23} \times t_{ip} \times exp(-435000/RT)$	**[95]** (Eq. 4.90)
Ti	$d^{10} = d_0^{10} + 2.6 \times 10^{28} \times t_{ip} \times exp(-437000/RT)$	**[95]** (Eq. 4.91)
V	$d^{7} = d_0^{7} + 1.45 \times 10^{27} \times t_{ip} \times exp(-400000/RT)$	**[95]** (Eq. 4.92)
C-Mn	$t_{ip} < 1\ s$ $d_{gg,SRX}^2 = d_{SRX}^2 + 4.0 \times 10^7 (t_{ip} - 4.32 t_{0.5\ SRX}) exp(-113000/RT)$ $d_{gg,MDRX}^2 = d_{MDRX}^2 + 1.2 \times 10^7 (t_{ip} - 2.65 t_{0.5\ MDRX}) exp(-113000/RT)$ $t_{ip} > 1\ s$ $d_{gg,SRX}^7 = d_{SRX}^7 + 4.0 \times 10^{27} (t_{ip} - 4.32 t_{0.5\ SRX}) exp(-400000/RT)$ $d_{gg,MDRX}^7 = d_{MDRX}^7 + 8.2 \times 10^{25} (t_{ip} - 2.65 t_{0.5\ MDRX}) exp(-400000/RT)$	**[77, 93]** (Eq. 4.93)
Cr-Ni	$d^{1/0.2432} = d_0^{1/0.2432} + 1.72 \times 10^{21} \times t_{ip} \times exp[-5000 \times (70.44 + 4.37X_C + 3.99X_{Mn} + 1.44X_{Cr} + 1.48X_{Ni}) /RT]$	**[96, 97]** (Eq. 4.94)

4.5 Precipitation Effects

The addition of carbonitride forming elements retards the recrystallization process because of pinning effect of strain-induced precipitates and the solute drag resulting from microalloy additions. Elements such as niobium or titanium can form stable alloy carbonitrides in austenite. The precipitation process has been explained by some researchers based on the type of solute atom [98] or strain-induced precipitation which have major effects on the retardation of recrystallization [99-102]. Solute atoms or precipitates formed on grain boundaries can create a considerable drag force that retards the motion of dislocations or boundaries [103-105].

There are two types of precipitation namely static and dynamic precipitation. The static precipitation occurs after deformation or in undeformed austenite. While dynamic precipitation occurs during deformation and it is called strain-induced which produces very fine precipitates of sizes around 5 nm and impact the rate of work hardening [106].

Jonas and Weiss [107, 108] determined the kinetics of precipitation after deformation using hot compression testing. It was found that recrystallization was delayed by more than an order of magnitude in time when precipitation forming process started before. They observed that presence of solute atoms at high temperatures and precipitates at the low temperatures contribute to the retardation of recrystallization.

Dutta and Sellars [109] proposed a model to describe the isothermal strain-induced precipitation of Nb carbonitride from supersaturated austenite. The precipitation start time is a function of strain, strain rate, temperature, Nb carbonitride solubility and super-saturation ratio (K_s) as follows:

$$t_{ps}^{DS} = A\, Nb^{-1}\varepsilon^{-1}Z^{-0.5}exp\left(\frac{270000}{RT}\right)exp\left(\frac{2.5\times10^{10}}{T^3\ ln(K_s^2)}\right) \qquad \text{(Eq. 4.95)}$$

A: represents the number of precipitate nuclei per unit volume, equal to 3×10^{-6} in DS model.

The super-saturation ratio describes the driving force for precipitation or the amount of Nb and C in solution at specific temperature compared to the reheating temperature which can be calculated as follows [110]:

$$K_s = \frac{10^{-6770/T_{RH}+2.26}}{10^{-6770/T_{Pass}+2.26}} \quad \text{(Eq. 4.96)}$$

Where T_{RH} and T_{Pass} are the reheating and pass temperatures in Kelvin, respectively.

Si and Mn addition retard precipitation so the precipitation start time can be corrected as follows [111]:

$$t_{ps} = \frac{t_{ps}^{DS}}{10^{(-0.26-0.90Mn+2.85Si)}} \quad \text{(Eq. 4.97)}$$

Nb carbonitride solubility product can be computed using an equation proposed by Irvine et al. as follows [110]:

$$log\ Nb \times \left(C + \frac{12}{14}N\right) = 2.26 - \frac{6770}{T} \quad \text{(Eq. 4.98)}$$

The above equation was modified by Siciliano and Jonas [20] to include the effect Si and Mn concentration:

$$log\ Nb \times \left(C + \frac{12}{14}N\right) = 2.26 + \frac{838Mn^{0.246} - 1730Si^{0.594} - 6440}{T} \quad \text{(Eq. 4.99)}$$

The parameter A was formulated by Siciliano and Jonas [20] to include the effect of the chemical composition:

$$A = \frac{\left(\frac{Mn}{Si}\right)^{0.42} exp\left(\frac{0.42Nb}{C}\right)}{169000} \quad \text{(Eq. 4.100)}$$

S.G. Hong et al. [112] studied the precipitation start time (Ps) of strain-induced NbC carbides in low carbon Nb-Ti steel using two-stage isothermal interrupted compression tests with different holding times and then measuring the softening ratio. It was observed that the precipitation is delayed for Nb-Ti steel compared to Nb steel due to the insufficient solution of Nb during reheating and the heterogeneous nucleation of (Nb,Ti)C carbides.

As shown in Table 4.9, At 975°C, the softening ratio reaches maximum of 90% prior to precipitation when the holding time is about 28s; After that, precipitates start to form

and finish at 120s. Table 4.9 lists the maximum softening ratios, precipitation start and finish times at different temperatures.

Table 4.9: The estimated precipitation start and finish times as well as the maximum softening ratio before precipitation starts for Nb-Ti steels using different holding times. [112]

Temperature	Maximum softening ratio	Precipitation start time, Ps in sec	Precipitation finish time, Pf in sec
975	90%	28	900
950	35%	40	600
900	22%	15	400
850	18%	20	1000

CHAPTER-5

Experimental Materials & Procedure

Hot torsion was used to study the hot deformation behavior of industrial HSLA grades. The so called 'average' deformation schedules were used in which strain per pass, strain rate, interpass time and cooling rate are kept constant throughout the test. Average schedules are commonly used to obtain basic information about the hot deformation behaviour, since analysis of the flow behaviour is more straightforward than for a 'real' rolling schedule. In this study, different time gaps, i.e. the interval between roughing and finishing in an industrial rolling schedule, were incorporated into these average schedules to investigate the effect on MFS behavior in the finishing schedule.

5.1 Experimental Materials

For this study two industrial HSLA steels were cast and rolled in the SABIC – Hadeed hot strip reversing mill (HSM), Saudi Arabia. The chemical compositions of these steels are shown in Table 5.1.

Table 5.1: Chemical Compositions of the Investigated Steels in Weight Percent

Steel	C	Mn	Si	Nb	Ti	Cr	Mo	V	Ni	N
A	0.0490	1.540	0.189	0.0530	0.0170	0.0130	0.165	0.014	0.034	0.0066
B	0.0541	1.566	0.180	0.0846	0.0165	0.1639	0.000	0.015	0.138	0.0062

Steels A and B are of grade X65 and X70, respectively. Both are used for pipeline operating pressures that require high strength and high toughness at low temperatures (from 0 to -10°C). These requirements are traditionally produced using low C-Mn-Mo-Nb chemistry as in Steel A to obtain steel microstructure that is based on ferrite/acicular ferrite. Recently, an alternative unique chemistry named HTP, i.e. High Temperature Processing, has been used to produce ferrite/acicular ferrite microstructure using higher Nb contents and without the use of molybdenum, as in Steel B. The high Nb has the unique capability to use higher thermo-mechanical processing temperatures since it has enough solute Nb to retard recrystallization at elevated temperatures and therefore produce a finer ferrite/acicular microstructure. The absence of Mo in HTP chemistries has

several advantages in terms of steel cost and properties, such as keeping hardness below 260 HV10 and better weldability [113]. The other differences are the higher carbon content and the presence of Ni and Cr in Steel B; these elements enhance the strength required for grade X70. Table 5.2 presents the mechanical data for both steels in the as-hot rolled condition, which was obtained using samples at 30° relative to rolling direction.

Table 5.2: Mechanical data of Steel A and B as received from the steel supplier.

Steel	Yield Strength, MPa	Tensile Strength, MPa	Hardness, HV10	Elongation, %
A	570	658	215	40
B	605	697	238	36

5.2 McGill Hot Torsion Machine

Hot torsion experiments were carried out in a computer-controlled MTS machine at McGill. The main components of this machine are shown in Figure 5.1 and can be summarized as follows [61, 114]:

1. **Potentiometer**: to measure the twist angle and provide feedback signals for the hydraulic servo valve.
2. **Hydraulic servo valve**: to control the rotation of the hydraulic motor.
3. **Hydraulic motor:** to drive the torsion machine with a maximum torque capacity of 100 N-m and rotational speed of 628 rpm.
4. **Rotating torsion bar:** to twist the specimen
5. **Radiant furnace**: a water cooled furnace with four radiant elements to allow temperatures up to 1200 °C.
6. **Quartz tube**: the specimen is placed inside a tube protected by argon gas passing through it to avoid oxidation at high temperatures.
7. **Stationary grips**: the specimen is held by nickel-based superalloy grips and screwed into a threaded slot on the rotating torsion bar.
8. **Torque cell**: attached to the stationary grips to measure the applied torque.

9. **Control system**: consists of two devices: MTS TestStar interface and a program installed in a computer which provides digital control of the required test parameters.

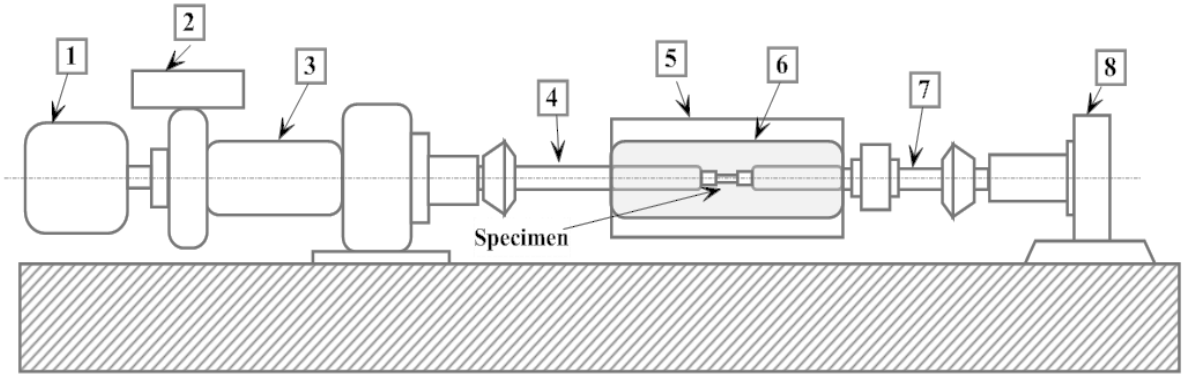

Figure 5.1: Schematic diagram of the main components of the hot torsion machine.

5.3 Hot Torsion Specimen

The specimens were machined from the as-hot rolled 16mm plate transverse to rolling direction. The specimen dimensions were 22.2 mm in length and 6.4 mm diameter as shown in Figure. 5.2.

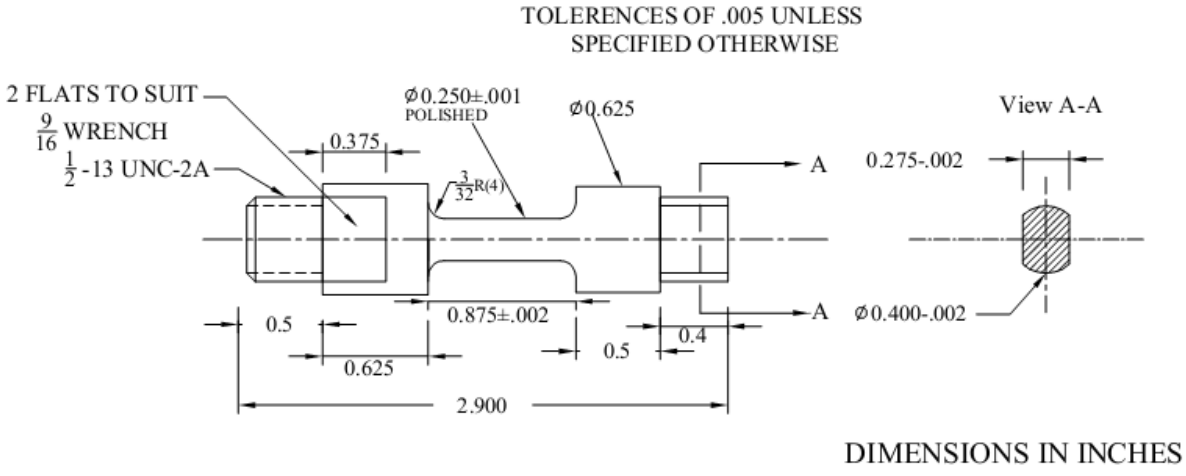

Figure 5.2: Schematic diagram of the hot torsion specimen (in inches).

5.4 Calculation of Stress and Strain based on the Experimental Data

The measured torque and twist were converted to von Mises effective stress and strain using the following formulas [15]:

$$\sigma = 3.3\sqrt{3} \quad Torque/2\pi R \qquad \text{(Eq. 5.1)}$$

$$\varepsilon = (\theta . R)/(\sqrt{3}\, R) \qquad \text{(Eq. 5.2)}$$

Where R,L,θ are the gauge radius, length and the twist angle in radians.

5.5 Testing Schedules and the Designation System Used in this Work

Different testing schedules were comprised of a reheating of the specimens to 1200°C to ensure the dissolution of precipitates, followed by continuous cooling the specimens and deformation at 3 /s strain rate of 0.2 strain per pass, keeping the interpass time constant. Three types of time gap between roughing and finishing were used; (i) no time gap; (ii) a time gap in which roughing is stopped at the T_{nr} and therefore finishing begins well below the T_{nr} revealed by time gap schedule and (iii) a time gap resulting in finishing beginning at the T_{nr} of the no time gap schedule. For the no time gap type, two different interpass times were used – 5 and 30 s. For the time gap schedules, the interpass time was 5 s, and different time gaps of 10, 20 and 45 were used.

All schedules used follow a specific designation system which can be clarified in four points:

1. **Steel type:** comes at first, and it is either A for Steel A or B for Steel B.
2. **Type of time gap: NTG**: No time gap, **TGH**: Time gap at high temperature range in which roughing stops above the T_{nr} temperature and finishing resumes at the T_{nr} temperature, **TGL:** Time gap at low temperature range in which roughing stops at the T_{nr} temperature and finishing resumes below the T_{nr} temperature
3. **Time gap** (45, 20 or 10 seconds) in case of TGH and TGL schedules.
4. **Interpass time:** is represented by the last number (-5 or -30), either 5 or 30 seconds.

To summarise, the following line simplifies the order of the last four points:

(Steel Type) - (Type of time gap) (Time Gap) - Interpass time

The designations for all schedules for both steels are tabulated in Table 5.3.

Table 5.3: The designation for all schedules and steels used in this work

Type of time gap	NTG	TGH		TGL	
Description	No time gap	Time gap at high temperature range (finishing at T_{nr})		Time gap at low temperature range (finishing below T_{nr})	
Interpass time	5 and 30 seconds, respectively	5 seconds only			
Steel A	Designation	Time gap	Designation	Time gap	Designation
	A-NTG-5	45	A-TGH45-5	45	A-TGL45-5
	A-NTG-30	20	A-TGH20-5	20	A-TGL20-5
	---	10	A-TGH10-5	10	A-TGL10-5
Steel B	B-NTG-5	45	B-TGH45-5	45	B-TGL45-5
	B-NTG-30	20	B-TGH20-5	20	B-TGL20-5
	---	10	B-TGH10-5	10	B-TGL10-5

Detailed results are given in the following sections.

Chapter 6

Results & Discussion

6.1 Case I: No Time Gap (NTG)

Two interpass times were used: 5 and 30 seconds. The longer 30 s interpass time is more representative of roughing in a reversing roughing mill because the hot rolled slab has to travel all the way to clear the roll gap and reverse its direction. The shorter interpass time is more indicative of finishing since reductions take place in a tandem mill. For this case, deformation begins at 1170°C and ends at 820°C with a constant interpass time throughout the deformation schedule. No time gap was incorporated and deformation for all the passes was at 3 /s strain rate of 0.2 strain per pass. For the 5s interpass time, the number of passes was 28, which leads to a cooling rate of 2.6 °C/s; for the 30s interpass time, the number of passes was 21 and the cooling rate 1 °C/s.

6.1.1 Long Interpass Time of 30 Seconds (NTG-30)

Figure 6.1 shows the MFS behaviour for both steels using interpass time of 30 seconds. For the current experiments, the MFS behavior is very similar for both steels with on average 8.2% higher MFS values for Steel B. This is probably a reflection of the higher alloying level in Steel B particularly the higher amount of Nb. According to Andrade et al [115], it was concluded that an individual addition of niobium has a much greater effect on high temperature strengthening compared to molybdenum. Therefore, over the hot deformation range of Figure 6.1, Steel B has a higher MFS.

Recrystallization, strain-induced precipitation hardening and strain accumulation are the main factors affecting the MFS. If precipitation occurs, recrystallization would stop, leading to an accumulation of strain. Additionally, precipitation hardening would also contribute to a higher MFS. Therefore, it is important to determine the temperature at which recrystallization stops, i.e. the recrystallization stop temperature (T_{nr}), in order to determine when static recrystallization, strain-induced precipitation and strain accumulation occur; this would facilitate the modelling of the MFS behaviour.

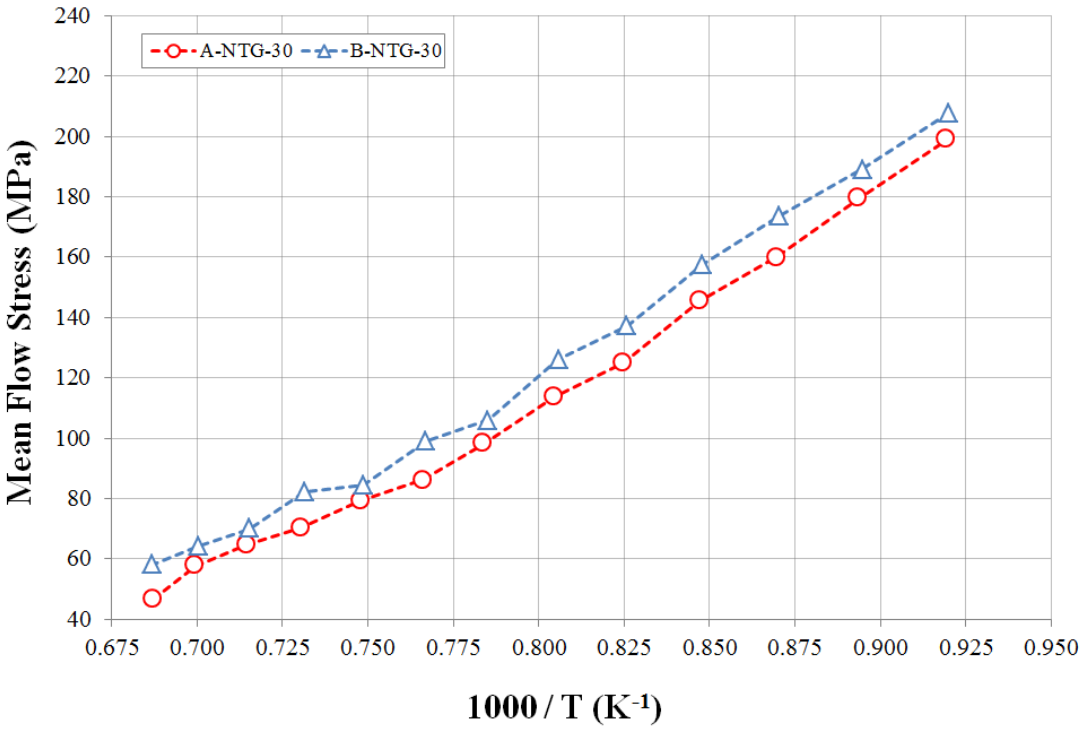

Figure 6.1: MFS behaviour interpass time of 30 seconds for the two steels.

The conventional method of locating the temperature of no recrystallization is by fitting linear relationships to the roughing and finishing regions and defining the T_{nr} as the intersection between these two slopes. This method was used to approximate the T_{nr} temperature for Steels A and B in the case of 30 second interpass times, as shown in Figures 6.2 and 6.3. The T_{nr} temperatures for steels A and B are 1003 and 1010°C, respectively. This result shows that there is no significant difference between the two steels in terms of the precipitation kinetics and their influence on the MFS, in this hot deformation schedule, even though there is more Nb in steel B.

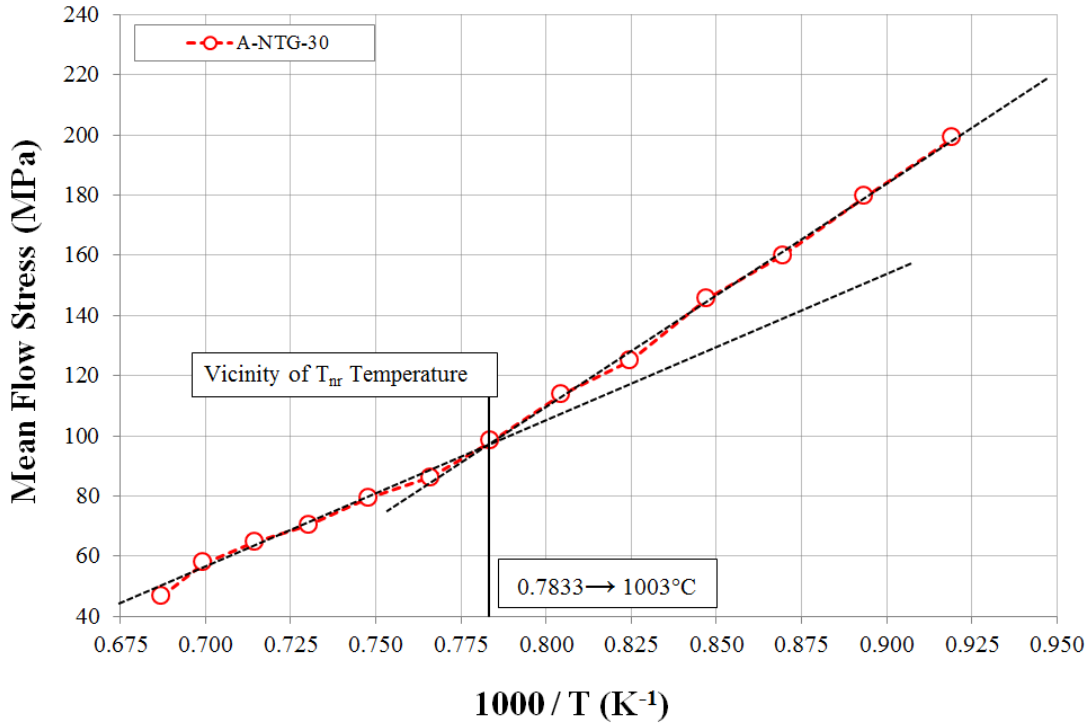

Figure 6.2: The vicinity of T_{nr} temperature for Steel A (1003°C).

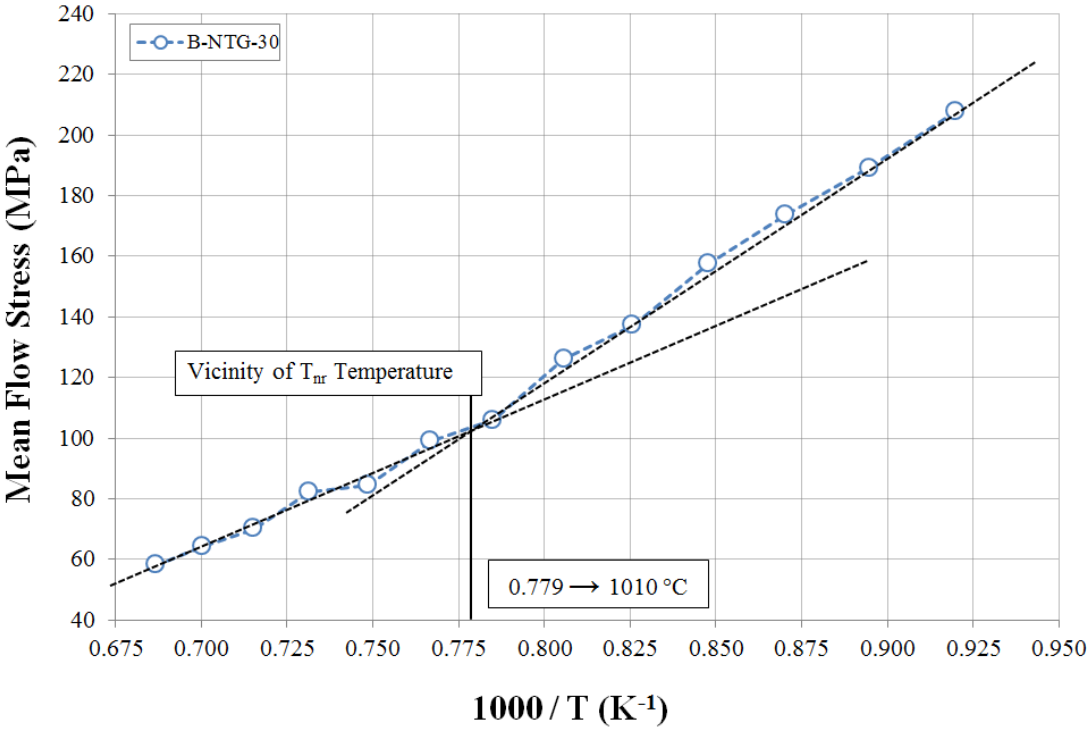

Figure 6.3: The vicinity of T_{nr} temperature for Steel B (1010°C).

6.1.2 Short Interpass Time of 5 Seconds (NTG-5)

The deformation variables were selected to be identical to the ones used previously except the interpass time was reduced to 5 seconds. Figure 6.4 shows that the MFS values for both steels are close at high temperatures but diverge as the temperature decreases. This is probably related to faster precipitation kinetics in Steel B, as will be discussed in the following pages.

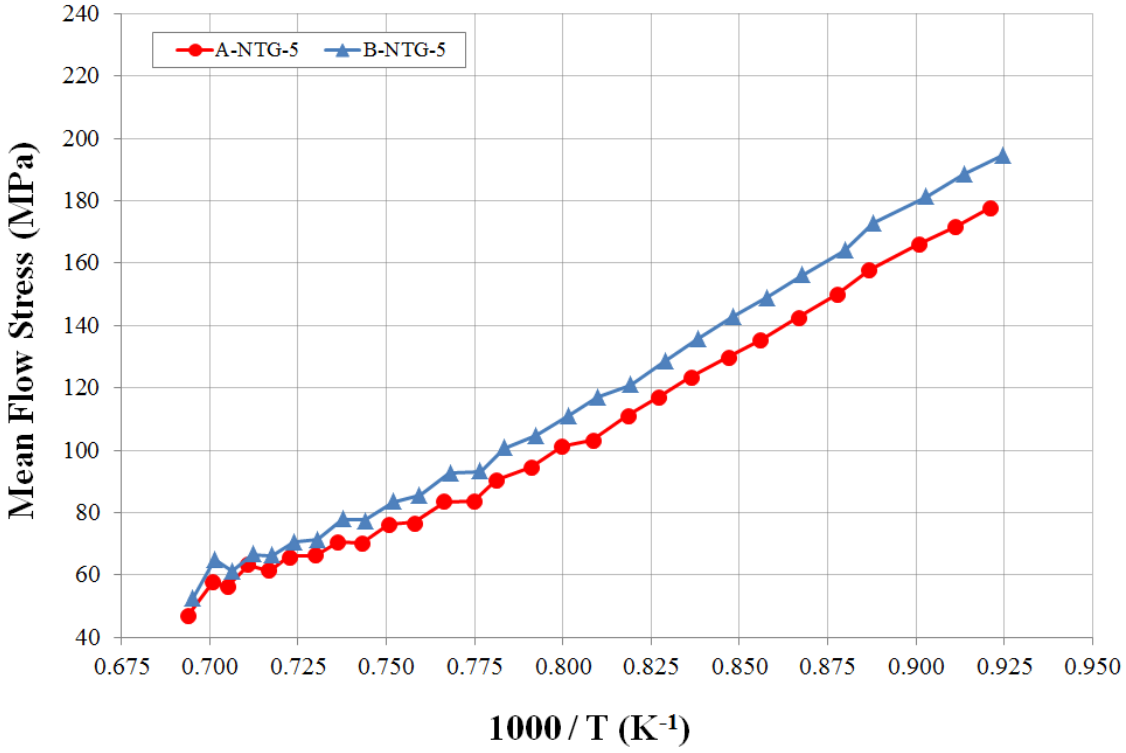

Figure 6.4: MFS behaviour interpass time of 5 seconds for the two steels.

For this short interpass time, it is quite difficult to accurately determine the T_{nr} temperature using the previous method because there is a gradual transition from full recrystallization to no recrystallization. This gradual transition leads to the presence of several points that are very close to the intersection of the two slopes corresponding to full recrystallization and full work hardening regions as shown in Figures 6.5 (a and b). Hence, the intersection between the two lines can be located anywhere within a wide range that approximates the T_{nr} temperature.

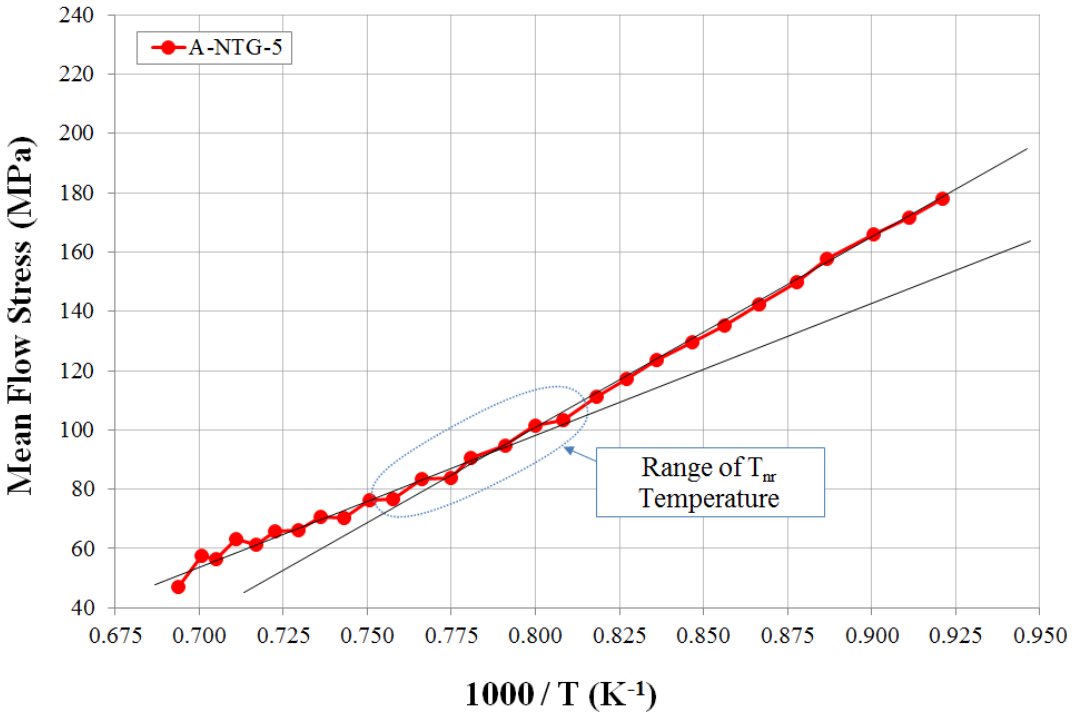

(a) Steel A

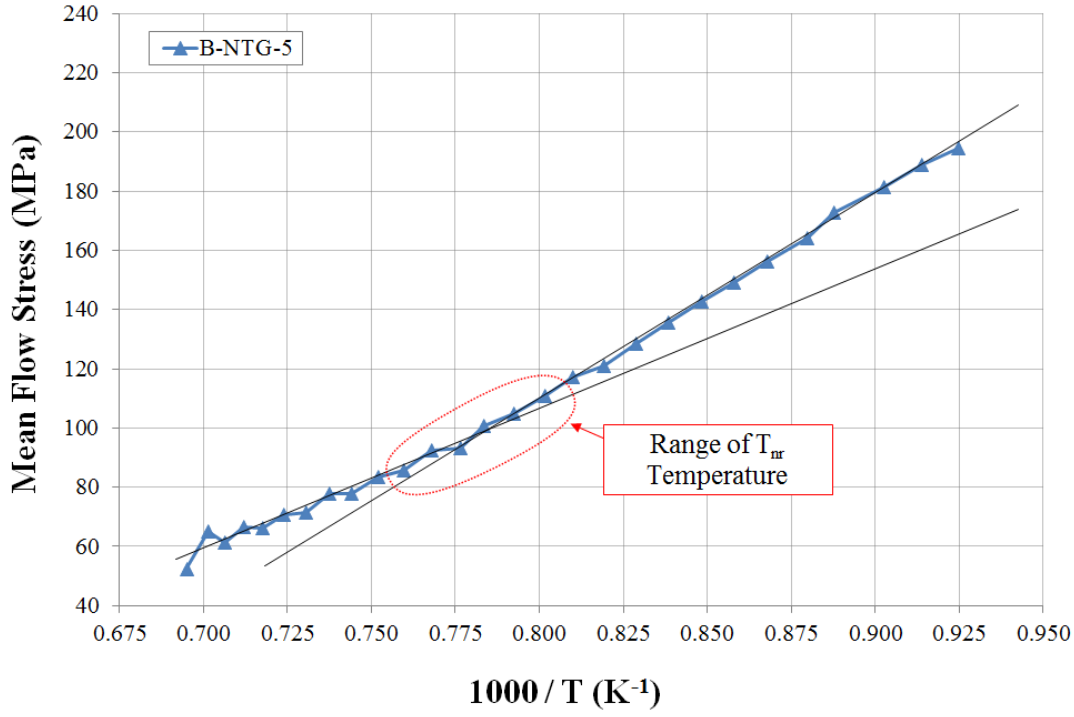

(b) Steel B

Figure 6.5: The wide range of possible T_{nr} temperatures using the conventional method.

Therefore, a new method for determining the T_{nr} temperature with a better resolution is proposed as follows. With reference to Figure 6.6, which is a 'magnification' of the high temperature region of Fig. 6.4, note that there is a systematic rise and fall of the MFS in the roughing stage superimposed on the general increase in MFS with decreasing temperature. This indicates that strain is accumulated after the 1st pass. When an additional strain of 0.2 is imposed in the 2nd pass, this leads to higher strain value which allows faster recrystallization between the 2nd and the 3rd passes. Similarly, the strain is accumulated at the 3rd pass and when the strain is applied at the 4th pass, recrystallization occurs between the 4th and the 5th pass. As precipitation occurs below the T_{nr}, recrystallization stops and this 'fluctuating' behavior vanishes at lower temperatures. According to this concept, the temperature of no recrystallization is the point at which the fluctuating behaviour stops, which is at 964 and 1003°C for Steels A and B, respectively. Contrary to the NTG-30 schedule, the NTG-5 schedule reveals that Steel B has a significantly higher T_{nr} than Steel A.

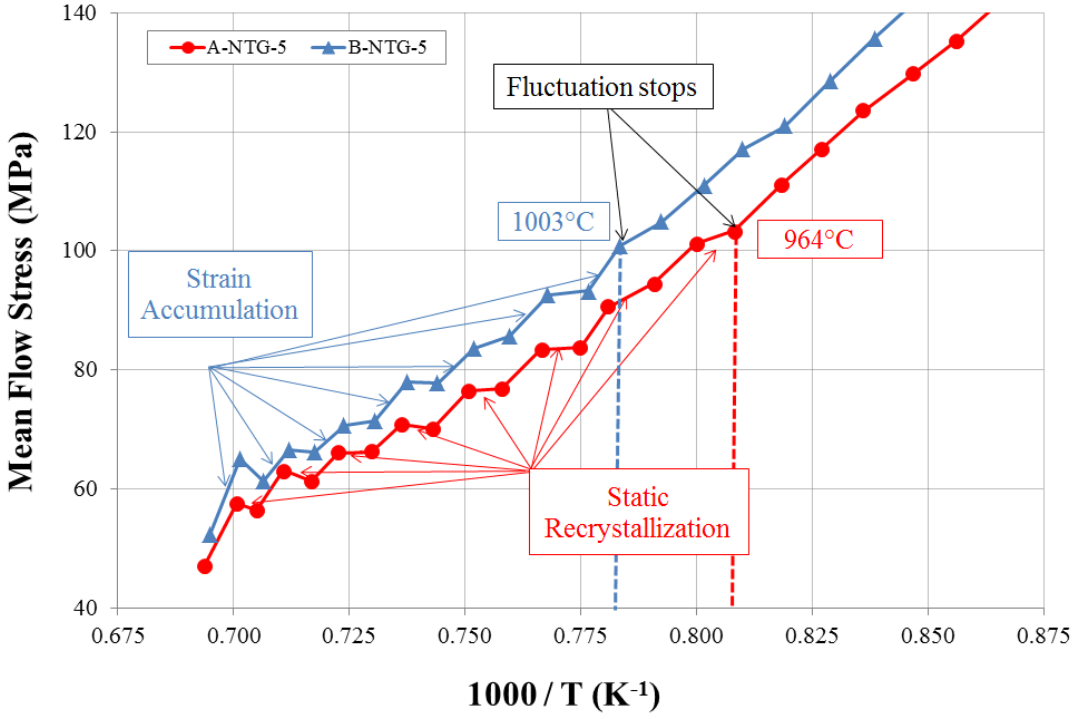

Figure 6.6: The fluctuating behavior at high temperature for Steel A and B indicating regions where strain accumulation and static recrystallization dominate

6.1.3 Comparison of NTG 30 and NTG-5 schedules

Compared to NTG-30, it was observed that the T_{nr} temperature for NTG-5 was decreased for both steels. The reason for that is probably the faster cooling rate used in NTG-5 schedule pushing the precipitate start temperature to lower values. The effect of NTG-5 is greater for Steel A than Steel B, i.e. the T_{nr} is much more decreased in Steel A. This may be due to faster precipitation kinetics of Steel B offsetting the cooling rate effect because of the presence of the higher Nb content.

For both steels, the responsible mechanism for the occurrence of T_{nr} is a combination of solute drag and precipitate pinning. For short interpass time, i.e. normally less than 10 seconds, the occurrence of T_{nr} is associated with either strain-induced precipitates of Nb(C,N) or with Nb solute drag [116]. Some workers observed that recrystallization is delayed by solute drag in Nb steels [108, 117, 118]. The effects of solute on MFS behaviour has been a controversial topic by many researchers. Andrade et al. [115] studied the solute effects and its role on static recrystallization and consequently MFS behaviour. Double hit isothermal compression testing was performed by Andrade et al. [115] on different steels to characterize the solute effects at 1000, and 900°C using different holding time. Table 6.1 shows the recrystallization start and finish times for plain carbon, Mo and Nb steels at two temperatures.

Table 6.1: The recrystallization start and finish times for different steels at 1000 and 900°C [115]

Steel	1000°C		900°C	
	R_s (s)	R_f (s)	R_s (s)	R_f (s)
Plain C	0.3	7.0	1.9	30
Mo	1.0	27.0	9.0	200
Nb	1.9	38.0	90.0	2800

The results in reference [115] show an evidence of the presence of solute effects prior to strain induced precipitation for Mo and Nb steel. The recrystallization start time for plain carbon steel at 1000 is 0.27s while Nb steel is delayed to 1.9s. The only possible reason for this delay proposed by Andrade et al. is the retardation effect of niobium as solute before precipitation starts. On the other hand, the recrystallization start time is 90s

at 900°C for Nb steel in which both strain-induced precipitate and solute effects contribute to this delay [115].

Bai et al [119] studied the effect of interpass time on T_{nr} temperature for different Nb bearing steels using hot torsion tests with a constant strain rate of 2 s^{-1} , a constant strain of 0.3/pass and different interpass times ranging from 5 to 200s, and suggested the following mechanisms [119]:

1. For interpass times below 12s, recrystallization is retarded by the solute drag effect since precipitation is unable to take place. In this range, the T_{nr} *decreases* with increasing the interpass time, because there is more time for recrystallization.
2. For interpass times between 12 and 50s: precipitation is expected to occur and the T_{nr} *increases* with increasing interpass time as a result of the increasing volume fraction of precipitates.
3. For interpass times above 50s: precipitation coarsening is expected which leads to a *decrease* in the T_{nr} with increasing interpass time.

According to this classification, increasing the interpass time from 5s to 30s would decrease the T_{nr} temperature only if the solute effect was the mechanism responsible for retarding recrystallization in NTG-30 schedule. However, the T_{nr} increased in NTG-30, which means that it occurred due to precipitation. For the NTG-5 schedule, the T_{nr} might have occurred due to solute effect, precipitation or both combined, which could be verified by running further experiments at slightly higher interpass times.

For Nb-Ti steels, Hong et al [112] reported that the solute effects range should be even more than 12 seconds that were originally determined for Nb bearing steels because of the presence of Ti. Precipitation start time of strain-induced NbC carbides in Nb-Ti steels is delayed because of two reasons. Firstly, incomplete dissolution of (Ti, Nb) (C,N) carbonitrides during reheating since they are very stable at high temperature. Secondly, the undissolved (Ti, Nb) (C,N) carbonitrides acted as nucleation sites for the (Nb,Ti)C carbides. Therefore, some amount of niobium (8-14%) is lost in the undissolved (Ti, Nb) (C,N) carbonitrides during reheating as well as after the first prestrain. This results in a delay of precipitation of strain-induced NbC carbides forming in the matrix of Nb-Ti steels [112].

The T_{nr} temperatures for both interpass times and the two steels are presented in Table 6.2. Steel A with 5 second interpass leads to the lowest T_{nr} because it has lower niobium content and less time to form precipitates. While Steel B with 30 interpass time has the highest T_{nr} since it has higher niobium compared to Steel A and longer interpass time for precipitation compared to 5 seconds. However, note that there is little effect of interpass time on Steel B, which suggests that 0.084% Nb is a 'critical' level of Nb above which there may be no effect of hot deformation parameters. This is important if Nb additions are being made to increase the pancaking window by increasing the T_{nr}.

One interesting observation is that the T_{nr} for Steel A-NTG-30 and Steel B-NTG-5 is exactly 1003°C. In fact the MFS vs 1000/T behaviour is also identical, as can be seen in Figure 6.7. This is interesting but at this point is merely a coincidence.

Table 6.2: Summary of approximate values of T_{nr} temperatures for Steel A and B using short and long interpass times.

	Vicinity of Temperature of no recrystallization	
Interpass time	Steel A	Steel B
5	964	1003
30	1003	1010

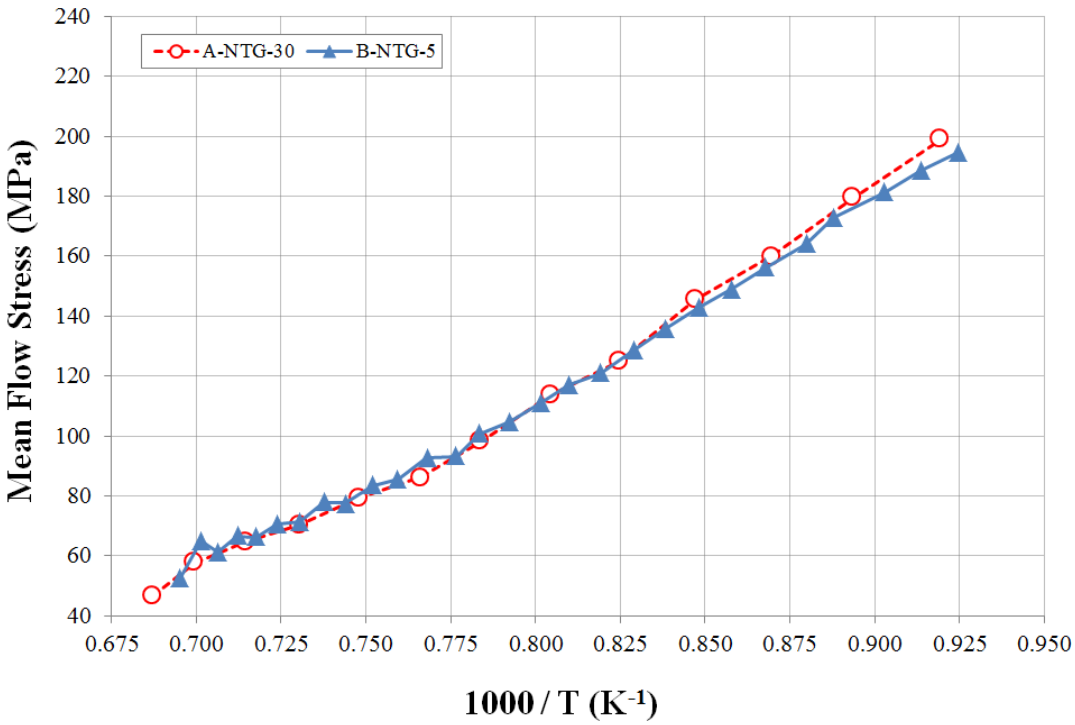

Figure 6.7: MFS behaviours of Steel A and B with 30, and 5 seconds interpass times, respectively.

As well, there is an effect of interpass time on the fluctuating MFS behaviour at high temperatures which is seen in the 5s interpass time, but not in the 30s one. This fluctuating behaviour is due to cycles of partial recrystallization, because the short interpass time does not lead to full recrystallization in the high temperature range, and this is followed by strain accumulation leading to full recrystallization in the following deformation pass.

Finally, Figures 6.8 and 6.9 show the difference in MFS behaviour due to the different interpass times for the two steels. Basically, there is no significant effect at high temperatures where there is full recrystallization, but the MFS for the 30s interpass time is always higher than for the 5 s one at low temperatures. Since there is no recrystallization at these temperatures for both interpass times, the MFS difference is probably due to precipitation strengthening with more precipitates formed during the longer interpass times.

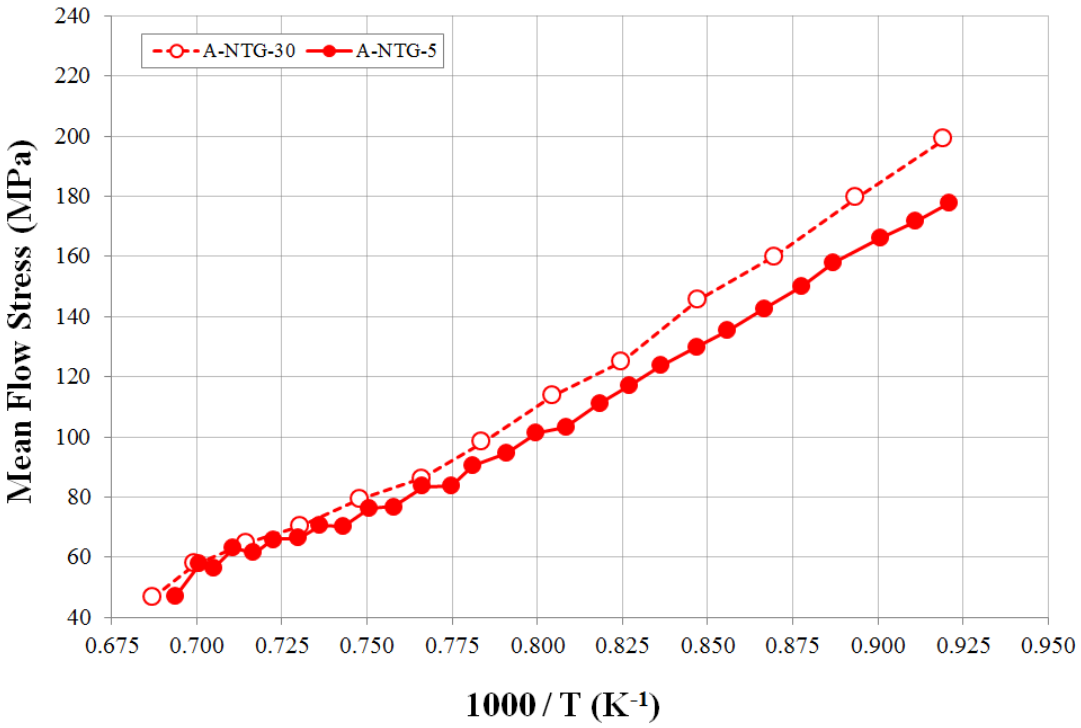

Figure 6.8: The influence of using long interpass time on MFS values starts at the 7th pass (around 1003°C) for Steel A

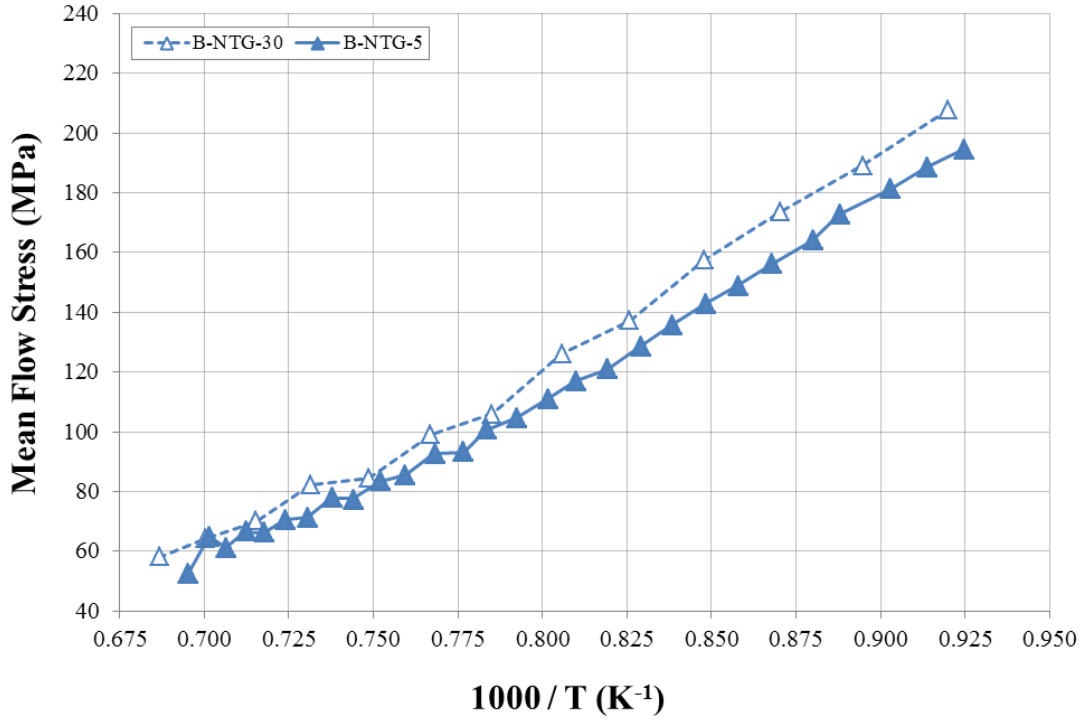

Figure 6.9: The influence of using long interpass time on MFS values starts at the 7th pass (around 1010°C) for Steel B

6.2 Case II: Time Gap Incorporated at Low and High Temperature Ranges (TGL & TGH)

These are based on NTG schedule with 5 second interpass times and different time gaps of 45, 20, and 10 seconds. The **TGL** schedule was designed so that the final pass of roughing was performed close to the T_{nr} temperature, as determined from the NTG-5 schedule, and the first pass of finishing followed after the time gap. While the **TGH** schedule was designed so that the final roughing pass was stopped at a temperature such that the first finishing pass, executed after the time gap, was performed at the T_{nr} temperature. Table 6.3 shows the 12 deformation schedules for Steel A and B using time gaps of 10, 20 and 45 seconds. This table also indicates T_{nr} temperatures for these schedules, which will be explained below.

Table 6.3: The deformation schedules including time gaps. The T_{nr} values are due to the presence of fluctuations with respect to the temperatures of the last roughing and the first finishing passes for the two steels

Steel	Schedule	Time Gap	RL Temp*	F1 Temp	Fluctuate after F1?	T_{nr}
A	TGL	45	966	842		842
		20	965	912		912
		10	967	939	Y	911
	TGH	45	1089	971		971
		20	1020	968	Y	889
		10	993	967	Y	910
B	TGL	45	994	873		873
		20	993	939	Y	911
		10	998	969	Y	912
	TGH	45	1112	1005		1005
		20	1048	994	Y	911
		10	1022	996	Y	911

* RL Temp: The temperature of the last roughing pass

From the previous findings of the average schedules, the fluctuations in NTG-5 represent the extent of recrystallization and the T_{nr} temperature can be approximated by the last point at which the fluctuations stop [Section 6.1.2]. With reference to Table 6.3, three points can be noted:

1. For all schedules with the time gap of 10 and 20 seconds, it was observed that the T_{nr} temperatures are, with the exception of A-TGL20, all very close to each other (911-912°C) which are lower than 964 and 1003°C determined by NTG-5 schedules. This may be due to delayed precipitation, as will be explained below.

2. For A-TGH20, the T_{nr} decreased to even lower temperature of 889°C. This may be related to the highest softening occurring during the time gap.

3. For 45 seconds time gap, precipitation was able to take place during the time gap leading to an increase in the T_{nr} temperature in all cases.

With reference to Figure 6.10 (a,b) and 6.11 (a,b), the time gap results in the following observations:

1. Mean flow stress fluctuations are observed for 20 and 10s time gaps for all schedules and steels except for steel A TGL20. Therefore, as concluded in the no time gap experiments, the end of these fluctuations signifies the T_{nr} due to this combination of steel composition and deformation schedule. If it is assumed that the presence of fluctuations indicates either an absence of precipitates (at very high temperatures) or the presence of very few precipitates (close to the T_{nr}), then it appears that the time gap has slowed down precipitation kinetics. This would be due mainly to the absence of deformation in the time gap compared to the average schedule, where deformation would be taking place at the corresponding times and temperatures of the time gap. Increasing the time gap beyond a certain time decreases the temperature of the first finishing pass below a critical temperature, which would minimize or eliminate the extent of fluctuations (i.e. static recrystallization) in finishing due to very fine precipitation as a consequence of increasing the driving force for precipitation.

2. A drop in MFS values for the first passes of finishing stage below that predicted by extrapolating the MFS vs. 1000/T behaviour of the roughing stage, assuming full static recrystallization between roughing passes. As mentioned in the introduction, this lower than expected MFS may be due to grain coarsening during the time gap. However the presence of Ti should inhibit grain coarsening, On the other hand, as implied by the MFS fluctuations, it is clear that full recrystallization does not occur after each pass in roughing, despite the relatively high temperatures of roughing. Thus complete recrystallization takes place in the time gap, leading to an MFS which does not follow the MFS behaviour of the roughing stage.

3. There is a sudden jump in MFS from the 1^{st} to the 2^{nd} pass of the finishing stage for all of the time gap schedules. The MFS of the 2^{nd} pass is as predicted by the NTG5 schedule below the T_{nr}, i.e. during finishing. It is generally accepted that below the T_{nr}, the MFS is a strong function of work hardening, which is essentially a function of strain. In other words a large increase in MFS in a finishing pass should correlate with a large strain in that pass. However, the unpredictably large increase from the first finishing pass to the second in the schedules with time gaps are associated with strains that are the same as all other passes in finishing. Thus, this jump in MFS is probably associated with precipitation hardening allows the MFS to increase rapidly to a comparable value with the no time schedule in, for example, 3 passes only, compared with 10 passes in the case of no time gap, (Figure 6.12). The time gap could lead to much finer precipitates by delaying precipitation to lower temperatures, in this way increasing the driving force for precipitation and increasing the kinetics of precipitation. These finer precipitates would have an increased precipitation strengthening effect for a given volume fraction of precipitates. This precipitation effect is much lower in the TGH schedules because the 2^{nd} finishing pass is very close to the start of precipitation.

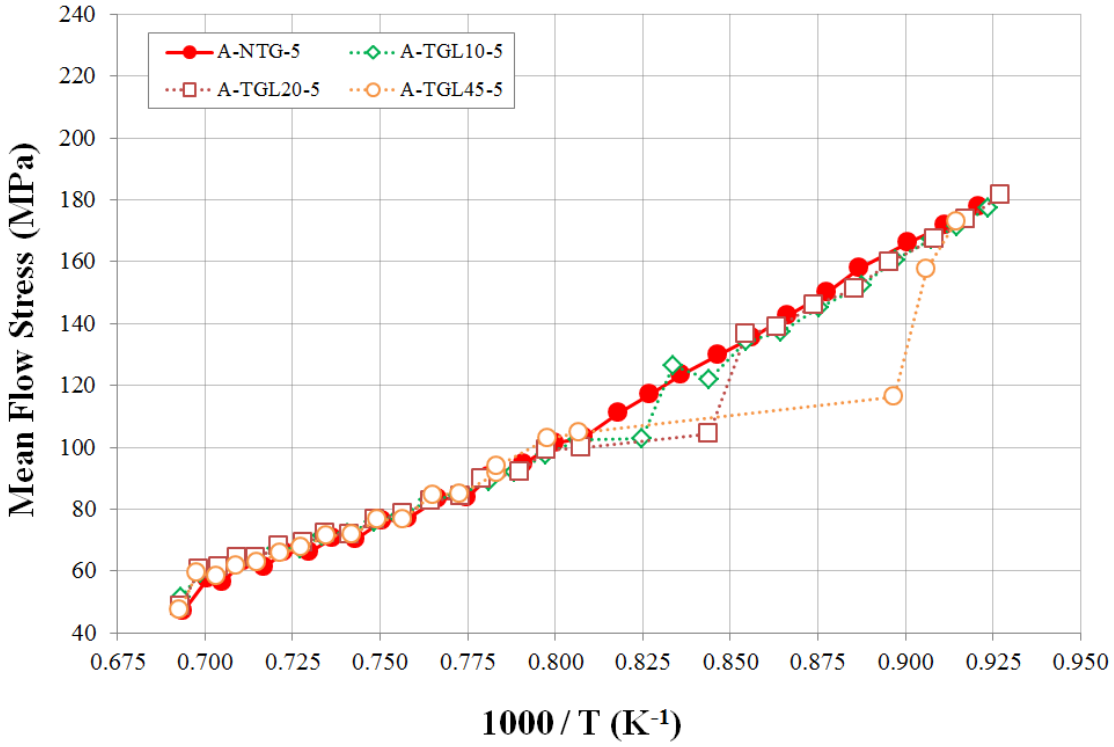

(a) Steel A.

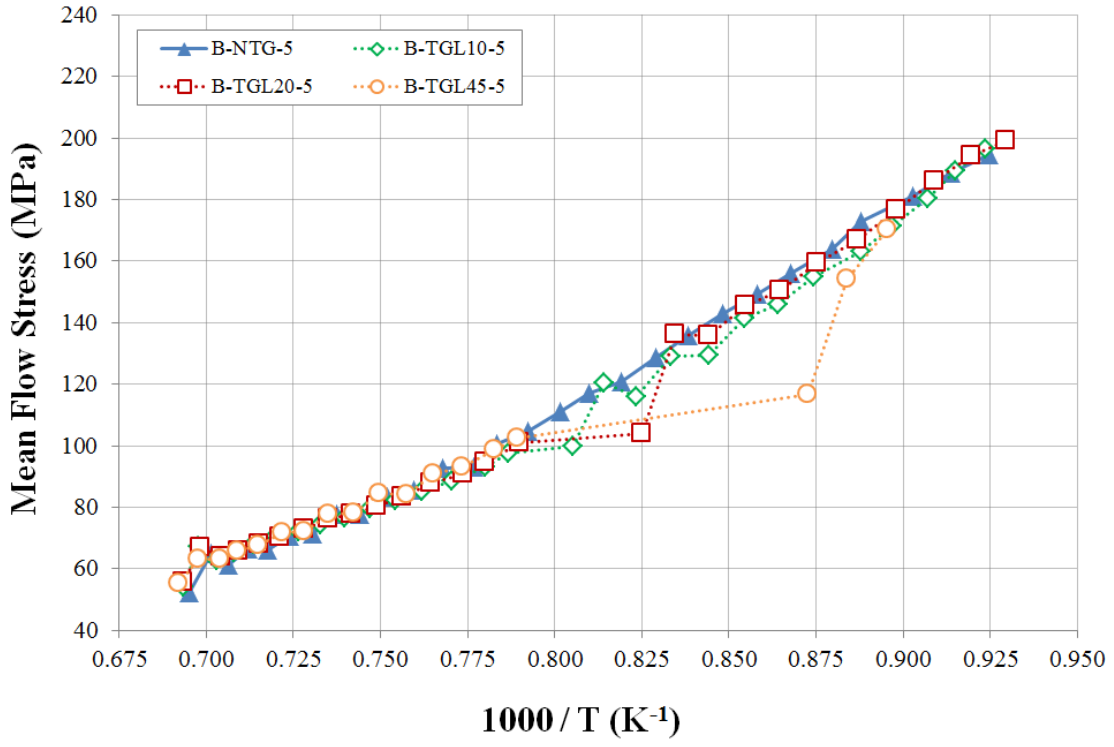

(b) Steel B.

Figure 6.10: MFS behaviour using Schedule TGL.

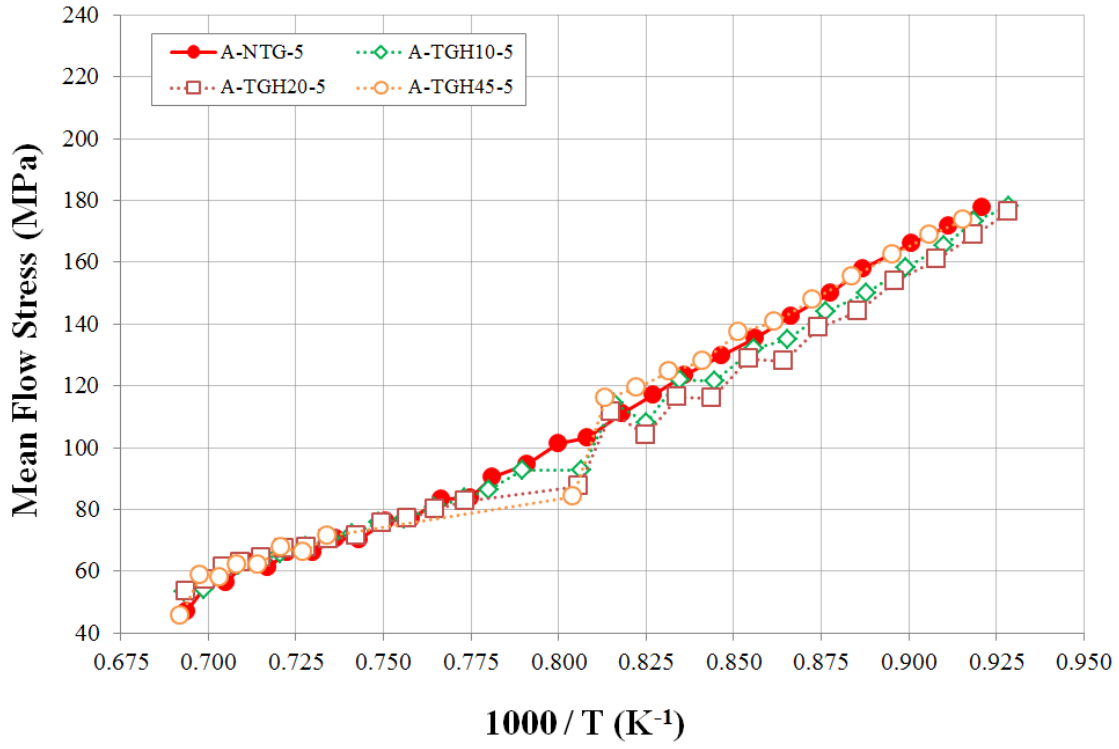

(a) Steel A.

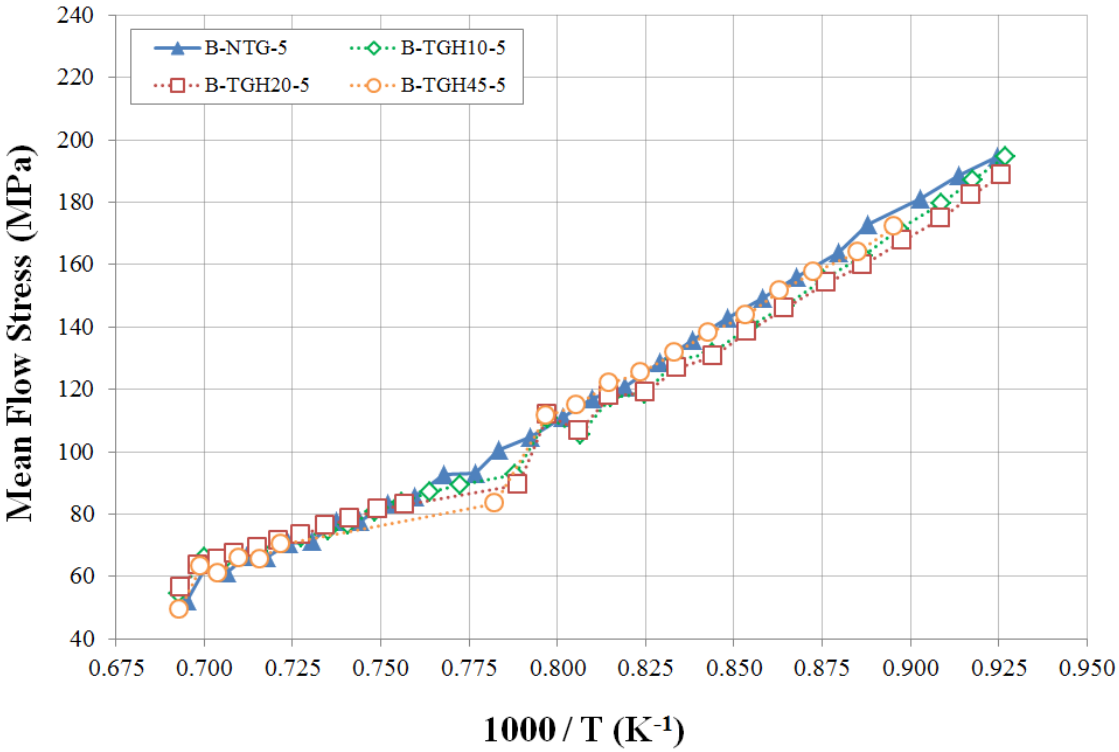

(b)) Steel B.

Figure 6.11: MFS behaviour using Schedule TGH.

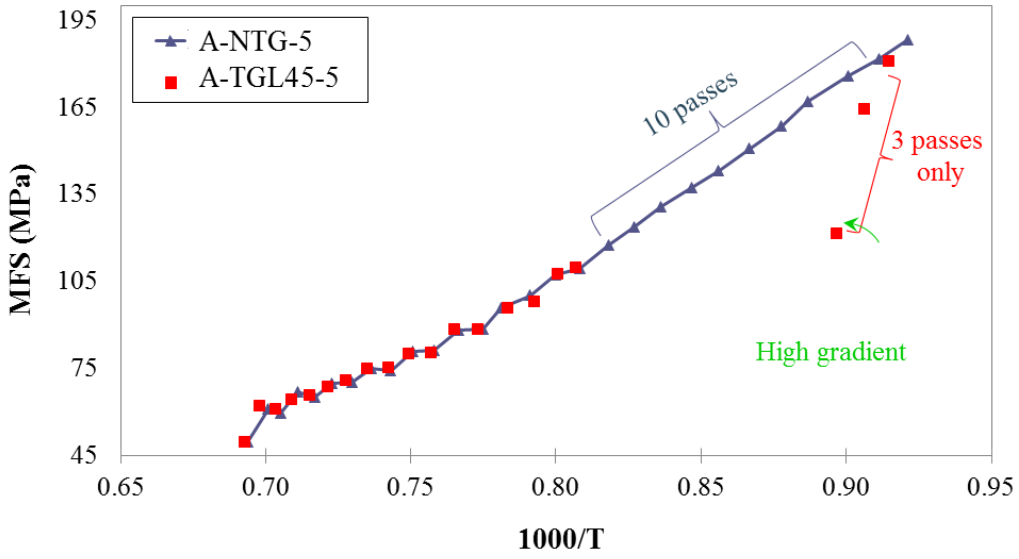

Figure 6.12: MFS behaviour using Schedule TGH.

Chapter 7

The Mean Flow Stress Prediction Model

The Misaka equation [21] is frequently used as the basis for predicting the MFS for C-Mn steels. It is essentially a simple empirical constitutive equation (i.e. it accounts for temperature, strain and strain rate) plus the effect of C. Other phenomena such as recrystallization and strain induced precipitation must be considered to acquire a model which can predict MFS for HSLA steels.

In this work, sub-models were selected carefully to take into account the effect of alloying elements such as Nb, Mo and Ti. These sub-models were incorporated in the general modified Misaka model for better prediction. Misaka expressed MFS as function of carbon content, strain, strain rate and temperature as follows:

$$MFS_{Misaka} = exp\left(A + \frac{B}{T}\right)\varepsilon^{0.21}\dot{\varepsilon}^{0.13}$$
$$A = 0.126 - 1.75\,[C] + 0.594\,[C]^2 \qquad \text{(Eq. 7.1)}$$
$$\mathrm{B} = 2851 + 2968\,[\mathrm{C}] - 1120\,[\mathrm{C}]^2$$

7.1 MFS Model for High Temperatures (Full Recrystallization)

The strain and strain rate exponents in Misaka equation were originally derived using mechanical testing and for C-Mn steels assuming full recrystallization between passes, hence this equation is applicable to high temperature roughing. However, modifications must be done to consider the effect of solid solution strengthening of other alloying elements and the mill type. These modifications are usually incorporated in the exponential term, γ, or using a multiplying factor, f, which allows us to use Misaka to model HSLA steels.

Table 7.1: Common modifications to Misaka equation.

Modification	Equation	
Multiplying factor	$\mathrm{MFS}^{*}_{\mathrm{Misaka}} = f.\ \mathrm{MFS}_{\mathrm{Misaka}}$	(Eq. 7.2)
Exponential term	$MFS = exp\left(\frac{\gamma}{T}\right)\varepsilon^{0.21}\dot{\varepsilon}^{0.13}$	(Eq. 7.3)

In this work, the approach of modifying the exponential term by eliminating the constant A and replacing B with γ, is used because it gives a better fit. The values of γ, are derived from the best fit of the high temperature side of the deformation schedule. Figures 7.1 (a and b) show the best fit for these MFS values based on the modified form of the Misaka equation.

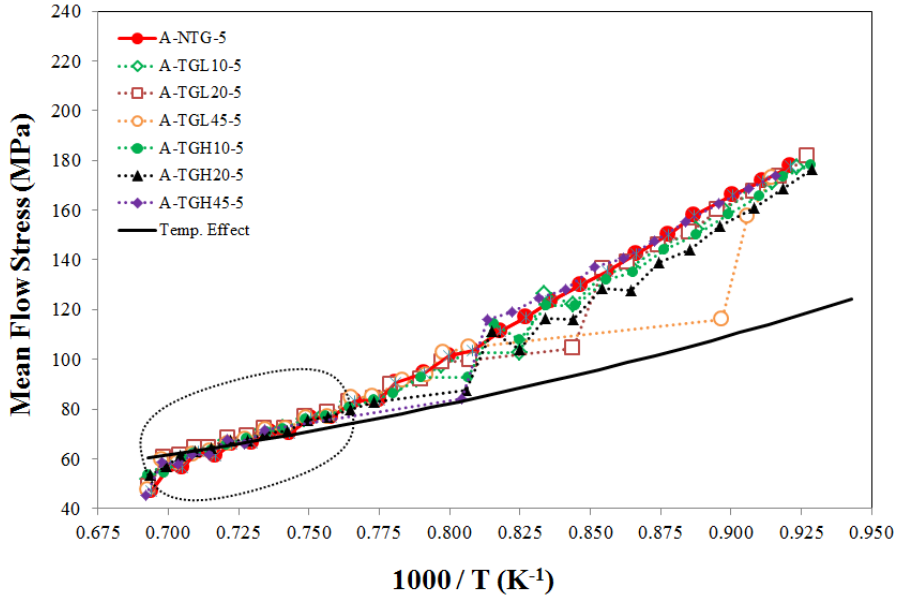

(a) γ = 2840 for Steel A

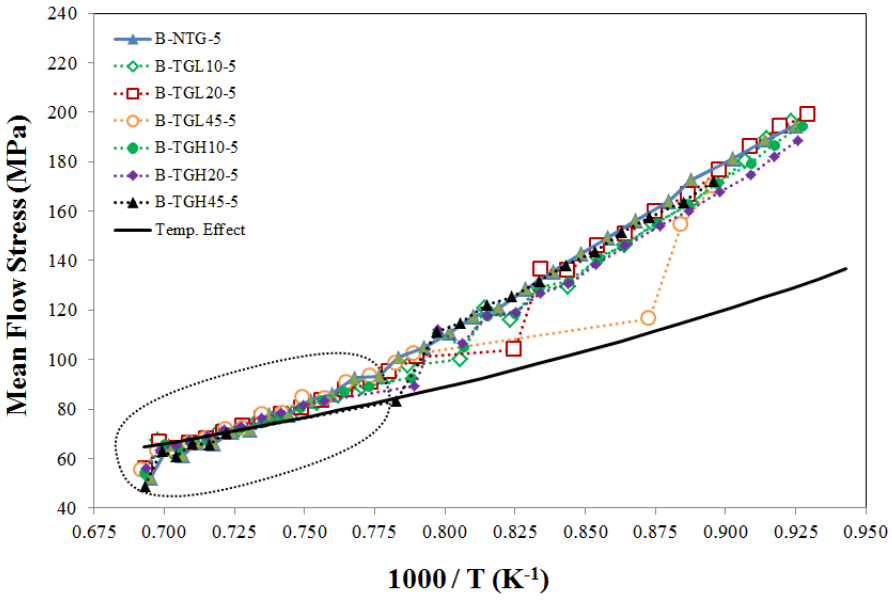

(b) γ = 2920 for Steel B

Figure 7.1: The derivation of parameter γ in the modified Misaka equation. Full softening is assumed if MFS value falls on the temperature line.

In the literature, γ is expressed as function of different alloying elements or just carbon as in the original Misaka equation. Table 7.1 shows a comparison between γ values found in this study and as reported by other workers for both steels. The value of γ is believed to be very sensitive to the mill type; γ values derived from experimental work are lower than those derived using mill data.

Table 7.2: Different values γ derived in the present study and in previous works

Author	Mill	Steel A	Steel B
Present work	Hot Torsion	2840	2920
Misaka [21]	Mechanical Testing	2994	3008
Siciliano [120]	HSM	3220	3332
Bruna [121]	HSM	3355	3402

7.2 MFS Model for Low Temperatures

During a particular deformation, the summation of retained strains caused by partial recrystallization of previous deformations with the applied strain of the current pass would determine which softening mechanism will take place. As mentioned earlier, static recrystallization (SRX) would be the only mechanism if the total strain is below the critical strain for dynamic recrystallization (DRX). Otherwise, DRX and meta-dynamic recrystallization (MDRX) will take place. Additionally, the formation of precipitates stops recrystallization between the passes and therefore alters the whole MFS behavior. The models present in the literature that describe these phenomena are function of the following:

1. Austenite grain size.
2. The amounts of Nb, Ti, C and N available in solution.
3. Deformation schedule (accumulated strain, strain rate and temperature).

7.2.1 Calculation of the Equilibrium Amounts of Nb and C.

In this work, it is assumed that Ti precipitates as the nitride at the reheating temperature, i.e. 1200°C. The equilibrium amounts of Nb and C in solid solution in wt.% can be calculated using the solubility product of NbC_{eq} [122].

$$Log(K_s) = Log\left([Nb].\left[C_{eq}\right]\right) = 2.26 - \ (6770/T) \quad \text{(Eq. 7.3)}$$

$$\left[C_{eq}\right] = [C + (12/14)N] \quad \text{(Eq. 7.4)}$$

For a given temperature, T, the equilibrium amount of Nb and C present in solid solution as well as the amount of Nb precipitated, Nb^P, as carbonitrides can calculated using the following equations [123]:

$$Nb^P{}_{equlib} = \frac{\{(A_C Nb/A_{Nb}) + C_{eq}\} - \left\{\left((A_C Nb/A_{Nb}) + C_{eq}\right)^2 - \left((4A_C/A_{Nb})(C_{eq}Nb - K_s)\right)\right\}^{1/2}}{2A_C/A_{Nb}} \quad \text{(Eq. 7.5)}$$

$$[Nb]_{equlib} = Nb - \ Nb^P \quad \text{(Eq. 7.6)}$$

$$\left[C_{eq}\right]_{equlib} = \ K_s/[Nb] \quad \text{(Eq. 7.7)}$$

Where A_C (12.01), and A_{Nb} (92.91) are the atomic weights of carbon and niobium, respectively; [Nb] and $[C_{eq}]$ are the wt.% of niobium and carbon (nitrogen ≈ 0 since Ti is assumed to precipitate as TiN) in solution and K_S is the solubility product.

7.2.2 Calculation of Statically Recrystallized Fraction during Hot Rolling

The static recrystallization kinetics equation used here has been established for isothermal conditions, whereas the temperature decreases continuously during hot rolling. Thus, the principles of the additivity rule [124] were applied for these equations to be used in continuous cooling conditions, as follows. The cooling curve is divided into large number of isothermal reaction intervals, Δt, and the fractional softening is calculated by following the below steps:

1. At a deformation temperature T_j, X_j is calculated for the first interval Δt at T_j temperature.
2. For the second interval at temperature T_{j+1}, ($T_{j+1} = T_j - \Delta t.v$), determine the "equivalent time", t_{eq}, required to reach the recrystallized fraction value of the

last pass or X_j during isothermal holding at temperature T_{j+1}, which can be calculated using the Avrami equation as follows:

$$t_{eq} = \left(t_{0.5\ at\ T_{j+1}}\right)\left\{\left(\frac{-1}{0.693}\right)\ln[1 - X_{j\ at\ T_j}]\right\}^{1/n_{j+1}} \quad \text{(Eq. 7.8)}$$

3. The real recrystallized fraction value for the second interval of temperature T_{j+1} can be computed with the following equation:

$$X_{j+1}(\Delta t) = X_{j+1}\left(\Delta t + t_{eq}\right) - X_{j+1}(t_{eq}) \quad \text{(Eq. 7.9)}$$

4. The accumulated recrystallized fraction value is calculated by adding the recrystallized fraction value for each interval.

$$X_{acc} = X_j\,(\Delta t) + X_{j+1}(\Delta t) + \cdots \quad \text{(Eq. 7.10)}$$

5. The accumulated recrystallized fraction value at the end T_{j+1} is used to calculated the "equivalent time" for the next interval by following steps 2 through 4.
6. During the whole interpass time, the total recrystallized fraction value is calculated by:

$$X_{total} = X_j\,(\Delta t) + X_{j+1}(\Delta t) + \cdots + X_{j+n}(\Delta t) \quad \text{(Eq. 7.11)}$$

7. For the next pass, X_{total} is calculated by following step 1 through 6.

7.2.3 Calculation of Precipitated Fraction during Hot Rolling

The amounts of Nb, C, and Nb^P during hot rolling are different from those calculated using equilibrium conditions and, therefore, a different approach is used as follows:

The precipitated weight fraction for time t, at a constant temperature is calculated as:

$$[Nb^P{}_{at\ T=constant}] = \left[Nb^P{}_{equlib}\right].X_{p\ at\ T=constant} \quad \text{(Eq. 7.12)}$$

Where Xp is the precipitated fraction for time t at constant temperature, which can be modeled by an Avrami type equation[124].

$$X_p = 1 - exp\left(\ln(0.95)\left(\frac{t}{t_{0.05p}}\right)^{n_p}\right) \quad \text{(Eq. 7.13)}$$

Where $t_{0.05p}$ is the start time for strain induced precipitation, n_p is Avram exponent taken as 0.6 from reference [125]

The additivity rule [124] is also applied for the calculation of the precipitated volume fraction under continuous cooling conditions using the following equation:

$$X_{p_{j+1}}(\Delta t) = X_{p_{j+1}}(\Delta t + t_{eq}) - X_{p_{j+1}}(t_{eq}) \qquad \text{(Eq. 7.14)}$$

The equivalent time in the case of the occurrence of precipitation is defined as the time required to reach the precipitated fraction X_{p_j} at temperature T_j of the previous deformation, during the isothermal annealing at T_{j+1}.

$$t_{eq} = t_{0.05p\ at\ T_{j+1}} \left(\frac{1}{\ln(0.95)} ln\left(1 - X_{p\ at\ T_j}\right) \right)^{1/n_p} \qquad \text{(Eq. 7.15)}$$

The total precipitated weight fraction at the end of the interpass time is calculated as follows:

$$X_{p,\ total} = X_{p,\ j}(\Delta t) + X_{p,\ j+1}(\Delta t) + \cdots + X_{p,\ j+n}(\Delta t) \qquad \text{(Eq. 7.16)}$$

In multipass hot deformation, the time required for the onset of precipitation can be determined by applying the additivity rule. This approach involves dividing the continuous cooling curve into multiple isothermal segments, and then calculating the time required to start precipitation for each isothermal segment as shown in Figure 7.2. Then, strain induced precipitation is considered to occur and recrystallization is assumed to have stopped once the summation of t_{ip}/t_{ps} reaches unity as stated by the following relation:

$$\frac{t_{ip_1}}{t_{ps_1}} + \frac{t_{ip_2}}{t_{ps_2}} + \frac{t_{ip_3}}{t_{ps_3}} + .. + \frac{t_{ip_n}}{t_{ps_n}} = 1 \qquad \text{(Eq. 7.17)}$$

Thus, the precipitation start time for a particular hot deformation schedule corresponds to the summation of the time required to start precipitation for each isothermal segment at a temperature T, which fulfills the previous condition.

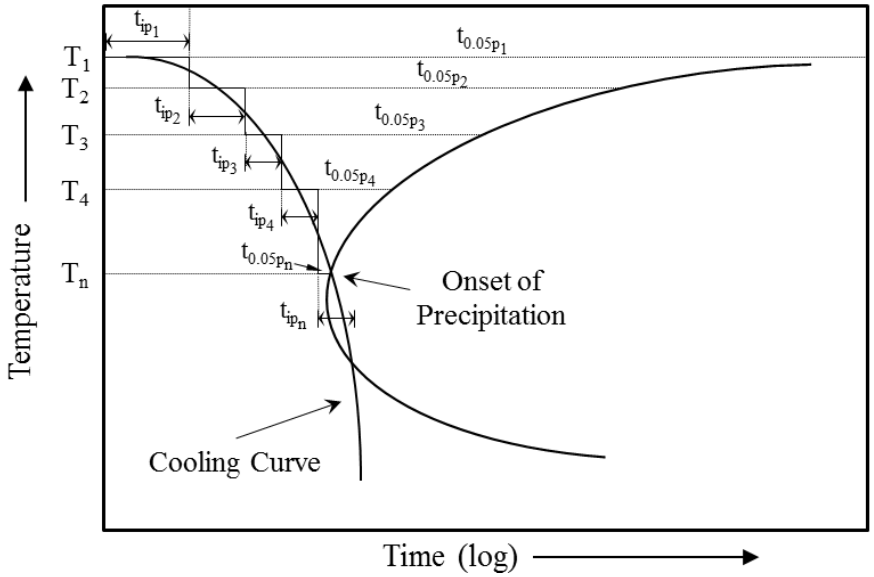

Figure 7.2: An illustration of the concept of additivity rule.

7.2.4 Strain accumulation during Hot Rolling

In multipass hot deformation, a mixed microstructure is produced when the interpass time is not long enough for full recrystallization. Therefore, the accumulated strain and the average grain size must be taken into account for the proper calculation of recrystallization and strain-induced precipitation. Using the "uniform softening method", which assumes a single average microstructure, the effective strain can be calculated by adding the "retained" strain to the pass strain using the following equation:

$$\varepsilon_{acc_j} = \varepsilon_j + k\left(1 - X_{j-1}\right)\varepsilon_{j-1} \qquad \text{(Eq. 7.18)}$$

where ε_j is the pass strain, X_{j-1} and ε_{j-1} are the recrystallized fraction between pass j and j-1. The constant k is related to the rate of recovery ranging from 0.5 (high recovery) to 1 (low recovery) for short and long interpass times, respectively [20]. A value of 1 was taken in this work.

7.3 The Structure of the General Model

The structure of the general model is shown in Figure 7.3. It requires the following input data:

1. Austenite initial grain size (assumed to be 100μm) [20].
2. [Nb] and [C_{eq}] weight percent in solution.
3. The reheating temperature (1200°C)
4. The chemical compositions.
5. Activation energy for deformation.
6. Deformation schedule.

For each deformation, the accumulated strain, the new initial austenite grain, the amount of [Nb] in solution, and the summation of $t_{ip}/t_{0.05ps}$ are taken as input for the next deformation.

The model is capable of predicting the following points:

1. Partial recrystallization due to solute drag.
2. Complete recrystallization followed by grain growth.
3. No recrystallization because of the occurrence of strain induced precipitation.
4. Precipitated weight fraction.
5. Temperature of no recrystallization.
6. Dynamic recrystallization.
7. Grain size is predicted for each deformation.
8. Mean flow stress.

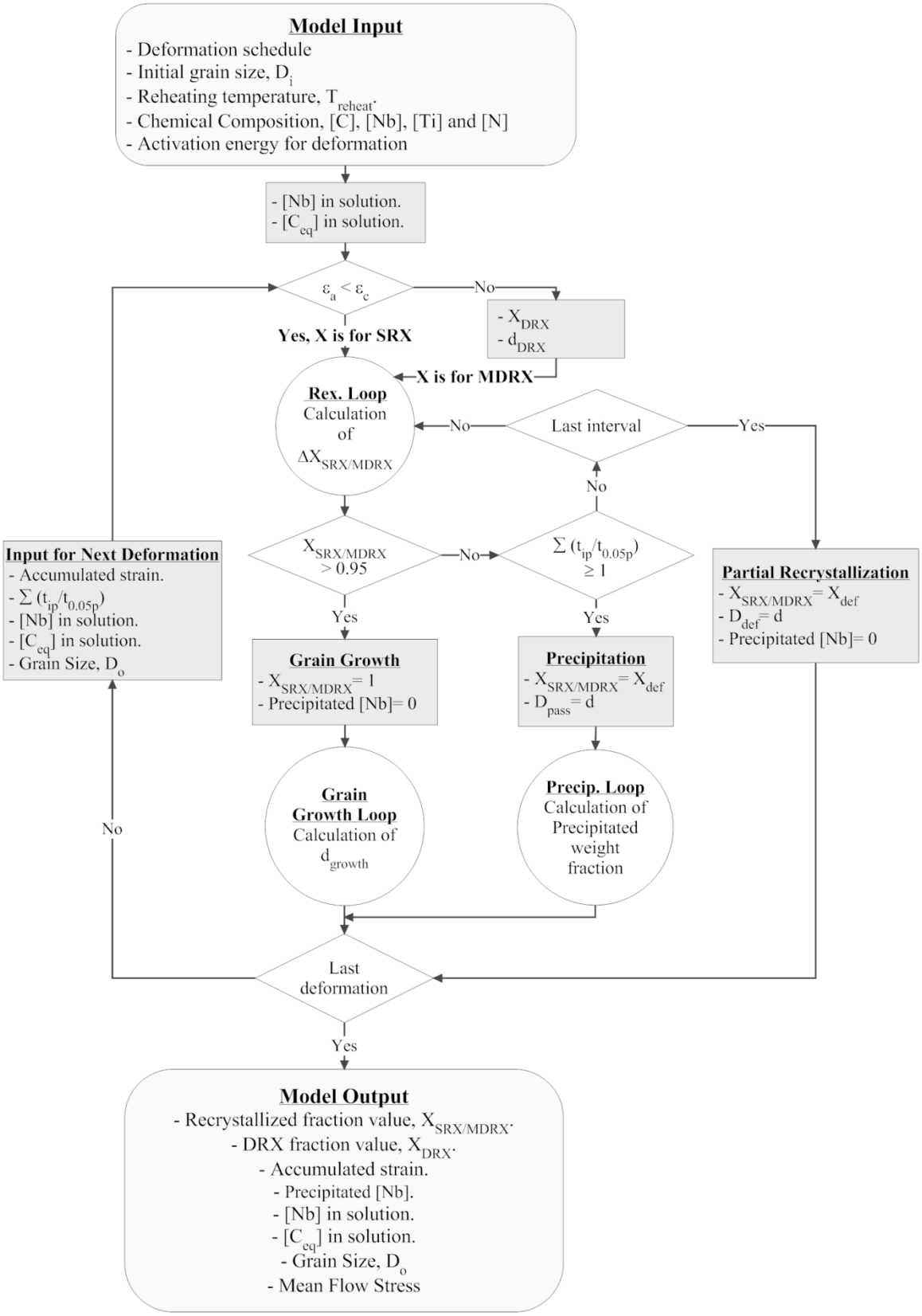

Figure 7.3: Flow chart describing the process of MFS calculation. [124]

7.3.1 A Static Recrystallization (SRX) Model

The evolution of the statically recrystallized fraction with time was described using a model developed by Fernández [80]:

$$X_{SRX} = 1 - exp[-0.693(t/t_{0.5\,SRX})^{n}] \quad \text{(Eq. 7.19)}$$

$$t_{0.5\,SRX} = 9.92 \times 10^{-11}\, d_0 \varepsilon^{-5.6 d_0^{-0.15}} \dot{\varepsilon}^{0.53} exp\left(\frac{180000}{RT}\right)\ exp\left[\left(\frac{275000}{RT} - 185\right) \times ([Nb] + 0.37[Ti])\right] \quad \text{(Eq. 7.20)}$$

This model was selected because it accounts for Nb and Ti contents present in solution, giving rise to solute drag, although in this work it is assumed that the Ti precipitates as the nitride. The effect of grain size takes into account the increase in recrystallization nucleation sites with decreasing grain size.

It is well known that the addition of Nb retards recrystallization by solute drag and pinning by strain-induced precipitates. Solute drag will slow down softening, whereas strain-induced precipitation has a much stronger influence and effectively stops recrystallization. The effect of solute drag before the onset of precipitation would influence the Avrami exponent in the below equation as reported by Medina and Quispe [126]. It was observed that the Avrami exponent depends on the temperature for microalloyed steels and it slightly decreases with decreasing the temperature. This dependence was expressed by the following equation:

$$n = 28 exp\left(\frac{-36000}{RT}\right) \quad \text{(Eq. 7.21)}$$

7.3.2 Meta-Dynamic (MDRX) & Dynamic (DRX) Recrystallization Models

The occurrence of meta-dynamic (MDRX) and dynamic recrystallization (DRX) is associated with the critical strain value. When the following relation is satisfied, then MDRX and DRX are initiated.

Accumulated strain > Critical strain (MDRX and DRX)

For the present purpose, it is useful to express the critical strain as function of peak strain since many equations can be found in the literature. The model proposed by Pereda

et al. [56] was selected in this work since it is a generalized model for different types of HSLA steels.

$$\varepsilon_p = 3.7 \times 10^{-3} \frac{\{1 + 20([Nb] + 0.02[Ti] + \Delta \times 0.035)\}}{1.78} \times d_0^{0.147} Z^{0.155} \qquad \text{(Eq. 7.22)}$$

The critical strain can be determined by assuming that $\varepsilon_c/\varepsilon_p$ for Nb steel is 0.77 [56]

The time required for the completion of 50% recrystallization was modeled for both steels using different models as follows:

Steel A
$$t_{0.5\,MDRX} = 8.4 \times 10^{-9} \dot{\varepsilon}^{-0.84} exp\left(\frac{186000}{RT}\right) \qquad \text{[62] (Eq. 7.23)}$$

Steel B
$$t_{0.5\,MDRX} = 4.42 \times 10^{-7} \dot{\varepsilon}^{-0.59} exp\left(\frac{153000}{RT}\right) \qquad \text{[62] (Eq. 7.24)}$$

The recystallized fraction due to MDRX was calculated using the Avrami equation. The Avrami exponent was assumed to be equivalent to that for SRX, and therefore it was calculated using Medina equation [126].

$$X_{MDRX} = 1 - exp[-0.693(t/t_{0.5\,MDRX})^n] \qquad \text{(Eq. 7.25)}$$

For DRX modeling, the fractional softening due to DRX was modeled using the following equation for microalloyed steels [56]:

$$\mathrm{X_{dyn}} = 1 - exp(-2.5\ (\varepsilon - \varepsilon_c)^{1.5}) \qquad \text{(Eq. 7.26)}$$

The drop in MFS associated with DRX was modeled using Siciliano approach [61]:

$$\mathrm{MFS_{Siciliano}} = \mathrm{MFS^*_{Misaka}} \times 9.8 \times \left(1 - \mathrm{X_{dyn}}\right) + 1.14\ \sigma_{ss} \mathrm{X_{dyn}} \qquad \text{(Eq. 7.27)}$$

Where 9.81 is used to convert to MPa and 1.14 is a fitting parameter required to convert flow stress to mean flow stress.

The steady stress model proposed by Roucoules et al. for Nb steels was used [60]:

$$\sigma_{ss} = 4.2 \left[\dot{\varepsilon}\ \exp\left(\frac{Q_{def}}{RT}\right)\right]^{0.09} \qquad \text{(Eq. 7.28)}$$

7.3.3 Microstructural Evolution Models

The grain sizes for full static, metadynamic and dynamic recrystallization were represented using the following equations:

$$d_{SRX} = 1.1 d_0^{0.67} \varepsilon^{-0.67}$$ **[64]** (Eq. 7.29)

$$d_{MDRX} = 1400 \times \left\{ \dot{\varepsilon}. exp\left(\frac{Q_{def}}{RT}\right)\right\}^{-0.13}$$ **[65]** (Eq. 7.30)

$$d_{DRX} = \mathbf{A}.\ Z^{-0.13}$$ **[56]** (Eq. 7.31)

where **A** = 580 and 812 for steels A and B, respectively

Once recrystallization is complete, grain growth occurs and it is a function of time, temperature and the fully SRX or MDRX grain size. The grain growth model for Nb steel given by Hodgson et al. is:

$$d^{4.5} = d^{4.5}_{Full\ SRX/MDRX} + 4.1 \times 10^{23} \times (t_{ip} - 4.32\, t_{0.5\ SRX/MDRX}) \times exp(-435000/RT)$$ (Eq. 7.32)

Where t_{ip} is the interpass time and $4.32 x t_{0.5}$ is the time for full (95%) recrystallization.

If the fractional softening is not complete, the average grain size for the subsequent deformation can be calculated by the "law of mixtures" type relation. This relation takes into account the recrystallized and unrecrystallized regions from the last pass.

$$d_{0_{i+1}} = d_{i,rex}\, X_i^{4/3} + d_{0_i}(1 - X_i)^2$$ (Eq. 7.33)

7.3.4 Strain-induced Precipitation Model

The model proposed by Dutta and Sellars [109] was used to describe the isothermal strain-induced precipitation of Nb carbonitride from supersaturated austenite.

$$t^{DS}_{0.05\ ps} = A\ [Nb]^{-1} \varepsilon^{-1} Z^{-0.5} exp\left(\frac{270000}{RT}\right) exp\left(\frac{B}{T^3\ ln(K_s^2)}\right)$$ (Eq. 7.34)

Where [Nb] is the amount of niobium in solution, Z is Zener-Hollomon parameter and Ks is the supersaturation ratio which describes the driving force for precipitation.

The Zener-Hollmon parameter [127] is given by:

$$Z = \dot{\varepsilon} \exp(\mathrm{Q_d}/RT) \quad \text{(Eq. 7.35)}$$

The supersaturation (Ks) was determined using the ratio of the solubility products, derived by Irvine el al. [110], of the reheat to the pass temperatures [20].

$$K_s = \frac{10^{-6770/T_{RH}+2.26}}{10^{-6770/T_{Pass}+2.26}} \quad \text{(Eq. 7.36)}$$

Recent studies by Pereda et al [124] revealed that the A and B parameters in Dutta-Sellars model are dependent on solubility products rather than being constant values as determined by the original model ($A = 3 \times 10^{-6}, B = 2.5 \times 10^{10}$).

$$A = 9.42 \times 10^{-7} exp\left(-372.\left([Nb].[C + (12/14).N)\right)\right) \quad \text{(Eq. 7.37)}$$

$$B = 1.59 \times 10^{9} exp\left(-459.\left([Nb].[C + (12/14).N)\right)\right) \quad \text{(Eq. 7.38)}$$

7.3.5 Activation Energy for Hot Deformation

Many authors reported the activation energy for hot deformation as one value which mainly depends on chemical composition regardless of test variables [1, 20, 23, 60, 119]. Cho et al. [62] derived an equation to estimate the activation energy as a function of microalloying elements.

Radovi and Drobnjak [128] studied the effect of interpass time on the hot deformation activation energy for Nb/Ti steels obtained from anisothermal multipass flow curves using hot torsion test. It was observed that the activation energy at high temperatures, Q_{def}^{H}, i.e. above T_{nr}, is little affected by the interpass time and cooling rate and its value is close to austenite self-diffusion. However, the Q_{def}^{L} below T_{nr} becomes sensitive to interpass time and is considerably higher because, according to the authors, recrystallization is retarded and probably precipitation strengthening is introduced.

It was concluded that the effect of interpass time on Q_{def}^{L} can be categorized in three groups as follows:

1. Interpass time below 10 seconds: Q_{def}^{L} *increases* with increasing interpass time.
2. Interpass time from 10 to 50 seconds: Q_{def}^{L} *slightly* increases with increasing interpass time.
3. Interpass time above 50 seconds: Q_{def}^{L} *decreases* with increasing interpass time.

For a Nb/Ti steel containing 0.074C, 0.035 Nb, 1.15Mn, 0.21Si, 0.024P. 0.014S. 0.068A1, 0.009N, 0.016Ti, the aforementioned 'double' Q_{def} behaviour was studied using different average schedules of different interpass times and cooling rates; the strain and strain rate were kept constant. Double Q_{def} behaviour was observed in all deformation schedules except for the case of high cooling rate of 14.1°C/sec and a very short interpass time of 2.7 sec, refer to Table 7.3.

Table 7.3: Different activation energies for deformation obtained using different interpass times and cooling rates [128].

Schedule		$Q_{def}^{H}(kJ/mol)$	$Q_{def}^{L}(kJ/mol)$
Interpass time (sec)	**Cooling rate (°C/sec)**		
2.7	14.2	386	386
5	5	314	395
10	2.5	295	365
30	0.86	334	383

In this work, the approach of the presence of double Q_{def} as reported by Radovi and Drobnjak [128] was used, even though the steel compositions are different. However, modeling the MFS using these values led to better results. Since the double Q_{def} was assumed to be related to the T_{nr} temperature, all the passes prior to the occurrence of strain induced precipitation were modeled by a Q_{def}^{H} value while Q_{def}^{L} was used after the onset of precipitation. It should be noted that the T_{nr} temperature was assumed to be the temperature of the first pass after the summation of $t_{ip}/t_{0.05ps}$ reaches unity. At this

particular pass, strain induced precipitation commences and the transition form Q_{def}^{H} to Q_{def}^{L} takes place.

In this work the activation energies for the higher and lower temperatures for both steels and using NTG-30 schedule were selected as 334 and 383, respectively [128]. These values were obtained using similar test variables, i.e. an interpass time of 30s and a cooling rate of 0.86°C/s. While for NTG-5 schedule, it was found that data of 10s interpass time and 2.5°C/s give a better MFS prediction. Since the data on the effect of time gap on the activation energy are lacking in the literature, the same values of NTG-5 schedule were used.

7.4 Spreadsheet for the Prediction of MFS

All models were incorporated in Excel file which predicts the MFS for each deformation step during the rolling schedule. The output data, listed in the following tables, includes the critical strain required to initiate DRX, the fractional softening of DRX (X_{DRX}), MDRX and SRX (X; whenever there is DRX, X= MDRX), grain size (d), amount of Nb in solution ($[Nb]_{soln}$) and in the carbide (Nb in C). When the wt % of strain induced precipitation is 5% or greater, X = 0; otherwise X is only reduced by solute drag. The MFS vs. 1000/T were generated and compared with the experimental data for each deformation schedule for both steels. Due to similarities between the two steels, only one steel (Steel B) will be discussed in the following pages, while all tabulated data and figures for microstructural and MFS prediction of Steel A are attached in the appendix.

7.4.1 Microstructural and MFS Predictions for Case I: No Time Gap

A B-NTG-5 Schedule

The model is in very good agreement with the experimental data as shown in Table 7.4 and Figure 7.4. According to the results, deformation at high temperature with short interpass times of 5 seconds does not always lead to full static recrystallization. Instead, there is a predicted fluctuation of X as deformation proceeds from pass 1 to 12. It can be observed that the predicted accumulated strains for all even passes are higher than the odd ones. The higher strain accumulation speeds up the static recrystallization kinetics after these even passes and thus higher SRX were achievable during the interpass time. Therefore, the lower retained strain, attained during the interpass time of the even passes, was added to the applied strain for the odd passes. This resulted in lower accumulated strains for the odd passes compared to the even passes and therefore, lower SRX values were obtained. This alternating behaviour continued as the speed of SRX kinetics reduced as a result of decreasing temperature, solute drag and precipitation until strain induced precipitation commenced. More than 5wt% of precipitates were formed during the interpass time of pass 12. This causes recrystallization to stop completely (X = 0) in the interpass time after pass 13 (1015°C), and therefore, the pass strains are accumulated. Furthermore, more and more Nb is taken out of solution to form NbC, which hypothetically should make dynamic recrystallization easier by reducing the amount of *dynamic* precipitation [108]. The model predicts dynamic recrystallization during all the passes after pass number 15, greatly influencing most of the passes below the T_{nr}. The occurrence of DRX is also linked to the use of lower deformation activation energy for this particular schedule, and therefore the strain required for DRX initiation, i.e. critical strain, was attainable. For the last 10 passes, the MFS was a function of the steady state flow stress only, according to Eq. 7.27, since the fractional softening associated with DRX was almost equal to 1. Furthermore, the model does not explicitly take the effect of precipitation strengthening on MFS into account, yet the predicted MFS values matches the experimental data. The reason for the insignificant role of precipitation strengthening is not clear at present. However, it might be related to precipitate pinning force which is mainly affected by density, distribution, particle radius and volume fraction of Nb(C,N)

[129]. In this case, most of the Nb precipitated as carbides according to the model and therefore, the density, distribution and/or particle radius are possible factors. Further microstructural studies are required to determine the reason for absence of significant precipitation strengthening in this schedule.

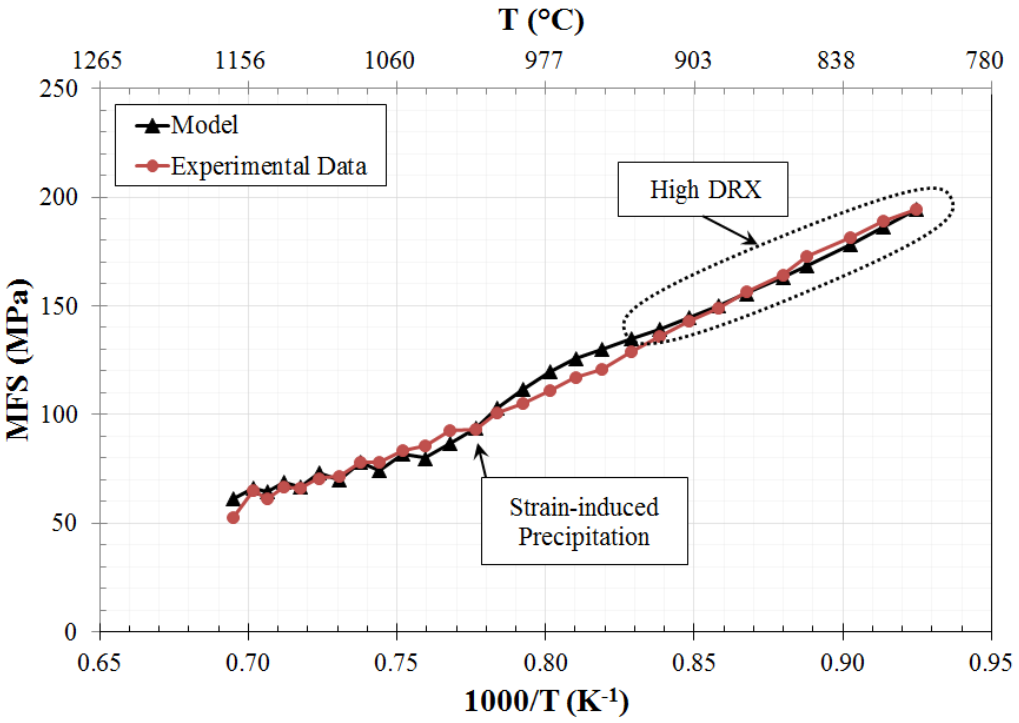

Figure 7.4: MFS graph for B-NTG-5

Table 7.4: Microstructural and MFS predictions for B-NTG-5.

Pass No.	T_{def} (°C)	t_{ip}	ε_a	ε_c	X_{DRX}	$[Nb]_{soln}$	Nb in C	X	d	1000/T	MFS (Model)	MFS (Torsion)
1	1166	5	0.20	0.38	0.00	0.085	0.000	0.69	52.8	0.695	61.4	52.4
2	1153	5	0.26	0.36	0.00	0.085	0.000	0.96	38.5	0.701	66.2	65.1
3	1142	5	0.21	0.35	0.00	0.085	0.000	0.65	25.1	0.706	64.2	61.3
4	1131	5	0.27	0.34	0.00	0.085	0.000	0.93	20.8	0.712	68.9	66.5
5	1121	5	0.22	0.34	0.00	0.085	0.000	0.53	14.6	0.718	66.9	66.1
6	1108	5	0.30	0.33	0.00	0.085	0.000	0.92	13.2	0.724	72.9	70.7
7	1096	5	0.23	0.34	0.00	0.085	0.000	0.37	9.7	0.730	69.8	71.5
8	1083	5	0.34	0.33	0.00	0.084	0.001	0.87	8.7	0.738	77.7	77.9
9	1071	5	0.25	0.34	0.00	0.084	0.001	0.33	6.7	0.744	74.0	77.7
10	1057	5	0.36	0.34	0.01	0.083	0.002	0.77	5.8	0.752	81.9	83.5
11	1044	5	0.28	0.34	0.00	0.082	0.004	0.36	4.5	0.760	79.8	85.6
12	1029	5	0.38	0.34	0.02	0.081	0.017	0.27	3.4	0.768	86.4	92.6
13	**1015**	5	0.48	0.98	0.00	0.068	0.031	**0.00**	3.4	0.777	93.7	93.3
14	1003	5	0.68	0.91	0.00	0.054	0.044	0.00	3.4	0.783	102.8	100.8
15	989	5	0.88	0.84	0.02	0.041	0.055	0.00	3.4	0.792	111.5	104.8
16	975	5	1.08	0.79	0.33	0.030	0.063	0.00	7.7	0.802	119.7	111.0
17	962	5	1.28	0.85	0.51	0.022	0.069	0.00	7.4	0.810	125.5	117.2
18	948	5	1.48	0.82	0.74	0.016	0.073	0.00	7.0	0.819	130.1	120.9
19	933	5	1.68	0.81	0.87	0.012	0.076	0.00	6.6	0.829	134.8	128.6
20	920	5	1.88	0.82	0.94	0.009	0.078	0.00	6.3	0.838	139.4	135.6
21	906	5	2.08	0.84	0.97	0.007	0.079	0.00	5.9	0.848	144.6	142.8
22	892	5	2.28	0.86	0.99	0.005	0.080	0.00	5.6	0.858	149.9	149.1
23	879	5	2.48	0.90	0.99	0.004	0.081	0.00	5.3	0.868	155.6	156.2
24	864	5	2.68	0.95	1.00	0.003	0.082	0.00	5.0	0.880	163.0	164.0
25	853	5	2.88	0.98	1.00	0.003	0.082	0.00	4.8	0.888	168.2	172.7
26	835	5	3.08	1.07	1.00	0.002	0.083	0.00	4.4	0.903	178.2	181.3
27	821	5	3.28	1.13	1.00	0.002	0.083	0.00	4.1	0.914	186.0	188.7
28	808	-	3.48	1.20	1.00	0.002	-	-	-	0.925	194.1	194.5

B B-NTG-30 Schedule

For the case of 30 second interpass times, the model precisely predicts the MFS values for the first 3 passes where full static recrystallization is achievable. Once precipitates of 0.004wt% formed during the interpass time of pass 3, the model underestimates the MFS values for most passes, possibly due to the effect of precipitation strengthening as well as strain accumulation. The latter may occur because of the effect of interaction between precipitation and recrystallization. At 1063°C (pass 5), strain induced precipitation commenced and fractional softening for SRX is assumed to be zero. The higher predicted T_{nr} temperature in this schedule compared to NTG-5 schedule is due to the higher influence of precipitation with increasing the interpass time. In this schedule, DRX was prevented because the accumulated strain did not exceed the critical strain. This is directly related to use of higher activation energy compared to NTG-5 schedule. Unlike NTG-5 schedule, precipitation strengthening appears to be responsible for the deficiency in the model with a maximum difference of around 19 MPa.

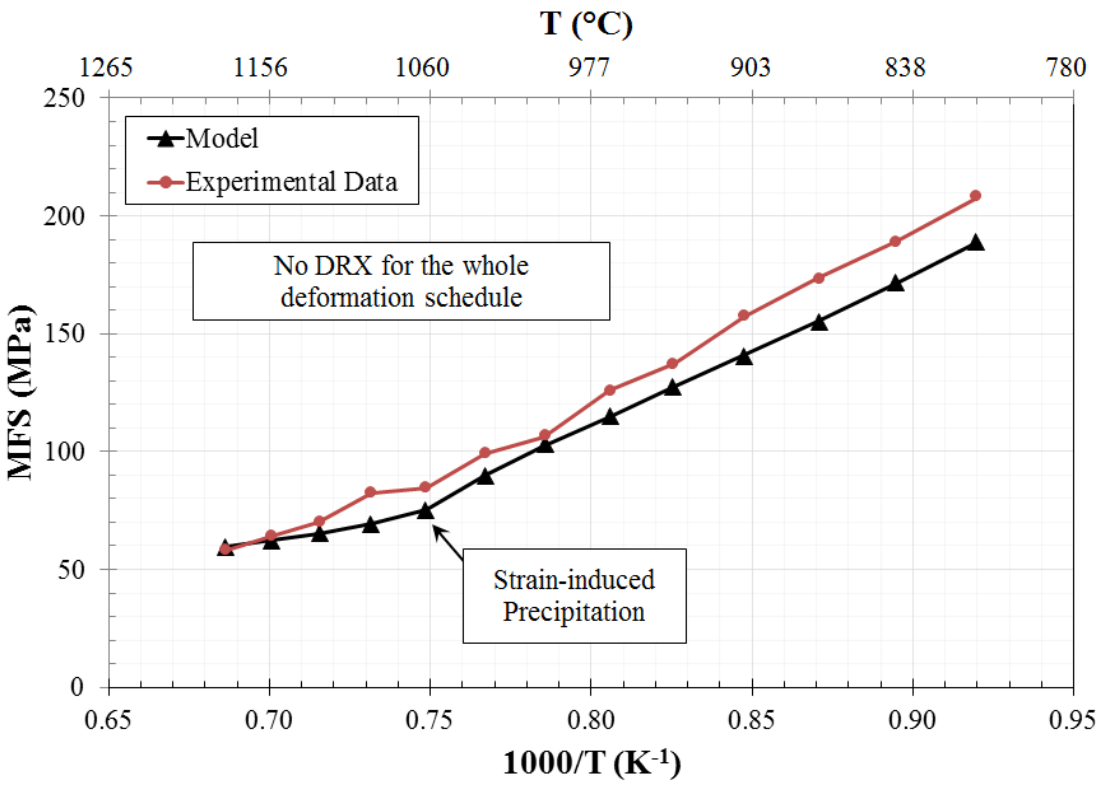

Figure 7.5: MFS graph for B-NTG-30

Table 7.5: Microstructural and MFS predictions for B-NTG-30.

Pass No.	T_{def} (°C)	t_{ip}	ε_a	ε_c	X_{DRX}	$[Nb]_{soln}$	Nb in C	X	d	1000/T	MFS (Model)	MFS (Torsion)
1	1183	30	0.20	0.72	0.00	0.085	0.000	1.00	122.3	0.687	59.9	58.0
2	1155	30	0.20	0.81	0.00	0.085	0.000	1.00	95.8	0.700	62.4	64.1
3	1125	30	0.20	0.86	0.00	0.085	0.000	0.92	61.8	0.715	65.1	70.0
4	1094	30	0.22	0.89	0.00	0.084	0.004	0.77	37.4	0.732	69.5	82.2
5	**1063**	30	0.25	0.89	0.00	0.081	0.028	0.00	37.4	0.749	75.3	84.4
6	1031	30	0.45	1.64	0.00	0.056	0.053	0.00	37.4	0.767	89.9	99.0
7	1000	30	0.65	1.44	0.00	0.032	0.068	0.00	37.4	0.785	102.4	106.1
8	968	30	0.85	1.35	0.00	0.016	0.076	0.00	37.4	0.806	115.0	126.0
9	938	30	1.05	1.37	0.00	0.008	0.080	0.00	37.4	0.826	127.5	137.4
10	906	30	1.25	1.50	0.00	0.004	0.082	0.00	37.4	0.848	141.1	157.5
11	876	30	1.45	1.70	0.00	0.002	0.083	0.00	37.4	0.870	155.4	173.6
12	845	30	1.65	1.98	0.00	0.002	0.084	0.00	37.4	0.895	171.4	189.2
13	814	-	1.85	2.35	0.00	0.001	-	-	-	0.920	188.9	207.7

7.4.2 Microstructural and MFS Predictions for Case II: Time Gap

The model generally provides good predictions of MFS, however the first few passes of finishing did not precisely fit the experimental data for the following possible reasons:

1. The sharp rise in MFS value for the second pass of finishing is believed to be related to precipitation strengthening, for two main reasons. Firstly, the sharp rise tends to be greater when the time gap is increased from 10 to 20s or 20 to 45s. The greater time gap increases the chance for precipitation strengthening, because the temperature of the subsequent pass is decreased, thereby increasing the driving force for precipitation. Therefore, strain induced precipitation occurs in first finishing pass which gives the sharp rise in MFS of the following passes. Secondly, the rise in MFS in TGL schedules, where finishing was well below the T_{nr} temperature, is even sharper since more precipitates are formed.

2. For all time gap schedules, the values for activation energy of NTG-5 schedule were used since there are no available data on the effect of time gap on the activation energy. If the time gap, for example, decreased the activation energy for deformation, the critical strain would be easier to achieve and therefore dynamic recrystallization could take place during the first pass. Additionally, if the occurrence of strain induced precipitation influences the activation energy of hot deformation, this would lead to different MFS behavior for the subsequent finishing passes. Further studies are required to investigate all parameters including the time gap on the activation energy for deformation.

3. It was assumed the occurrence of 5% precipitation would stop recrystallization (X = 0). Therefore, the model does not take into account the interaction between recrystallization and precipitation. This affected the prediction of MFS value for the first finishing pass in TGL schedules that were designed so the last roughing pass deformed at a temperature close to T_{nr}. In these cases, it seems that recrystallization resumes during the time gap, leading to a lower measured value, according to torsion data, than predicted by the model. The assumption that 5% precipitation stops SRX appears to be valid when the time gap or interpass time that follows the occurrence of 5% strain induced precipitation is relatively short.

Otherwise, 5% precipitation would not be able to retard recrystallization during longer interpass times or time gaps.

A B-TGH10-5

As shown in Figure 7.6 and Table 7.6, the behavior of MFS up to pass R13 was very similar to NTG-5 schedule since the deformation variables are identical. The amount of Nb in carbide reached 0.011wt%, i.e. more than 5% of precipitation, during the interpass time of pass R12. Therefore, pass R13 (1022°C) is assumed to be where recrystallization stops. After this pass, a time gap of 10 seconds was incorporated. The model overestimates the MFS values for several passes after the time gap by a maximum error value of 13 MPa probably as a result of an overestimation in the value of the accumulated strain. Therefore, all fluctuations after the time gap that were initially assumed to be related to SRX were not predicted. Probably, the small amount of precipitates formed before the time gap was able to stop SRX in the NTG-5 schedule. However, when 10 seconds was used, this perhaps allowed recrystallization to resume along with precipitation. As DRX starts to take place after pass F03, the model slowly converges with torsion data.

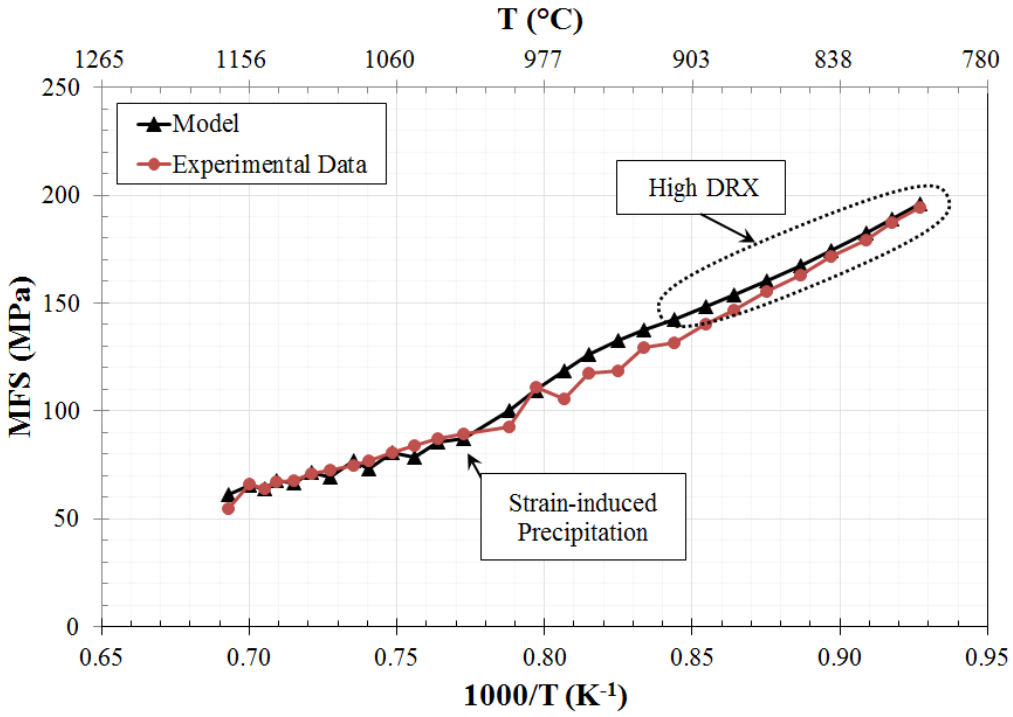

Figure 7.6: MFS graph for B-TGH10-5

Table 7.6: Microstructural and MFS predictions for B-TGH10-5.

Pass No.	T_{def} (°C)	t_{ip}	ε_a	ε_c	X_{DRX}	$[Nb]_{soln}$	Nb in C	X	d	1000/T	MFS (Model)	MFS (Torsion)
R01	1170	5	0.20	0.37	0.00	0.085	0.000	0.73	53.9	0.693	61.0	54.7
R02	1156	5	0.25	0.35	0.00	0.085	0.000	0.95	39.9	0.700	65.5	65.9
R03	1145	5	0.21	0.35	0.00	0.085	0.000	0.70	26.5	0.705	64.0	64.1
R04	1137	5	0.26	0.34	0.00	0.085	0.000	0.93	22.0	0.709	67.8	66.9
R05	1125	5	0.22	0.34	0.00	0.085	0.000	0.58	15.6	0.715	66.4	67.8
R06	1114	5	0.29	0.33	0.00	0.085	0.000	0.91	14.1	0.721	71.7	70.9
R07	1102	5	0.23	0.34	0.00	0.085	0.000	0.41	10.2	0.727	69.3	72.5
R08	1087	5	0.33	0.33	0.00	0.084	0.000	0.88	9.3	0.735	76.9	74.7
R09	1077	5	0.24	0.34	0.00	0.084	0.001	0.35	7.1	0.741	73.0	76.7
R10	1063	5	0.36	0.34	0.01	0.084	0.002	0.79	6.2	0.748	80.8	80.9
R11	1050	5	0.28	0.34	0.00	0.083	0.003	0.35	4.8	0.756	78.5	83.7
R12	1036	5	0.38	0.34	0.02	0.082	0.011	0.57	3.8	0.764	85.3	87.2
R13	1022	10	0.36	1.01	0.00	0.073	0.030	0.00	3.8	0.772	87.3	89.3
F01	996	5	0.56	0.96	0.00	0.055	0.043	0.00	3.8	0.788	100.1	92.6
F02	981	5	0.76	0.89	0.00	0.042	0.054	0.00	3.8	0.797	109.6	110.9
F03	967	5	0.96	0.84	0.11	0.031	0.062	0.00	7.5	0.806	118.8	105.3
F04	954	5	1.16	0.88	0.32	0.022	0.068	0.00	7.2	0.815	126.3	117.5
F05	940	5	1.36	0.85	0.60	0.016	0.072	0.00	6.8	0.825	132.6	118.5
F06	926	5	1.56	0.84	0.78	0.012	0.075	0.00	6.4	0.834	137.4	129.4
F07	912	5	1.76	0.85	0.89	0.009	0.078	0.00	6.1	0.844	142.6	131.6
F08	897	5	1.96	0.87	0.94	0.007	0.079	0.00	5.7	0.855	148.3	140.4
F09	884	5	2.16	0.90	0.97	0.006	0.080	0.00	5.4	0.864	153.8	146.6
F10	869	5	2.36	0.94	0.99	0.004	0.081	0.00	5.1	0.875	160.4	155.3
F11	855	5	2.56	0.99	0.99	0.004	0.082	0.00	4.8	0.887	167.4	162.8
F12	842	5	2.76	1.04	1.00	0.003	0.082	0.00	4.5	0.897	174.3	171.4
F13	827	5	2.96	1.11	1.00	0.002	0.082	0.00	4.2	0.909	182.5	179.4
F14	817	5	3.16	1.15	1.00	0.002	0.083	0.00	4.0	0.917	188.8	187.2
F15	806	-	3.36	1.21	1.00	0.002	-	-	-	0.927	195.9	194.5

B B-TGH20-5

As shown in Figure 7.7 and Table 7.7, the behavior of MFS up to pass R11 was very similar to NTG-5 schedule since the deformation variables are identical. After pass R11, a time gap was introduced and since no precipitation is predicted before the time gap, recrystallization continued. Additionally, during the time gap, the amount of Nb in carbide reached 0.02wt%, i.e. more than 5% of precipitation. Therefore, the first pass of finishing (F1, 994°C) is assumed to be when recrystallization stops. The model is in good agreement with the 1st, 3rd and 4th passes of finishing as shown in Figure 7.7. However, the model underestimates the MFS for the second finishing (F02) pass and that is probably because of the effect of precipitation hardening. For the other passes, the MFS values predicted by the model are higher by a maximum error value of 10 MPa. That is because all fluctuations after the time gap that were initially assumed to be related to SRX were not predicted. As DRX starts to take place after pass F05, the error decreased to a minimum value of 7.3 MPa.

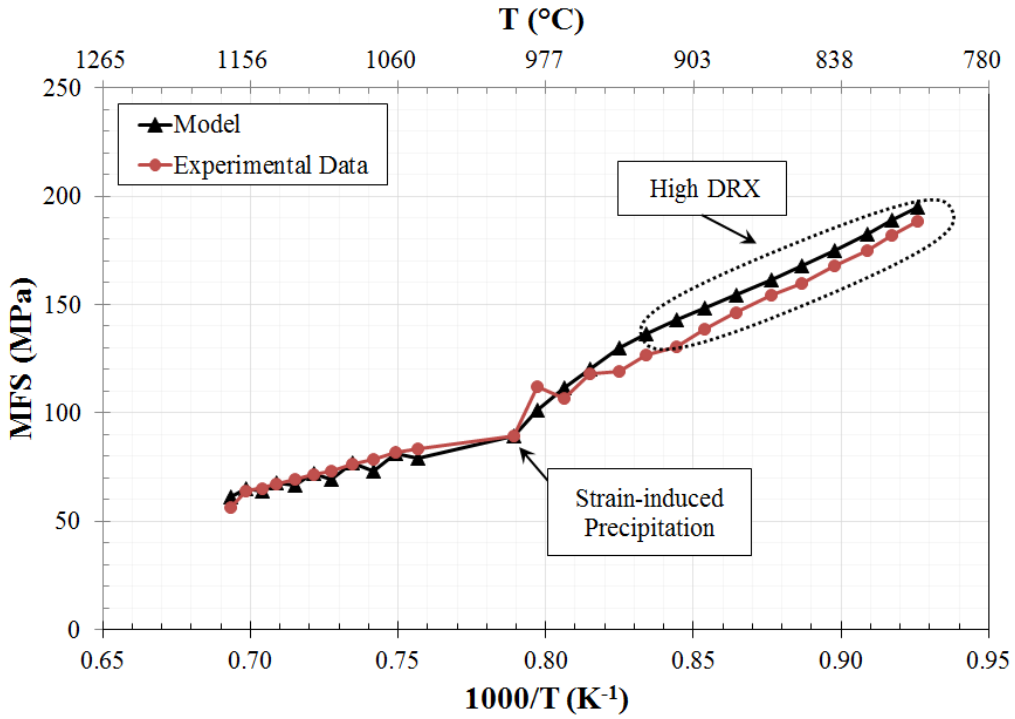

Figure 7.7: MFS graph for B-TGH20-5

Table 7.7: Microstructural and MFS predictions for B-TGH20-5.

Pass No.	T_{def} (°C)	t_{ip}	ε_a	ε_c	X_{DRX}	$[Nb]_{soln}$	Nb in C	X	d	1000/T	MFS (Model)	MFS (Torsion)
R01	1169	5	0.20	0.38	0.00	0.085	0.000	0.75	54.3	0.693	61.1	56.2
R02	1159	5	0.25	0.35	0.00	0.085	0.000	0.96	40.4	0.698	65.0	63.6
R03	1147	5	0.21	0.35	0.00	0.085	0.000	0.71	27.0	0.704	63.7	65.2
R04	1138	5	0.26	0.34	0.00	0.085	0.000	0.92	22.2	0.709	67.6	67.4
R05	1125	5	0.22	0.34	0.00	0.085	0.000	0.59	15.7	0.715	66.5	69.1
R06	1113	5	0.29	0.33	0.00	0.085	0.000	0.91	14.1	0.721	71.8	71.5
R07	1102	5	0.23	0.34	0.00	0.085	0.000	0.42	10.2	0.728	69.3	73.1
R08	1088	5	0.33	0.33	0.00	0.084	0.000	0.87	9.3	0.735	76.7	76.1
R09	1076	5	0.24	0.34	0.00	0.084	0.001	0.35	7.0	0.742	73.3	78.6
R10	1061	5	0.36	0.34	0.01	0.084	0.002	0.78	6.1	0.749	81.2	81.5
R11	1048	20	0.28	0.34	0.00	0.083	0.020	0.56	5.2	0.757	78.8	83.1
F01	994	5	0.32	1.11	0.00	0.065	0.033	0.00	5.2	0.789	89.4	89.4
F02	981	5	0.52	1.04	0.00	0.052	0.046	0.00	5.2	0.797	101.3	111.9
F03	967	5	0.72	0.96	0.00	0.039	0.056	0.00	5.2	0.806	111.3	106.7
F04	954	5	0.92	0.90	0.01	0.029	0.064	0.00	5.2	0.815	120.2	117.8
F05	939	5	1.12	0.87	0.27	0.021	0.069	0.00	6.8	0.825	129.7	119.0
F06	926	5	1.32	0.89	0.51	0.015	0.073	0.00	6.4	0.834	136.6	126.9
F07	912	5	1.52	0.89	0.72	0.012	0.076	0.00	6.1	0.844	142.8	130.7
F08	898	5	1.72	0.90	0.85	0.009	0.078	0.00	5.8	0.854	148.2	138.4
F09	884	5	1.92	0.92	0.92	0.007	0.079	0.00	5.4	0.864	154.1	146.0
F10	868	5	2.12	0.97	0.96	0.005	0.080	0.00	5.1	0.876	161.2	154.1
F11	855	5	2.32	1.00	0.98	0.004	0.081	0.00	4.8	0.887	167.6	159.9
F12	841	5	2.52	1.06	0.99	0.004	0.082	0.00	4.5	0.898	175.1	167.8
F13	827	5	2.72	1.12	0.99	0.003	0.082	0.00	4.2	0.909	182.6	174.6
F14	817	5	2.92	1.16	1.00	0.002	0.082	0.00	4.0	0.917	188.7	182.1
F15	807	-	3.12	1.21	1.00	0.002	-	-	-	0.926	195.1	188.4

C B-TGH45-5

As shown in Figure 7.8 and Table 7.8, the behavior of MFS up to pass R6 was very similar to NTG-5 schedule since the deformation variables are identical. After pass R6, a time gap was introduced and since no precipitation occurred before the time gap, recrystallization continued. The fractional softening due to SRX was very minor (X = 0.02) between the first and second passes of finishing. Additionally, during the time gap, the amount of Nb in carbide form reached 0.004wt%, i.e. almost equal to 5% of precipitation, which stops SRX. So, in the second pass of finishing (F02, 982°C) 5% strain induced precipitation is exceeded hence, recrystallization stops. The model is in good agreement with the whole deformation schedule except for 2nd, 3rd and 4th passes of finishing as shown in Figure 7.8 and that is probably because of the effect of precipitation hardening. Dynamic recrystallization starts to take place after pass F08 (899°C), which is the lowest temperature for the occurrence of DRX compared to NTG-5, TGH10-5 and THH20 schedules.

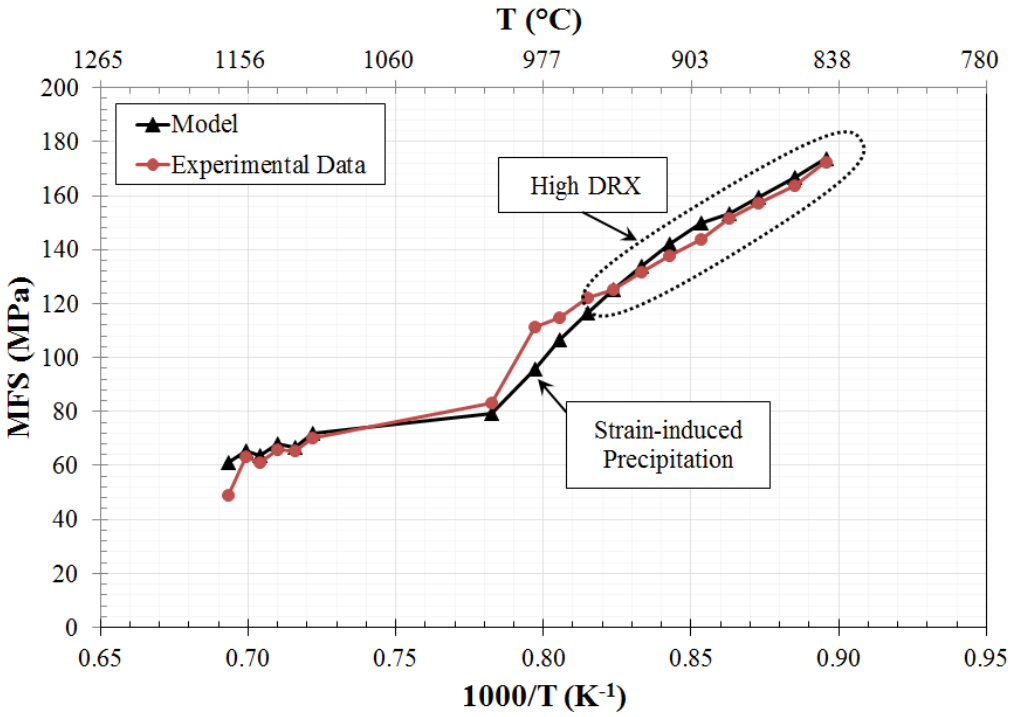

Figure 7.8: MFS graph for B-TGH45-5

Table 7.8: Microstructural and MFS predictions for B-TGH45-5.

Pass No.	T_{def} (°C)	t_{ip}	ε_a	ε_c	X_{DRX}	$[Nb]_{soln}$	Nb in C	X	d	1000/T	MFS (Model)	MFS (Torsion)
R01	1170	5	0.20	0.37	0.00	0.085	0.000	0.74	54.1	0.693	61.1	49.1
R02	1157	5	0.25	0.35	0.00	0.085	0.000	0.96	40.2	0.699	65.2	63.1
R03	1147	5	0.21	0.35	0.00	0.085	0.000	0.70	26.6	0.704	63.8	60.9
R04	1136	5	0.26	0.34	0.00	0.085	0.000	0.92	21.8	0.710	68.0	65.9
R05	1124	5	0.22	0.34	0.00	0.085	0.000	0.58	15.4	0.716	66.7	65.4
R06	1112	45	0.29	0.33	0.00	0.085	0.004	1.00	87.3	0.722	72.0	70.4
F01	1005	5	0.20	0.57	0.00	0.081	0.017	0.02	84.7	0.783	79.3	83.3
F02	982	5	0.40	1.81	0.00	0.068	0.033	0.00	84.7	0.797	95.5	111.3
F03	969	5	0.60	1.65	0.00	0.051	0.047	0.00	84.7	0.805	106.7	114.7
F04	954	5	0.80	1.51	0.00	0.038	0.058	0.00	84.7	0.815	116.5	121.9
F05	941	5	1.00	1.41	0.00	0.027	0.065	0.00	84.7	0.824	125.3	125.3
F06	927	5	1.20	1.36	0.00	0.020	0.070	0.00	84.7	0.833	133.9	131.6
F07	913	5	1.40	1.34	0.03	0.014	0.074	0.00	84.7	0.843	142.2	137.9
F08	899	5	1.60	1.36	0.25	0.011	0.076	0.00	5.8	0.853	149.9	143.8
F09	886	5	1.80	0.94	0.86	0.008	0.078	0.00	5.5	0.863	153.5	151.4
F10	873	5	2.00	0.96	0.93	0.006	0.080	0.00	5.2	0.873	159.2	157.4
F11	857	5	2.20	1.01	0.96	0.005	0.081	0.00	4.8	0.885	166.8	163.7
F12	844	-	2.40	1.05	0.98	0.004	-	-	-	0.896	173.6	172.2

D B-TGL10-5

As shown in Figure 7.9 and Table 7.9, the behavior of MFS up to pass R15 was very similar to NTG-5 schedule since the deformation variables are identical. The amount of Nb in carbide form reached 0.006wt%, i.e. more than 5% of precipitation, during the interpass time of pass R12. Therefore, pass R13 (1025°C) is when recrystallization stops. After pass R15, a time gap of 10 seconds was incorporated. The model overestimates the MFS values for several passes after the time gap by a maximum error value of 17 MPa probably as a result of an incorrect estimate of strain accumulation. As DRX starts to take place after pass F02, the model slowly converges with torsion data.

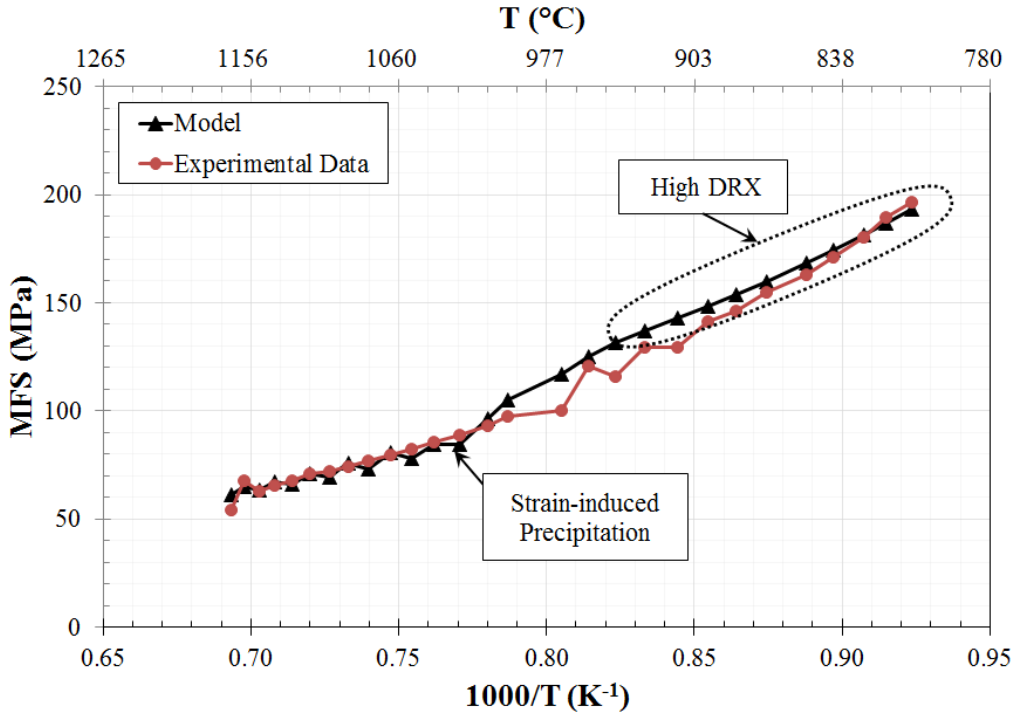

Figure 7.9: MFS graph for B-TGL10-5

Table 7.9: Microstructural and MFS predictions for B-TGL10-5.

Pass No.	T_{def} (°C)	t_{ip}	ε_a	ε_c	X_{DRX}	$[Nb]_{soln}$	Nb in C	X	d	1000/T	MFS (Model)	MFS (Torsion)
R01	1169	5	0.20	0.38	0.00	0.085	0.000	0.75	54.5	0.693	61.1	54.0
R02	1160	5	0.25	0.35	0.00	0.085	0.000	0.96	40.6	0.698	64.9	67.4
R03	1150	5	0.21	0.35	0.00	0.085	0.000	0.72	27.4	0.703	63.4	62.8
R04	1140	5	0.26	0.33	0.00	0.085	0.000	0.93	22.7	0.708	67.3	65.5
R05	1128	5	0.22	0.34	0.00	0.085	0.000	0.61	16.2	0.714	66.1	67.9
R06	1116	5	0.29	0.33	0.00	0.085	0.000	0.90	14.5	0.720	71.2	70.7
R07	1103	5	0.23	0.34	0.00	0.085	0.000	0.45	10.5	0.727	69.2	71.9
R08	1092	5	0.33	0.33	0.00	0.084	0.000	0.87	9.6	0.733	75.9	74.4
R09	1079	5	0.24	0.34	0.00	0.084	0.001	0.36	7.2	0.740	72.9	76.6
R10	1066	5	0.35	0.34	0.01	0.084	0.002	0.80	6.4	0.747	80.4	79.5
R11	1053	5	0.27	0.34	0.00	0.083	0.003	0.35	5.0	0.754	77.9	82.3
R12	1039	5	0.38	0.34	0.02	0.082	0.006	0.68	4.2	0.762	84.7	85.4
R13	1025	5	0.32	1.06	0.00	0.079	0.019	0.00	4.2	0.770	84.5	88.6
R14	1009	5	0.52	1.02	0.00	0.065	0.034	0.00	4.2	0.780	96.2	93.1
R15	998	10	0.72	0.93	0.00	0.051	0.051	0.00	4.2	0.787	105.1	97.6
F01	969	5	0.92	0.88	0.02	0.034	0.060	0.00	4.2	0.805	116.8	99.9
F02	955	5	1.12	0.83	0.33	0.025	0.067	0.00	7.2	0.814	125.3	120.5
F03	942	5	1.32	0.87	0.53	0.018	0.071	0.00	6.8	0.823	131.7	115.9
F04	927	5	1.52	0.85	0.74	0.013	0.075	0.00	6.5	0.833	137.2	129.2
F05	912	5	1.72	0.86	0.86	0.010	0.077	0.00	6.1	0.844	142.8	129.5
F06	897	5	1.92	0.88	0.93	0.008	0.079	0.00	5.7	0.855	148.4	141.4
F07	884	5	2.12	0.91	0.96	0.006	0.080	0.00	5.4	0.864	153.8	146.0
F08	871	5	2.32	0.94	0.98	0.005	0.081	0.00	5.1	0.874	159.7	155.0
F09	853	5	2.52	1.00	0.99	0.004	0.082	0.00	4.8	0.888	168.3	163.2
F10	842	5	2.72	1.04	1.00	0.003	0.082	0.00	4.5	0.897	174.3	171.3
F11	829	5	2.92	1.10	1.00	0.003	0.082	0.00	4.3	0.907	181.4	180.4
F12	820	5	3.12	1.14	1.00	0.002	0.083	0.00	4.1	0.915	186.9	189.5
F13	810	-	3.32	1.19	1.00	0.002	-	-	-	0.923	193.2	196.4

E B-TGL20-5

As shown in Figure 7.10 and Table 7.10, the behavior of MFS up to pass R15 was very similar to NTG-5 schedule since the deformation variables are identical. The differences between the model and measurements can be explained as per the previous schedule.

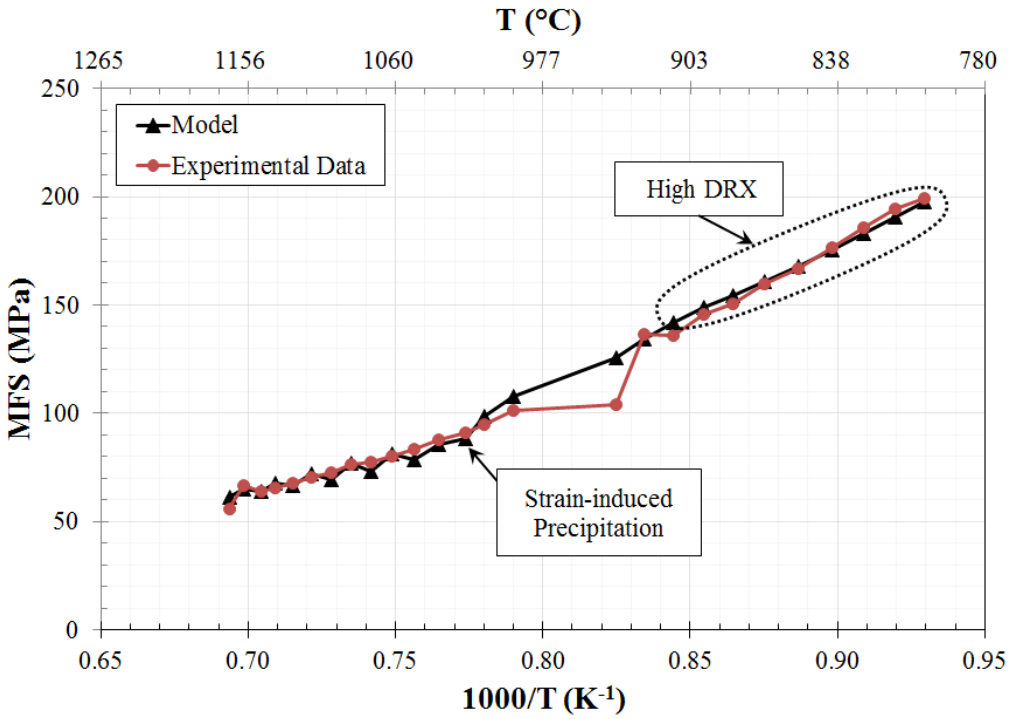

Figure 7.10: MFS graph for B-TGL20-5

Table 7.10: Microstructural and MFS predictions for B-TGL20-5.

Pass No.	T_{def} (°C)	t_{ip}	ε_a	ε_c	X_{DRX}	$[Nb]_{soln}$	Nb in C	X	d	1000/T	MFS (Model)	MFS (Torsion)
R01	1169	5	0.20	0.38	0.00	0.085	0.000	0.74	54.2	0.694	61.2	55.6
R02	1158	5	0.25	0.35	0.00	0.085	0.000	0.96	40.2	0.699	65.1	66.7
R03	1147	5	0.21	0.35	0.00	0.085	0.000	0.70	26.7	0.704	63.8	63.9
R04	1137	5	0.26	0.34	0.00	0.085	0.000	0.93	22.1	0.709	67.8	65.7
R05	1125	5	0.22	0.34	0.00	0.085	0.000	0.58	15.6	0.715	66.5	67.8
R06	1113	5	0.29	0.33	0.00	0.085	0.000	0.91	14.0	0.721	71.8	70.3
R07	1100	5	0.23	0.34	0.00	0.085	0.000	0.41	10.2	0.728	69.5	72.8
R08	1087	5	0.33	0.33	0.00	0.084	0.000	0.87	9.2	0.735	76.9	76.1
R09	1075	5	0.24	0.34	0.00	0.084	0.001	0.35	7.0	0.742	73.3	77.6
R10	1062	5	0.36	0.34	0.01	0.084	0.002	0.79	6.2	0.749	81.0	80.2
R11	1049	5	0.28	0.34	0.00	0.083	0.003	0.35	4.8	0.756	78.5	83.2
R12	1035	5	0.38	0.34	0.02	0.082	0.012	0.54	3.7	0.765	85.5	87.7
R13	1019	5	0.37	1.01	0.00	0.072	0.025	0.00	3.7	0.774	88.2	90.7
R14	1009	5	0.57	0.94	0.00	0.059	0.039	0.00	3.7	0.780	98.3	94.6
R15	993	20	0.77	0.88	0.00	0.046	0.058	0.00	3.7	0.790	107.7	101.1
F01	939	5	0.97	0.89	0.06	0.027	0.065	0.00	6.8	0.825	125.5	103.9
F02	925	5	1.17	0.94	0.24	0.019	0.070	0.00	6.4	0.834	134.5	136.2
F03	912	5	1.37	0.92	0.53	0.014	0.074	0.00	6.1	0.844	142.1	135.9
F04	897	5	1.57	0.93	0.73	0.011	0.076	0.00	5.7	0.855	148.7	145.6
F05	884	5	1.77	0.94	0.85	0.008	0.078	0.00	5.4	0.865	154.5	150.5
F06	870	5	1.97	0.97	0.92	0.006	0.080	0.00	5.1	0.875	160.7	159.5
F07	855	5	2.17	1.02	0.95	0.005	0.081	0.00	4.8	0.887	167.9	166.9
F08	841	5	2.37	1.07	0.98	0.004	0.081	0.00	4.5	0.898	175.3	176.5
F09	827	5	2.57	1.13	0.99	0.003	0.082	0.00	4.2	0.909	182.7	185.8
F10	814	5	2.77	1.19	0.99	0.003	0.082	0.00	4.0	0.920	190.5	194.1
F11	803	-	2.97	1.25	1.00	0.002	-	-	-	0.929	197.8	199.0

F B-TGL45-5

As shown in Figure 7.11 and Table 7.11, the behavior of MFS up to pass R15 was very similar to NTG-5 schedule since the deformation variables are identical. The differences between the model and measurements can be explained as per the previous schedule.

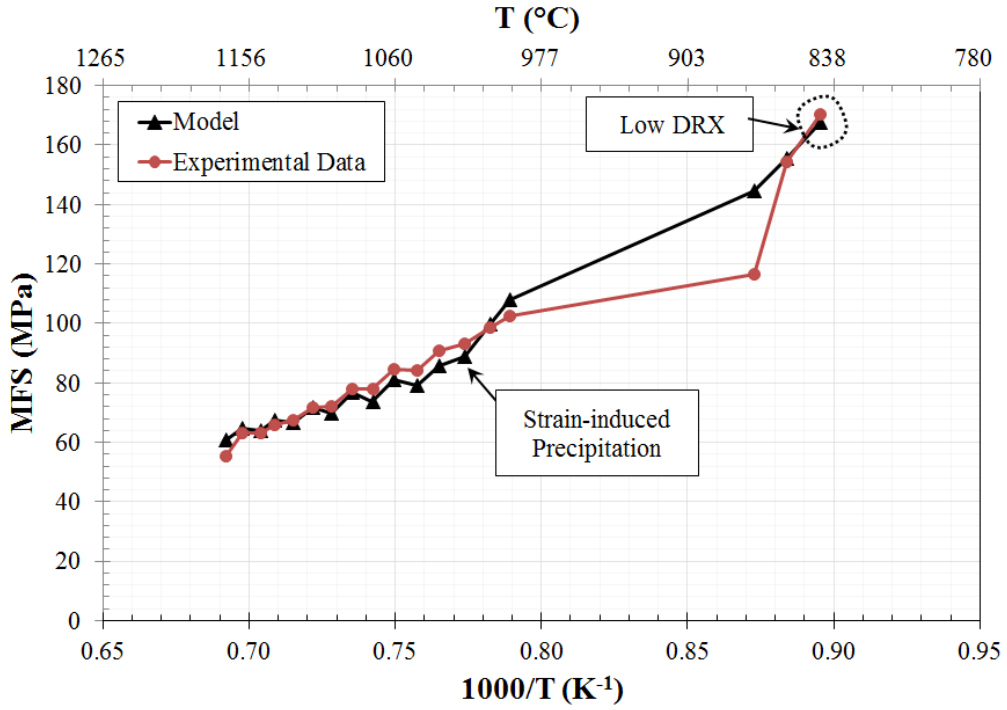

Figure 7.11: MFS graph for B-TGL45-5

Table 7.11: Microstructural and MFS predictions for B-TGL45-5.

Pass No.	T_{def} (°C)	t_{ip}	ε_a	ε_c	X_{DRX}	$[Nb]_{soln}$	Nb in C	X	d	1000/T	MFS (Model)	MFS (Torsion)
R01	1172	5	0.20	0.37	0.00	0.085	0.000	0.77	55.2	0.692	60.9	55.2
R02	1160	5	0.25	0.35	0.00	0.085	0.000	0.95	41.3	0.698	64.7	63.2
R03	1148	5	0.21	0.35	0.00	0.085	0.000	0.72	27.4	0.704	63.8	63.2
R04	1138	5	0.26	0.34	0.00	0.085	0.000	0.92	22.4	0.709	67.6	65.9
R05	1125	5	0.22	0.34	0.00	0.085	0.000	0.59	15.8	0.715	66.6	67.6
R06	1112	5	0.29	0.33	0.00	0.085	0.000	0.90	14.0	0.722	71.8	71.7
R07	1100	5	0.23	0.34	0.00	0.085	0.000	0.43	10.1	0.728	69.7	72.0
R08	1087	5	0.33	0.33	0.00	0.084	0.000	0.86	9.1	0.735	76.8	77.8
R09	1074	5	0.25	0.34	0.00	0.084	0.001	0.36	6.9	0.742	73.6	78.1
R10	1061	5	0.36	0.34	0.01	0.084	0.002	0.78	6.0	0.750	81.2	84.6
R11	1047	5	0.28	0.34	0.00	0.083	0.003	0.36	4.7	0.757	79.1	84.3
R12	1034	5	0.38	0.34	0.02	0.081	0.013	0.49	3.5	0.765	85.6	90.7
R13	1020	5	0.39	1.00	0.00	0.071	0.027	0.00	3.5	0.774	89.1	93.3
R14	1005	5	0.59	0.94	0.00	0.058	0.040	0.00	3.5	0.783	99.7	98.6
R15	994	45	0.79	0.86	0.00	0.044	0.063	0.00	3.5	0.789	108.0	102.3
F01	873	5	0.99	1.15	0.00	0.022	0.068	0.00	3.5	0.873	144.5	116.5
F02	858	5	1.19	1.14	0.03	0.016	0.072	0.00	3.5	0.884	155.5	154.2
F03	844	-	1.39	1.16	0.24	0.012	-	-	-	0.896	167.6	170.3

7.5 Model Validity and Consistency

In general, the developed model provides good MFS predictions for HSLA steels with a consistent microstructural evolution rationale to explain the measured MFS values. Discrepancies arise when precipitation strengthening takes place, which leads to inconsistencies between MFS predictions and the experimental data for the first few passes of finishing stage, especially below the T_{nr} temperature. Precipitation strengthening also might affect the activation energy for hot deformation and therefore influences the consistency of the model. The model also is not capable of predicting the fluctuation behavior after the time gap since strain induced precipitation is usually predicted to occur prior to the time gap or at the first finishing pass.

Chapter-8

CONCLUSION AND FUTURE WORK

8.1 Conclusions

The effect of time gap on mean flow stress behavior of HSLA steels was investigated by torsion testing and by developing a mathematical model to predict MFS during deformation. In this present study, the following points can be summarized.

1. A mathematical model was developed for the predication of MFS behavior of HSLA steels during hot rolling. The model is based on Misaka equation which is valid only for full static recrystallization. Therefore, different approaches were suggested to take into account the effect of Nb in solution, strain accumulation, strain induced precipitation, and static, metadynamic and dynamic recrystallization on MFS behavior. There was good agreement between the experimental and predicted mean flow stresses over most of the deformation schedules. However, some discrepancies in the MFS values were observed for the first few passes of finishing stage especially when precipitation hardening is more likely to occur.

2. For average schedules of short interpass time (5 seconds), a systematic rise and fall of the MFS at high temperatures indicates the effect of solute drag as revealed by both experimental and model data. This fluctuation behavior is associated with repeated cycles of strain accumulation and static recrystallization. Therefore, a new concept was proposed to determine the temperature of no recrystallization as the point at which the fluctuating behaviour stops.

3. For average schedules of long interpass time (30 seconds), the model underestimated the MFS values after the occurrence of precipitation, which is probably related to precipitation hardening. For this case, dynamic recrystallization is totally absent because of the increase in the deformation activation energy. Thus, the critical strain was higher and not achievable in this condition.

4. For short time gaps (10 to 20 seconds), fluctuations in MFS values during finishing were observed in the torsion data for all deformation schedules, except for A-TGL20-

5 schedule, in which the time gap was introduced at relatively low temperatures and thus, precipitation stopped these fluctuations. If the presence of fluctuations indicates either an absence of precipitates (at very high temperatures) or the presence of very few precipitates (close to the T_{nr}), then it appears that the time gap has slowed down precipitation kinetics for TGH10, TGH20 and TGL10 schedules. These fluctuations were not predicted by the model since it was assumed that recrystallization stops completely when 5% of precipitates are formed regardless of the possible effect of using different time gaps on the precipitation kinetics and the activation energy for hot deformation.

5. For the case of long time gaps, the temperature of the first finishing pass decreased below a critical temperature, which would minimize or eliminate the extent of fluctuations (i.e. static recrystallization) in finishing due to the presence of very fine precipitation as a consequence of increasing the driving force for precipitation. Therefore, a high sudden jump in MFS occurs in the second finishing pass, showing an evidence of strain induced precipitation that was formed after the first finishing pass.

6. A drop in MFS value of the first finishing pass was observed in all deformation schedules. This suggests that recrystallization takes place during the time gap, even when the time gap is below the T_{nr} temperature predicted by the average schedule. This is because, it was initially assumed that recrystallization completely stops when 5% precipitation are formed. However, it is believed some recrystallization can occur with longer time gaps. Hence, for TGH schedules, this drop in MFS was predicted by the model, whereas it was overestimated for TGL schedules.

8.2 Future Work

1. Modelling of the effect of precipitation hardening on mean flow stress during finishing. The model should describe precipitation hardening in terms of the effective pinning force for precipitates.

2. The interaction between precipitation and recrystallization when different time gaps are to be investigated. Also, the validity of assuming that recrystallization stops when 5% of precipitates are formed needs to be revisited. Because different steels can have different amounts of Nb, different criteria should be made to determine when recrystallization stops completely depending on the weight percent of Nb in carbonitrides and size of precipitates.

3. Modeling the effect of using different time gaps on the activation energy for hot deformation.

REFERENCES

1. Hodgson, P.D., *Mathematical Modelling of Recrystallisation Processes During the Hot Rolling of Steel.* PhD Thesis, University of Queensland, Australia, 1993.
2. Schey, J.A., *Introduction to Manufacturing Processes - 3rd Edition*. 2000, New York: McGraw-Hill.
3. Orowan, E. and K.J. Pascoe, *A Simple Method of Calculating Roll Pressure and Power Consumption in Flat Hot Rolling.* Iron and Steel Institute (London), 1946(34): p. 124-126.
4. Bland, D.R. and H. Ford, *The Calculation of Roll Force and Torque in Cold Strip Rolling with Tensions.* Proc. I. Mech. E, 1948. **139**: p. 144.
5. Sims, R.B., *The Calculation of Roll Force and Torque in Hot Rolling Mills.* Proc. Inst. Mech. Eng., 1954(168): p. 191–200.
6. Cook, P. and M. A., *The Calculation of Load and Torque in Hot Flat Rolling.* The British Iron and Steel Research Association, London, 1938.
7. Sellars, C.M., *Modeling Microstructural Development During Hot-Rolling.* Materials Science and Technology, 1990. **6**(11): p. 1072-1081.
8. Beynon, J.H. and C.M. Sellars, *Modeling Microstructure and Its Effects During Multipass Hot-Rolling.* ISIJ International, 1992. **32**(3): p. 359-367.
9. Calvo, J., et al., *Influence of the Chemical Composition on Transformation Behaviour of Low Carbon Microalloyed Steels.* Materials Science and Engineering: A, 2009. **520**(1): p. 90-96.
10. Dieter, G.E., *Mechanical Metallurgy*. Vol. 3. 1986, New York: McGraw-Hill p. 586-612.
11. Lenard, J.G., *Primer on Flat Rolling*. 2007, London: Elsevier Science Limited. p. 3-7.
12. Maccagno, T.M., et al., *Determination of Recrystallization Stop Temperature from Rolling-Mill Logs and Comparison with Laboratory Simulation Results.* ISIJ International, 1994. **34**(11): p. 917-922.
13. Hitchcock, J.H., *Roll Neck Bearings.* ASME Research Publication, New York, 1935: p. 33.

14. Siciliano, F., et al., *Mathematical Modeling of the Mean Flow Stress, Fractional Softening and Grain Size During the Hot Strip Rolling of C-Mn Steels.* ISIJ International, 1996. **36**(12): p. 1500-1506.
15. Minami, K., et al., *Mathematical Modeling of Mean Flow Stress During the Hot Strip Rolling of Niobium Steels.* ISIJ International, 1996. **36**(12): p. 1507-1515.
16. Yue, S., *The Mathematical Modelling of Hot Rolling of Steel.* Metal Forming Science and Practice: A State-of-the-Art Volume in Honour of Professor JA Schey's 80th Birthday, (ed. Lenard J.G.), Elsevier, Amsterdam, 2002: p. 213.
17. Ford, H. and J.M. Alexander, *Simplified Hot-Rolling Calculations.* Journal of the Institute of Metals, 1964. **92**(12): p. 397-&.
18. Hill, R., *The Mathematical Theory of Plasticity*. Vol. 11. 1998: Oxford University Press, USA.
19. Boratto, F., et al., *The 3 Critical-Temperatures of the Hot-Rolling of Microalloyed Steels.* CIM Bulletin, 1988. **81**(914): p. 71.
20. Siciliano, F. and J.J. Jonas, *Mathematical Modeling of the Hot Strip Rolling of Microalloyed Nb, Multiply-Alloyed Cr-Mo, and Plain C-Mn Steels.* Metallurgical and Materials Transactions A, 2000. **31**(2): p. 511-530.
21. Misaka, Y. and T. Yoshimoto, *Formularization of Mean Resistance to Deformation of Plain Carbon Steels at Elevated Temperature.* Journal of The Japan Soc. Tec. Plasticity, 1967. **8**(79): p. 414-422.
22. Devadas, C., I.V. Samarasekera, and E.B. Hawbolt, *The Thermal and Metallurgical State of Steel Strip During Hot Rolling: Part Iii. Microstructural Evolution.* Metallurgical and Materials Transactions A, 1991. **22**(2): p. 335-349.
23. Kirihata, A., et al., *Mathematical Modelling of Mean Flow Stress During the Hot Strip Rolling of Multiply-Alloyed Medium Carbon Steels.* ISIJ International, 1998. **38**(2): p. 187-195.
24. Shida, S., *Effect of Carbon Content, Temperature and Strain Rate on Compressive Flow Stress of Carbon Steel.* Hitachi Res. Lab. Report, 1974: p. 1-9.
25. Biglou, J.A., M.S. Chun, and J.G. Lenard, *A Comparative Study of Flow Stress Modeling by Artificial Neural Networks and Statistical Methods.* Iron and Steelmaker (USA), 1998. **25**(6): p. 61.

26. Karjalainen, L.P., T.M. Maccagno, and J.J. Jonas, *Softening and Flow Stress Behaviour of Nb Microalloyed Steels During Hot Rolling Simulation.* ISIJ International, 1995. **35**(12): p. 1523-1531.
27. Johnson, G.R. and W.H. Cook, *A Constitutive Model and Data for Metals Subjected to Large Strains, High Strain Rates and High Temperatures,* in *Proceedings of the 7th International Symposium on Ballistics*. 1983, The Hague, Netherlands: International Ballistics Committee. p. 541-547.
28. Lee, W.S. and G.W. Yeh, *The Plastic Deformation Behaviour of A.I.S.I. 4340 Alloy Steel Subjected to High Temperature and High Strain Rate Loading Conditions.* Journal of Materials Processing Technology, 1997. **71**(2): p. 224-234.
29. Kim, S.I., Y. Lee, and S.M. Byon, *Study on Constitutive Relation of A.I.S.I. 4140 Steel Subject to Large Strain at Elevated Temperatures.* Journal of Materials Processing Technology, 2003. **140**(1): p. 84-89.
30. Voce, E., *Practical Strain-Hardening Function.* Metallurgia, 1955. **51**(307): p. 219-226.
31. Kim, S.I. and Y.C. Yoo, *Dynamic Recrystallization Behavior of A.I.S.I. 304 Stainless Steel.* Materials Science and Engineering A, 2001. **311**(1-2): p. 108-113.
32. Medina, S.F. and C.A. Hernandez, *Modelling of the Dynamic Recrystallization of Austenite in Low Alloy and Microalloyed Steels.* Acta Materialia, 1996. **44**(1): p. 165-171.
33. Kim, S.I. and Y.C. Yoo, *Prediction of Dynamic Recrystallisation Behaviour of A.I.S.I. Type 4140 Medium Carbon Steel.* Materials Science and Technology, 2002. **18**(2): p. 160-164.
34. Avrami, M., *Granulation, Phase Change, and Microstructure - Kinetics of Phase Change. Iii.* Journal of Chemical Physics, 1941. **9**(2): p. 177-184.
35. Laasraoui, A. and J.J. Jonas, *Prediction of Steel Flow Stresses at High-Temperatures and Strain Rates.* Metallurgical and Materials Transactions A, 1991. **22**(7): p. 1545-1588.
36. Petkovic, R.A., M.J. Luton, and J.J. Jonas, *Recovery and Recrystallization of Polycrystalline Copper after Hot Working.* Acta Metallurgica, 1979. **27**(10): p. 1633-1648.

37. McQueen, H.J. and J.J. Jonas, *Role of the Dynamic and Static Softening Mechanisms in Multistage Hot Working.* Journal of Applied Metalworking, 1985. **3**(4): p. 410-420.
38. McQueen, H.J. and J.J. Jonas, *Recovery and Recrystallization During High Temperature Deformation* Plastic Deformation of Metals, 1975: p. 393-493.
39. Doherty, R.D., et al., *Current Issues in Recrystallization: A Review.* Materials Science and Engineering: A, 1997. **238**(2): p. 219-274.
40. Cahn, R.W., *Recovery and Recrystallization.* Physical Metallurgy, 1970: p. 1129-1197.
41. Sellars, C.M., *Recrystallization of Metals During Hot Deformation.* Philosophical Transactions of the Royal Society A-Mathematical Physical and Engineering Sciences, 1978. **288**(1350): p. 147-158.
42. Djaic, R.A.P. and J.J. Jonas, *Recrystallization of High-Carbon Steel between Intervals of High-Temperature Deformation.* Metallurgical Transactions, 1973. **4**(2): p. 621-624.
43. Glover, G. and C.M. Sellars, *Recovery and Recrystallization During High Temperature Deformation of Alpha-Iron.* Metallurgical Transactions, 1973. **4**(3): p. 765-775.
44. Barraclough, D.R., *Hot Working and Recrystallisation of a Stainless and a Low Alloy Steel.* Ph.D. thesis, University of Sheffield, UK, 1974.
45. Djaic, R.A.P. and J.J. Jonas, *Static Recrystallization of Austenite between Intervals of High Temperature Deformation (Microfilm)*. 1972, Ottawa: National Library of Canada.
46. SICILIANO, J.R.F., et al., *Mathematical Modeling of the Mean Flow Stress, Fractional Softening and Grain Size During the Hot Strip Rolling of C-Mn Steels.* ISIJ international, 1996. **36**(12): p. 1500-1506.
47. Pussegoda, L.N., S. Yue, and J.J. Jonas, *Laboratory Simulation of Seamless Tube Piercing and Rolling Using Dynamic Recrystallization Schedules.* Metallurgical and Materials Transactions A, 1990. **21**(1): p. 153-164.
48. Samuel, F.H., et al., *Effect of Dynamic Recrystallization on Microstructural Evolution During Strip Rolling.* ISIJ International, 1990. **30**(3): p. 216-225.

49. Sun, W.P. and E.B. Hawbolt, *Comparison between Static and Metadynamic Recrystallization: An Application to the Hot Rolling of Steels.* ISIJ international, 1997. **37**(10): p. 1000-1009.
50. Kowalski, B., C.M. Sellars, and M. Pietrzyk, *Development of a Computer Code for the Interpretation of Results of Hot Plane Strain Compression Tests.* ISIJ international, 2000. **40**(12): p. 1230-1236.
51. Sakai, T. and J.J. Jonas, *Overview No. 35 Dynamic Recrystallization: Mechanical and Microstructural Considerations.* Acta Metallurgica, 1984. **32**(2): p. 189-209.
52. Luton, M.J. and C.M. Sellars, *Dynamic Recrystallization in Nickel and Nickel-Iron Alloys During High Temperature Deformation.* Acta Metallurgica, 1969. **17**(8): p. 1033-1043.
53. Sellars, C.M. and W.J. Tegart, *On the Mechanism of Hot Deformation.* Acta Metallurgica, 1966. **14**(9): p. 1136-1138.
54. Senuma, T., et al., *Structure of Austen-Ite of Carbon Steels in High Speed Hot Working Processes.* Tetsu to Hagane, 1984. **70**(15): p. 2112-2119.
55. Yada, H., in *Int. Symp. on Accelerated Cooling of Rolled Steel*, G.E.R.a.A.F. Crawley, Editor. 1988: Pergamon. p. 105.
56. Pereda, B., et al., *Effect of Mo on Dynamic Recrystallization Behavior of Nb-Mo Microalloyed Steels.* ISIJ International, 2007. **47**(6): p. 860-868.
57. Serajzadeh, S., *Thermomechanical Modelling of Hot Slab Rolling.* Materials Science and Technology, 2005. **21**(1): p. 93-102.
58. Poliak, E.I. and J.J. Jonas, *Initiation of Dynamic Recrystallization in Constant Strain Rate Hot Deformation.* ISIJ International, 2003. **43**(5): p. 684-691.
59. Elwazri, A.M., P. Wanjara, and S. Yue, *Dynamic Recrystallization of Austenite in Microalloyed High Carbon Steels.* Materials Science and Engineering: A, 2003. **339**(1–2): p. 209-215.
60. Roucoules, C., S. Yue, and J.J. Jonas, *Modelling of Metal Rolling Processes*. 1993, The Institute of Materials, London, UK. p. 165.
61. Siciliano, F., *Mathematical Modeling of the Hot Strip Rolling of Nb Microalloyed Steels.* PhD Thesis, McGill University, Canada, 1999.

62. Cho, S.H., K.B. Kang, and J.J. Jonas, *Mathematical Modeling of the Recrystallization Kinetics of Nb Microalloyed Steels.* ISIJ International, 2001. **41**(7): p. 766-773.
63. Bowden, J.W., F.H. Samuel, and J.J. Jonas, *Effect of Interpass Time on Austenite Grain Refinement by Means of Dynamic Recrystallization of Austenite.* Metallurgical and Materials Transactions A, 1991. **22**(12): p. 2947-2957.
64. Sellars, C.M. and G.J. Davies. *Hot Working and Forming Processes*. in *International Conference on Hot Working and Forming Processes*. 1980. Maney Pub.
65. Roucoules, C., S. Yue, and J.J. Jonas, *Effect of Dynamic and Metadynamic Recrystallization on Rolling Load and Microstructure*, in *Proc. Int. Conf. on Modelling of Metal Rolling Processes*. 1993: London, UK. p. 165-179.
66. Hodgson, P.D. and D.C. Collinson, *The Calculation of Hot Strength in Plate and Strip Rolling of Niobium Microalloyed Steels*, in *Proceedings of the Symposium Mathematical Modelling of Hot Rolling of Steel*, S. Yue, Editor. 1990: Hamilton. p. 239-251.
67. Sakui, S., T. Sakai, and K. Takeishi, *Hot Deformation of Austenite in a Plain Carbon-Steel.* Transactions of the Iron and Steel Institute of Japan, 1977. **17**(12): p. 718-725.
68. Rossard, C., *Mechanical and Structural Behaviour under Hot Working Conditions.* Inst Met (London) Monogr Rep Ser, 1973. **2**(3): p. 175-203.
69. Ryan, N.D. and H.J. Mcqueen, *Flow-Stress, Dynamic Restoration, Strain-Hardening and Ductility in Hot-Working of 316-Steel.* Journal of Materials Processing Technology, 1990. **21**(2): p. 177-199.
70. Shaban, M. and B. Eghbali, *Determination of Critical Conditions for Dynamic Recrystallization of a Microalloyed Steel.* Materials Science and Engineering: A, 2010. **527**(16–17): p. 4320-4325.
71. Stewart, G.R., et al., *Modelling of Dynamic Recrystallisation Kinetics in Austenitic Stainless and Hypereutectoid Steels.* Materials Science and Technology, 2006. **22**(5): p. 519-524.

72. Roucoules, C., S. Yue, and J.J. Jonas, *Effect of Alloying Elements on Metadynamic Recrystallization in High-Strength Low-Alloy Steels.* Metallurgical and Materials Transactions A, 1995. **26**(1): p. 181-190.
73. Siciliano, F. and J.J. Jonas, *Modeling the Critical Strain for the Initiation of Dynamic Recrystallization During the Hot Strip Rolling of Niobium Microalloyed Steels*, in *Materials Science Forum*. 1998, Trans Tech Publ. p. 377-384.
74. Elwazri, A.M., E. Essadiqi, and S. Yue, *Kinetics of Metadynamic Recrystallization in Microalloyed Hypereutectoid Steels.* ISIJ International, 2004. **44**(4): p. 744-752.
75. Hodgson, P.D. and R.K. Gibbs, *A Mathematical Model to Predict the Mechanical Properties of Hot Rolled C-Mn and Microalloyed Steels.* ISIJ International, 1992. **32**(12): p. 1329-1338.
76. Roucoules, C., et al., *Softening and Microstructural Change Following the Dynamic Recrystallization of Austenite.* Metallurgical and Materials Transactions A, 1994. **25**(2): p. 389-400.
77. Hodgson, P.D., et al., *Microalloying'95*. ISS, Pittsburgh, PA, 1995. **341**.
78. Li, G., et al., *Effect of Initial Grain Size on the Static Recrystallization Kinetics of Nb Microalloyed Steels.* ISIJ International, 1996. **36**(12): p. 1479-1485.
79. Uranga, P., et al., *Transition between Static and Metadynamic Recrystallization Kinetics in Coarse Nb Microalloyed Austenite.* Materials Science and Engineering: A, 2003. **345**(1): p. 319-327.
80. Fernández, A.I., et al., *Static Recrystallization Behaviour of a Wide Range of Austenite Grain Sizes in Microalloyed Steels.* ISIJ International, 2000. **40**(9): p. 893-901.
81. Hodgson, P.D., J.J. Jonas, and S. Yue, *Strain Accumulation and Post-Dynamic Recrystallization in C-Mn Steels*, in *Mater. Sci. Forum*. 1993, Trans Tech Publ. p. 473-478.
82. Luton, M.J., R. Dorvel, and R.A. Petkovic, *Interaction between Deformation, Recrystallization and Precipitation in Niobium Steels.* Metallurgical Transactions A, 1980. **11**(3): p. 411-420.

83. Bai, D.Q., S. Yue, and J.J. Jonas, *Metadynamic Recrystallization of Low Carbon Steels Containing Nb*, in *Symposium on Thermomechanical Processing of Steel as held at the 39 th Annual Conference of Metallurgists of CIM(COM 2000)*. 2000. p. 669-683.
84. Williams, J.G., C.R. Killmore, and G.R. Harris, *Recrystallisation Behaviour of Fine Grained Nb-Ti Austenite at Low Rolling Reductions*, in *THERMEC-88: International Conference on Physical Metallurgy of Thermomechanical Processing of Steels and Other Metals.* 1988. p. 224-231.
85. Hodgson, P.D., *The Metadynamic Recrystallization of Steels*, in *THERMEC 97: International Conference on Thermomechanical Processing of Steels and Other Materials*. 1997. p. 121-131.
86. Shaban, M. and B. Eghbali, *Characterization of Austenite Dynamic Recrystallization under Different Z Parameters in a Microalloyed Steel.* Materials Science and Technology, 2011. **27**(4): p. 359-363.
87. Elwazri, A.M., P. Wanjara, and S. Yue, *Metadynamic and Static Recrystallization of Hypereutectoid Steel.* ISIJ International, 2003. **43**(7): p. 1080-1088.
88. Cho, S.H., S.I. Kim, and Y.C. Yoo, *The Effects of Deformation Variables on Hot Workability of Austenitic Stainless Steel.* Metals and Materials International, 1998. **4**(4): p. 732-736.
89. Roberts, W., et al., *Prediction of Microstructure Development During Recrystallization Hot Rolling of Ti-V Steels*, in *Proceedings of the Technology and Applications of HSLA Steels*. 1983: Philadelphia. p. 67-84.
90. Choquet, P., et al., *Modelling of Forces, Structure, and Final Properties During the Hot Rolling Process on the Hot Strip Mill.* Mathematical Modeling of Hot Rolling of Steel, Canadian Institute of Mining and Metallurgy, Montreal, Canada, 1990: p. 34-43.
91. Hodgson, P.D., R.E. Gloss, and G.L. Dunlop, in *32nd Mechanical Working and Steel Processing Conference Proceedings*. 1991, ISS-AIME. p. 527.
92. Roucoules, C., *Dynamic and Metadynamic Recrystallization in High-Strength Low-Alloy Steels.* PhD Thesis, McGill University, Canada, 1992. .

93. Maccagno, T.M., J.J. Jonas, and P.D. Hodgson, *Spreadsheet Modelling of Grain Size Evolution During Rod Rolling.* ISIJ International, 1996. **36**(6): p. 720-728.

94. Ouchi, C., et al., *Microstructural Changes of Austenite During Hot Rolling and Their Effects on Transformation Kinetics.* The Hot Deformation of Austenite. AIME, New York, 1977: p. 316-340.

95. Hodgson, P.D., J.J. Jonas, and S. Yue, *Growth During and after the Static and Metadynamic Recrystallization of Austenite*, in *Materials Science Forum*. 1992, Trans Tech Publ. p. 715-722.

96. Uhm, S., et al., *Prediction Model for the Austenite Grain Size in the Coarse Grained Heat Affected Zone of Fe-C-Mn Steels: Considering the Effect of Initial Grain Size on Isothermal Growth Behavior.* ISIJ International, 2004. **44**(7): p. 1230-1237.

97. Sha, Q.Y. and Z.Q. Sun, *Prediction of Grain Growth of Coarse-Grained Austenite in Nb-V-Ti Microalloyed Steel.* Materials Science and Technology, 2011. **27**(9): p. 1408-1411.

98. LeBon, A.B. and L.N. deSaint-Martin, *Using Laboratory Simulations to Improve Rolling Schedules and Equipment*, in *Proc. Conf. on Microalloying 75*. 1977. p. 90-99.

99. Gladman, T. and D. Dulieu, *Grain-Size Control in Steels.* Metal Science, 1974. **8**(1): p. 167-176.

100. Lebon, A., J. Rofes-Vernis, and C. Rossard, *Recrystallization and Precipitation During Hot Working of a Nb-Bearing Steel.* Met. Sci., 1975. **9**(1): p. 36-40.

101. Davenport, A.T., R.E. Miner, and R.A. Kot, *The Hot Deformation of Austenite.* AIME, New York, 1977 p. 186–203.

102. Irvine, J. and T.N. Baker, *Effect of Rolling Deformation on Niobium Carbide Particle Size Distribution in Low-Carbon Steel.* Metal Science, 1979. **13**(3-4): p. 228-237.

103. Michel, J.P. and J.J. Jonas, *Precipitation Kinetics and Solute Strengthening in High Temperature Austenites Containing Al and N.* Acta Metallurgica, 1981. **29**(3): p. 513-526.

104. Bacroix, B., M.G. Akben, and J.J. Jonas, *Effect of Molybdenum on Dynamic Precipitation and Recrystallization in Niobium and Vanadium Bearing Steels.* Thesis (M. Eng.), McGill University, Canada, 1982: p. 293-318.

105. Akben, M.G., B. Bacroix, and J.J. Jonas, *Effect of Vanadium and Molybdenum Addition on High Temperature Recovery, Recrystallization and Precipitation Behavior of Niobium-Based Microalloyed Steels.* Acta Metallurgica, 1983. **31**(1): p. 161-174.

106. Jonas, J.J., *Mechanical Testing for the Study of Austenite Recrystallization and Carbonitride Precipitation.*, in *Proc. Int. Conf. on 'High strength low alloy steels'*, D.P. Dunne and T. Chandra, Editors. 1984: Wollongong. p. 80.

107. Jonas, J.J. and I. Weiss, *Effect of Precipitation on Recrystallization in Microalloyed Steels.* Metal Science, 1979. **13**(3-4): p. 238-245.

108. Weiss, I. and J.J. Jonas, *Interaction between Recrystallization and Precipitation During the High Temperature Deformation of High-Strength Low-Alloy Steels.* Metallurgical Transactions A, 1979. **10**(7): p. 831-840.

109. Dutta, B. and C.M. Sellars, *Effect of Composition and Process Variables on Nb(C, N) Precipitation in Niobium Microalloyed Austenite.* Materials Science and Technology, 1987. **3**(3): p. 197-206.

110. Irvine, K.J., F.B. Pickering, and T. Gladman, *Grain-Refined C-Mn Steels.* Journal of Iron and Steel Institute Journal, 1967. **205**: p. 161.

111. Siciliano, F., et al. *Modeling of Softening and Precipitation During the Hot Strip Rolling of Niobium Steels*. in *THERMEC 97: International Conference on Thermomechanical Processing of Steels and Other Materials*. 1997.

112. Hong, S.G., K.B. Kang, and C.G. Park, *Strain-Induced Precipitation of Nbc in Nb and Nb–Ti Microalloyed High-Strength Low-Alloy Steels.* Scripta Materialia, 2002. **46**(2): p. 163-168.

113. Stalheim, D.G. and D. G., *The Use of High Temperature Processing (H.T.P.) Steel for High Strength Oil and Gas Transmission Pipeline Applications.* Iron and Steel, 2005. **40**(S): p. 699-704.

114. McQueen, H.J., et al., *Hot Deformation and Processing of Aluminum Alloys*. 2011, Boca Raton: CRC Press.

115. Andrade, H.L., M.G. Akben, and J.J. Jonas, *Effect of Molybdenum, Niobium, and Vanadium on Static Recovery and Recrystallization and on Solute Strengthening in Microalloyed Steels.* Metallurgical Transactions A, 1983. **14**(10): p. 1967-1977.
116. Militzer, M., E.B. Hawbolt, and T.R. Meadowcroft, *Microstructural Model for Hot Strip Rolling of High-Strength Low-Alloy Steels.* Metallurgical and Materials Transactions A, 2000. **31**(4): p. 1247-1259.
117. He, X.L., et al., *The Non-Equilibrium Segregation of Boron During the Recrystallization of Nb-Treated High-Strength Low-Alloy Steels.* Acta metallurgica, 1991. **39**(10): p. 2295-2308.
118. Maruyama, N., R. Uemori, and M. Sugiyama, *The Role of Niobium in the Retardation of the Early Stage of Austenite Recovery in Hot-Deformed Steels.* Materials Science and Engineering: A, 1998. **250**(1): p. 2-7.
119. Bai, D.Q., et al., *Effect of Deformation Parameters on the No-Recrystallization Temperature in Nb-Bearing Steels.* Metallurgical and Materials Transactions A, 1993. **24**(10): p. 2151-2159.
120. Siciliano, F., L.L. Leduc, and K. Hensger, *The Effect of Chemical Composition on the Hot-Deformation Resistance During Processing of Microalloyed Steels in Thin Slab Casting/Direct Rolling Process*, in *Proc. of Inter. HSLA 2005 Conf.* 2005: Sanya (China).
121. Bruna, R. and F. Siciliano, in *Super High Strength Steels Int. Conf–November 2-4*. 2005: Rome, Italy.
122. Palmiere, E.J., C.I. Garcia, and A.J. Deardo, *Compositional and Microstructural Changes Which Attend Reheating and Grain Coarsening in Steels Containing Niobium.* Metall. Mater. Trans. A, 1994. **25**(2): p. 277-286.
123. San Martın, D., et al., *Austenite Grain Coarsening under the Influence of Niobium Carbonitrides.* The Japan Institute of Metals, 2004. **45**(9): p. 2797-2804.
124. Pereda, B., J.M. Rodriguez-Ibabe, and B. Lopez, *Improved Model of Kinetics of Strain Induced Precipitation and Microstructure Evolution of Nb Microalloyed Steels During Multipass Rolling.* ISIJ International, 2008. **48**(10): p. 1457-1466.

125. Herman, J.C., B. Donnay, and V. Leroy, *Precipitation Kinetics of Microalloying Additions During Hot-Rolling of High-Strength Low-Alloy Steels.* ISIJ International, 1992. **32**: p. 779.

126. Medina, S.F. and A. Quispe, *Improved Model for Static Recrystallization Kinetics of Hot Deformed Austenite in Low Alloy and Nb/V Microalloyed Steels.* ISIJ International, 2001. **41**(7): p. 774-781.

127. Zener, C. and J.H. Hollomon, *Effect of Strain Rate Upon Plastic Flow of Steel.* Journal of Applied Physics, 1944. **15**(1): p. 22-32.

128. Radovi, N. and D. Drobnjak, *Effect of Interpass Time and Cooling Rate on Apparent Activation Energy for Hot Working and Critical Recrystallization Temperature of Nb-Microalloyed Steel.* ISIJ International, 1999. **39**(6): p. 575-582.

129. Dutta, B., E.J. Palmiere, and C.M. Sellars, *Modelling the Kinetics of Strain Induced Precipitation in Nb Microalloyed Steels.* Acta Materialia, 2001. **49**(5): p. 785-794.

Appendix

Similar to deformation conditions of Steel B, presented in the discussion part, the full microstructural and MFS predictions for Steel A are given in this section. Generally, the MFS behavior for the two steels is very similar and the following results prove that the model can be applicable to different HSLA steels.

- **A-NTG-5**

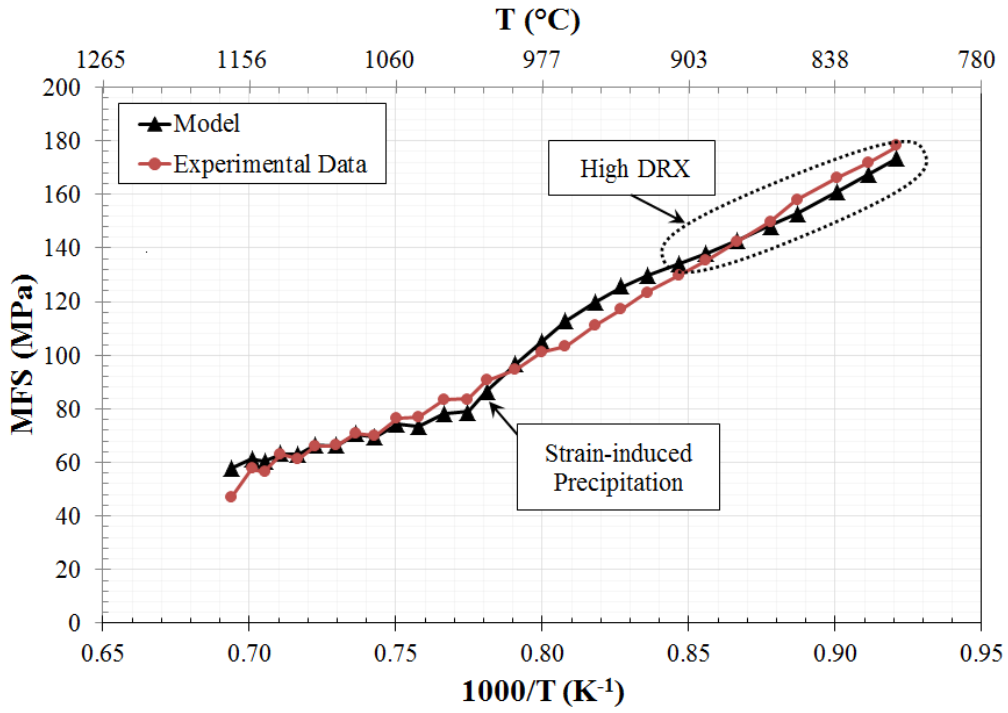

Figure A.1: MFS graph for A-NTG-5

Table A.1: Microstructural and MFS predictions for A-NTG-5.

Pass No.	T_{def} (°C)	t_{ip}	ε_a	ε_c	X_{DRX}	$[Nb]_{soln}$	Nb in C	X	d	1000/T	MFS (Model)	MFS (Torsion)
1	1168	5	0.20	0.30	0.00	0.053	0.000	0.81	57.2	0.694	57.9	47.0
2	1154	5	0.24	0.28	0.00	0.053	0.000	0.96	43.3	0.701	61.2	57.5
3	1145	5	0.21	0.28	0.00	0.053	0.000	0.80	30.8	0.705	60.4	56.4
4	1134	5	0.24	0.27	0.00	0.053	0.000	0.91	25.3	0.711	63.2	63.1
5	1122	5	0.22	0.27	0.00	0.053	0.000	0.74	19.2	0.717	63.1	61.4
6	1111	5	0.26	0.27	0.00	0.053	0.000	0.87	16.8	0.723	66.3	66.0
7	1097	5	0.23	0.27	0.00	0.053	0.000	0.61	12.5	0.730	66.2	66.2
8	1085	5	0.29	0.27	0.01	0.053	0.000	0.85	11.3	0.736	70.4	70.8
9	1073	5	0.24	0.27	0.00	0.053	0.001	0.52	8.6	0.743	69.5	70.1
10	1059	5	0.32	0.27	0.02	0.052	0.001	0.80	7.8	0.751	74.2	76.4
11	1047	5	0.26	0.28	0.00	0.052	0.002	0.47	6.1	0.758	73.6	76.8
12	1032	5	0.34	0.28	0.04	0.051	0.002	0.72	5.4	0.766	78.2	83.4
13	1017	5	0.29	0.28	0.00	0.051	0.008	0.26	4.2	0.775	79.0	83.7
14	1008	5	0.42	1.00	0.00	0.045	0.015	0.00	4.2	0.781	86.6	90.6
15	991	5	0.62	1.01	0.00	0.038	0.022	0.00	4.2	0.791	96.7	94.6
16	977	5	0.82	1.00	0.00	0.031	0.028	0.00	4.2	0.800	105.2	101.3
17	964	5	1.02	1.00	0.00	0.025	0.034	0.00	4.2	0.808	112.8	103.3
18	949	5	1.22	1.02	0.20	0.019	0.038	0.00	8.0	0.818	119.9	111.2
19	936	5	1.42	1.14	0.31	0.015	0.041	0.00	7.6	0.827	125.6	117.1
20	923	5	1.62	1.17	0.53	0.012	0.043	0.00	7.3	0.836	129.7	123.5
21	908	5	1.82	1.21	0.70	0.010	0.045	0.00	6.8	0.847	134.2	129.7
22	895	5	2.02	1.25	0.81	0.008	0.046	0.00	6.5	0.856	138.0	135.3
23	881	5	2.22	1.31	0.89	0.007	0.047	0.00	6.1	0.866	142.7	142.4
24	866	5	2.42	1.38	0.93	0.006	0.048	0.00	5.8	0.878	148.3	149.9
25	855	5	2.62	1.44	0.96	0.005	0.049	0.00	5.5	0.887	153.0	157.9
26	837	5	2.82	1.55	0.97	0.004	0.049	0.00	5.1	0.901	161.0	166.1
27	824	5	3.02	1.63	0.98	0.004	0.050	0.00	4.8	0.911	167.3	171.6
28	813	-	3.22	1.72	0.99	0.003	-	-	-	0.921	173.5	177.8

- **A-NTG-30**

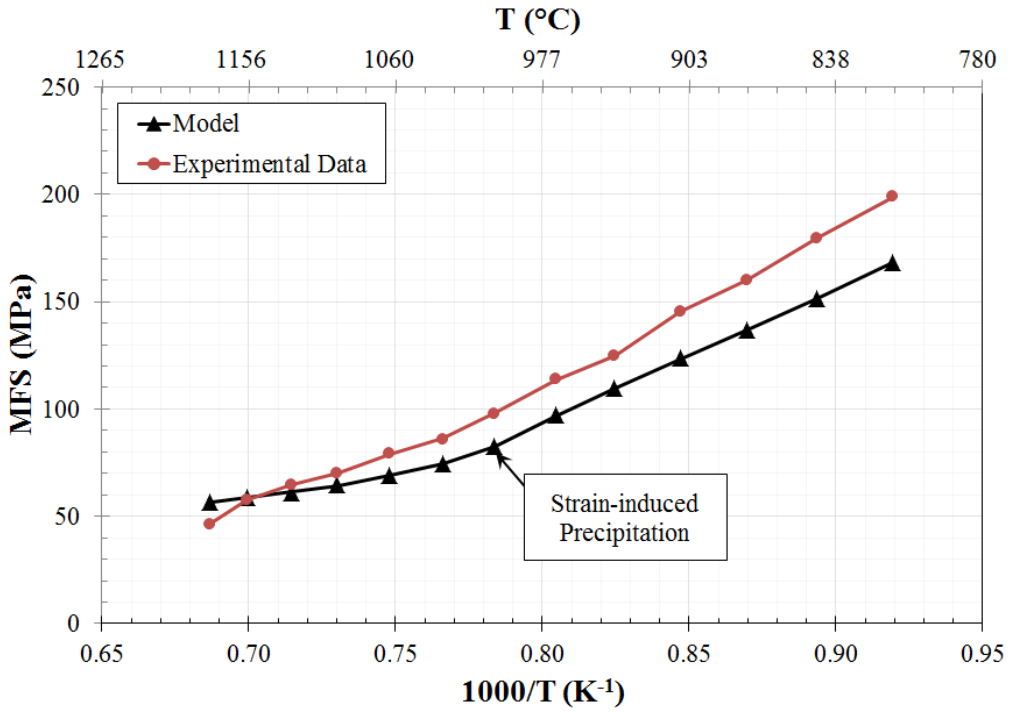

Figure A.2: MFS graph for A-NTG-30

Table A.2: Microstructural and MFS predictions for A-NTG-30.

Pass No.	T_{def} (°C)	t_{ip}	ε_a	ε_c	X_{DRX}	$[Nb]_{soln}$	Nb in C	X	d	1000/T	MFS (Model)	MFS (Torsion)
1	1182	30	0.20	0.29	0.00	0.053	0.000	1.00	123.4	0.687	56.8	46.6
2	1157	30	0.20	0.32	0.00	0.053	0.000	1.00	105.0	0.699	58.8	57.7
3	1127	30	0.20	0.33	0.00	0.053	0.000	0.99	73.1	0.714	61.4	64.6
4	1096	30	0.20	0.34	0.00	0.053	0.001	0.87	48.7	0.730	64.4	70.1
5	1064	30	0.23	0.35	0.00	0.052	0.002	0.79	31.5	0.748	69.2	79.1
6	1032	30	0.25	0.35	0.00	0.051	0.012	0.52	19.1	0.766	74.4	86.3
7	1003	30	0.32	1.23	0.00	0.041	0.024	0.00	19.1	0.784	82.4	98.1
8	970	30	0.52	1.27	0.00	0.029	0.033	0.00	19.1	0.805	96.9	113.6
9	939	30	0.72	1.33	0.00	0.020	0.040	0.00	19.1	0.825	109.9	125.1
10	907	30	0.92	1.45	0.00	0.013	0.044	0.00	19.1	0.847	123.3	145.7
11	877	30	1.12	1.60	0.00	0.009	0.046	0.00	19.1	0.870	137.0	160.0
12	846	30	1.32	1.82	0.00	0.007	0.048	0.00	19.1	0.893	151.7	179.4
13	815	-	1.52	2.12	0.00	0.005	-	-	-	0.919	168.2	198.8

- **A-TGH10-5**

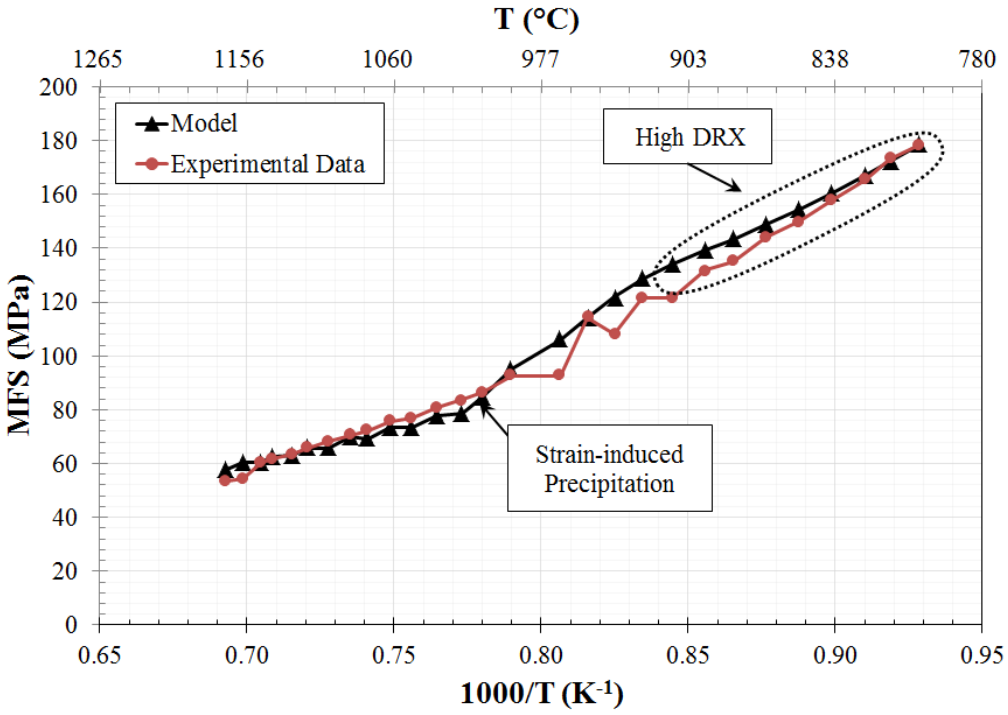

Figure A.3: MFS graph for A-TGH10-5

Table A.3: Microstructural and MFS predictions for A-TGH10-5.

Pass No.	T_{def} (°C)	t_{ip}	ε_a	ε_c	X_{DRX}	$[Nb]_{soln}$	Nb in C	X	d	1000/T	MFS (Model)	MFS (Torsion)
R01	1170	5	0.20	0.30	0.00	0.053	0.000	0.84	58.5	0.693	57.8	53.5
R02	1158	5	0.23	0.28	0.00	0.053	0.000	0.95	44.6	0.699	60.6	54.2
R03	1146	5	0.21	0.28	0.00	0.053	0.000	0.82	32.1	0.705	60.4	60.4
R04	1138	5	0.24	0.27	0.00	0.053	0.000	0.91	26.3	0.709	62.6	61.9
R05	1125	5	0.22	0.27	0.00	0.053	0.000	0.76	20.2	0.715	62.8	63.3
R06	1115	5	0.25	0.27	0.00	0.053	0.000	0.87	17.6	0.720	65.6	65.6
R07	1101	5	0.23	0.27	0.00	0.053	0.000	0.64	13.2	0.728	65.8	68.1
R08	1087	5	0.28	0.27	0.00	0.053	0.000	0.84	11.7	0.735	70.0	70.6
R09	1077	5	0.25	0.27	0.00	0.053	0.001	0.56	9.0	0.741	69.1	72.2
R10	1063	5	0.31	0.27	0.02	0.052	0.001	0.79	8.1	0.749	73.6	75.7
R11	1050	5	0.27	0.28	0.00	0.052	0.002	0.50	6.3	0.756	73.3	77.1
R12	1035	5	0.33	0.28	0.03	0.051	0.002	0.72	5.6	0.764	77.7	80.8
R13	1021	5	0.29	0.28	0.00	0.051	0.006	0.39	4.3	0.773	78.5	83.8
R14	1009	5	0.38	1.01	0.00	0.047	0.013	0.00	4.3	0.780	84.7	86.4
R15	993	10	0.58	1.01	0.00	0.040	0.023	0.00	4.3	0.790	95.1	92.7
F01	967	5	0.78	1.04	0.00	0.030	0.029	0.00	4.3	0.807	106.2	92.7
F02	953	5	0.98	1.05	0.00	0.024	0.034	0.00	4.3	0.816	114.3	114.3
F03	939	5	1.18	1.07	0.09	0.019	0.038	0.00	7.7	0.825	121.8	108.0
F04	925	5	1.38	1.19	0.19	0.015	0.041	0.00	7.3	0.834	128.6	121.8
F05	911	5	1.58	1.22	0.41	0.012	0.043	0.00	6.9	0.845	134.0	121.6
F06	896	5	1.78	1.27	0.59	0.010	0.045	0.00	6.5	0.856	139.2	131.9
F07	883	5	1.98	1.32	0.74	0.008	0.046	0.00	6.2	0.865	143.4	135.0
F08	868	5	2.18	1.39	0.83	0.007	0.047	0.00	5.8	0.876	148.7	144.2
F09	853	5	2.38	1.46	0.89	0.006	0.048	0.00	5.5	0.888	154.5	150.1
F10	839	5	2.58	1.55	0.93	0.005	0.049	0.00	5.1	0.899	160.7	158.2
F11	826	5	2.78	1.63	0.95	0.004	0.049	0.00	4.8	0.910	167.0	165.5
F12	816	5	2.98	1.70	0.97	0.004	0.050	0.00	4.6	0.919	172.2	173.2
F13	804	-	3.18	1.80	0.98	0.003	-	-	-	0.928	178.6	178.3

- **A-TGH20-5**

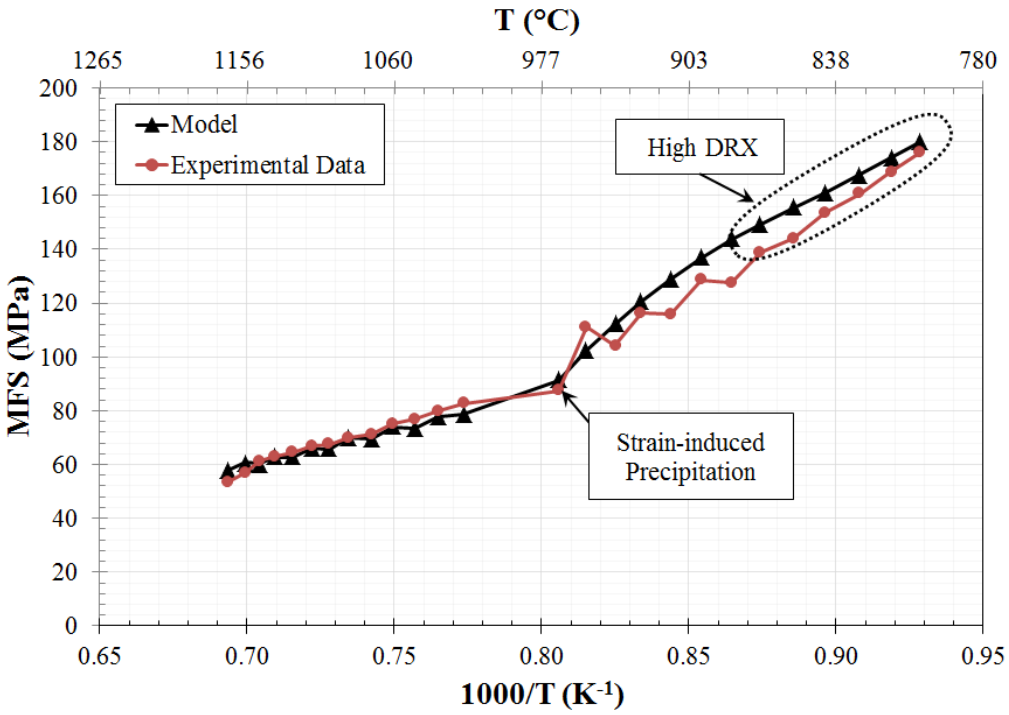

Figure A.4: MFS graph for A-TGH20-5

Table A.4: Microstructural and MFS predictions for A-TGH20-5.

Pass No.	T_{def} (°C)	t_{ip}	ε_a	ε_c	X_{DRX}	$[Nb]_{soln}$	Nb in C	X	d	1000/T	MFS (Model)	MFS (Torsion)
R01	1169	5	0.20	0.30	0.00	0.053	0.000	0.83	57.9	0.694	57.9	53.5
R02	1157	5	0.23	0.28	0.00	0.053	0.000	0.96	44.1	0.699	60.8	57.0
R03	1147	5	0.21	0.28	0.00	0.053	0.000	0.82	31.7	0.704	60.3	61.2
R04	1137	5	0.24	0.27	0.00	0.053	0.000	0.91	26.0	0.709	62.8	62.9
R05	1125	5	0.22	0.27	0.00	0.053	0.000	0.74	19.8	0.715	62.8	64.4
R06	1112	5	0.26	0.27	0.00	0.053	0.000	0.88	17.3	0.722	66.1	67.1
R07	1100	5	0.23	0.27	0.00	0.053	0.000	0.63	13.0	0.728	65.8	67.5
R08	1089	5	0.29	0.27	0.01	0.053	0.000	0.84	11.6	0.734	69.8	70.1
R09	1074	5	0.25	0.27	0.00	0.053	0.001	0.54	8.9	0.742	69.4	71.3
R10	1061	5	0.31	0.27	0.02	0.052	0.001	0.79	8.0	0.750	73.9	75.4
R11	1048	5	0.26	0.28	0.00	0.052	0.002	0.49	6.2	0.757	73.5	76.9
R12	1035	5	0.34	0.28	0.04	0.051	0.002	0.72	5.5	0.765	77.8	79.8
R13	1020	20	0.29	0.28	0.00	0.051	0.014	0.36	4.3	0.773	78.5	82.8
F01	968	5	0.39	1.12	0.00	0.039	0.021	0.00	4.3	0.806	91.4	87.4
F02	954	5	0.59	1.13	0.00	0.032	0.027	0.00	4.3	0.815	102.5	111.4
F03	939	5	0.79	1.14	0.00	0.026	0.032	0.00	4.3	0.825	112.0	104.0
F04	926	5	0.99	1.15	0.00	0.021	0.036	0.00	4.3	0.834	120.6	116.5
F05	912	5	1.19	1.18	0.00	0.017	0.039	0.00	4.3	0.844	128.9	115.8
F06	898	5	1.39	1.22	0.15	0.014	0.042	0.00	6.6	0.854	136.8	128.7
F07	884	5	1.59	1.36	0.24	0.011	0.044	0.00	6.2	0.864	143.8	127.8
F08	871	5	1.79	1.41	0.45	0.009	0.045	0.00	5.9	0.874	149.5	138.7
F09	856	5	1.99	1.48	0.60	0.008	0.046	0.00	5.5	0.885	155.5	144.2
F10	843	5	2.19	1.55	0.72	0.007	0.047	0.00	5.2	0.896	161.1	153.6
F11	828	5	2.39	1.64	0.80	0.006	0.048	0.00	4.9	0.908	167.7	160.8
F12	816	5	2.59	1.73	0.86	0.005	0.049	0.00	4.6	0.919	173.8	168.7
F13	804	-	2.79	1.82	0.91	0.004	-	-	-	0.929	179.9	176.4

- **A-TGH45-5**

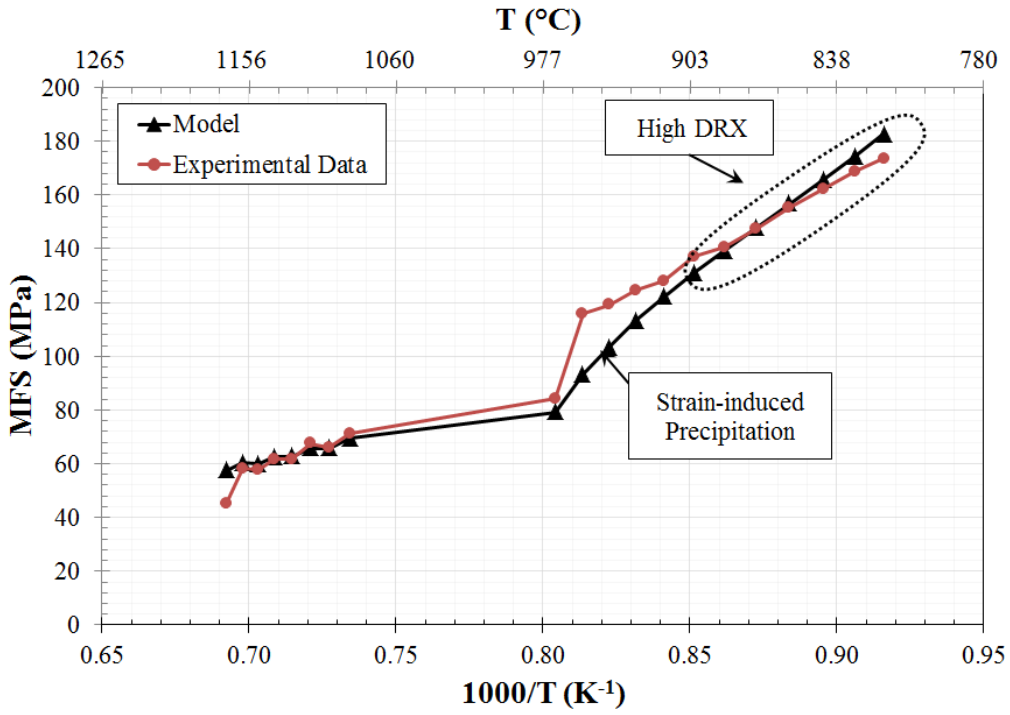

Figure A.5: MFS graph for A-TGH45-5

Table A.5: Microstructural and MFS predictions for A-TGH45-5.

Pass No.	T_{def} (°C)	t_{ip}	ε_a	ε_c	X_{DRX}	$[Nb]_{soln}$	Nb in C	X	d	1000/T	MFS (Model)	MFS (Torsion)
R01	1172	5	0.20	0.30	0.00	0.053	0.000	0.85	59.2	0.692	57.6	45.4
R02	1160	5	0.23	0.28	0.00	0.053	0.000	0.95	45.3	0.698	60.3	58.5
R03	1149	5	0.21	0.28	0.00	0.053	0.000	0.83	32.8	0.703	60.1	57.9
R04	1139	5	0.24	0.27	0.00	0.053	0.000	0.91	26.8	0.708	62.4	61.8
R05	1127	5	0.22	0.27	0.00	0.053	0.000	0.76	20.6	0.714	62.7	61.8
R06	1114	5	0.25	0.27	0.00	0.053	0.000	0.87	17.7	0.721	65.7	67.6
R07	1102	5	0.23	0.27	0.00	0.053	0.000	0.66	13.5	0.727	65.8	66.1
R08	1089	45	0.28	0.27	0.00	0.053	0.002	1.00	68.0	0.734	69.6	71.4
F01	971	5	0.20	0.47	0.00	0.051	0.002	0.09	59.0	0.804	79.2	84.2
F02	956	5	0.38	0.48	0.00	0.051	0.011	0.07	52.0	0.814	93.2	116.0
F03	943	5	0.56	1.84	0.00	0.042	0.020	0.00	52.0	0.822	103.4	119.1
F04	929	5	0.76	1.82	0.00	0.033	0.027	0.00	52.0	0.832	113.2	124.5
F05	916	5	0.96	1.82	0.00	0.026	0.032	0.00	52.0	0.841	122.2	128.1
F06	901	5	1.16	1.86	0.00	0.021	0.037	0.00	52.0	0.851	131.0	137.2
F07	887	5	1.36	1.91	0.00	0.016	0.040	0.00	52.0	0.862	139.5	140.7
F08	873	5	1.56	1.98	0.00	0.013	0.042	0.00	52.0	0.873	148.1	147.6
F09	858	5	1.76	2.08	0.00	0.011	0.044	0.00	52.0	0.884	156.8	155.4
F10	844	5	1.96	2.20	0.00	0.009	0.045	0.00	52.0	0.895	165.7	162.4
F11	831	5	2.16	2.32	0.00	0.008	0.046	0.00	52.0	0.906	174.4	168.7
F12	819	-	2.36	2.45	0.00	0.007	-	-	-	0.916	182.6	173.6

- **A-TGL10-5**

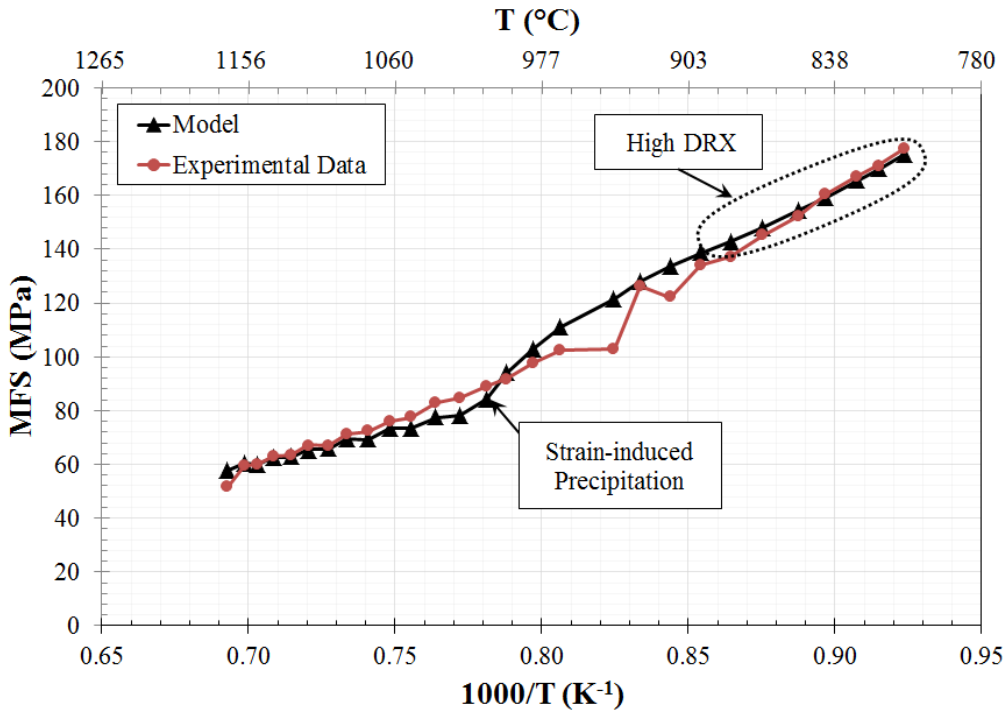

Figure A.6: MFS graph for A-TGL10-5

Table A.6: Microstructural and MFS predictions for A-TGL10-5.

Pass No.	T_{def} (°C)	t_{ip}	ε_a	ε_c	X_{DRX}	$[Nb]_{soln}$	Nb in C	X	d	1000/T	MFS (Model)	MFS (Torsion)
R01	1170	5	0.20	0.30	0.00	0.053	0.000	0.84	58.5	0.693	57.8	51.7
R02	1158	5	0.23	0.28	0.00	0.053	0.000	0.96	44.6	0.699	60.6	59.4
R03	1150	5	0.21	0.28	0.00	0.053	0.000	0.83	32.4	0.703	60.0	60.1
R04	1138	5	0.24	0.27	0.00	0.053	0.000	0.91	26.5	0.709	62.5	63.1
R05	1126	5	0.22	0.27	0.00	0.053	0.000	0.77	20.5	0.715	62.7	63.6
R06	1115	5	0.25	0.27	0.00	0.053	0.000	0.87	17.7	0.721	65.6	67.2
R07	1102	5	0.23	0.27	0.00	0.053	0.000	0.66	13.5	0.727	65.8	67.1
R08	1090	5	0.28	0.27	0.00	0.053	0.000	0.82	11.9	0.734	69.4	71.4
R09	1077	5	0.25	0.27	0.00	0.053	0.001	0.58	9.2	0.741	69.3	72.3
R10	1063	5	0.31	0.27	0.02	0.052	0.001	0.78	8.1	0.748	73.4	76.1
R11	1051	5	0.27	0.28	0.00	0.052	0.001	0.51	6.4	0.755	73.3	77.5
R12	1036	5	0.33	0.28	0.03	0.052	0.002	0.71	5.6	0.764	77.5	82.9
R13	1022	5	0.30	0.28	0.00	0.051	0.005	0.44	4.4	0.772	78.3	84.6
R14	1007	5	0.37	1.02	0.00	0.048	0.012	0.00	4.4	0.781	84.2	88.9
R15	996	5	0.57	1.01	0.00	0.041	0.020	0.00	4.4	0.788	94.2	91.9
R16	981	5	0.77	1.01	0.00	0.033	0.027	0.00	4.4	0.797	102.9	97.6
R17	967	10	0.97	1.02	0.00	0.026	0.034	0.00	4.4	0.807	111.0	102.5
F01	939	5	1.17	1.07	0.07	0.019	0.038	0.00	7.7	0.825	121.5	102.8
F02	926	5	1.37	1.19	0.18	0.015	0.041	0.00	7.3	0.834	128.2	126.5
F03	912	5	1.57	1.22	0.40	0.012	0.043	0.00	6.9	0.844	133.7	122.0
F04	897	5	1.77	1.26	0.59	0.010	0.045	0.00	6.6	0.854	138.6	134.2
F05	884	5	1.97	1.31	0.73	0.008	0.046	0.00	6.2	0.864	143.0	137.2
F06	870	5	2.17	1.38	0.83	0.007	0.047	0.00	5.9	0.875	148.1	145.2
F07	854	5	2.37	1.47	0.88	0.006	0.048	0.00	5.5	0.888	154.6	152.3
F08	842	5	2.57	1.53	0.93	0.005	0.049	0.00	5.2	0.897	159.4	160.5
F09	829	5	2.77	1.61	0.95	0.004	0.049	0.00	4.9	0.908	165.5	167.1
F10	820	5	2.97	1.67	0.98	0.004	0.050	0.00	4.7	0.915	169.7	171.3
F11	810	-	3.17	1.74	0.99	0.003	-	-	-	0.923	175.2	177.4

- **A-TGL20-5**

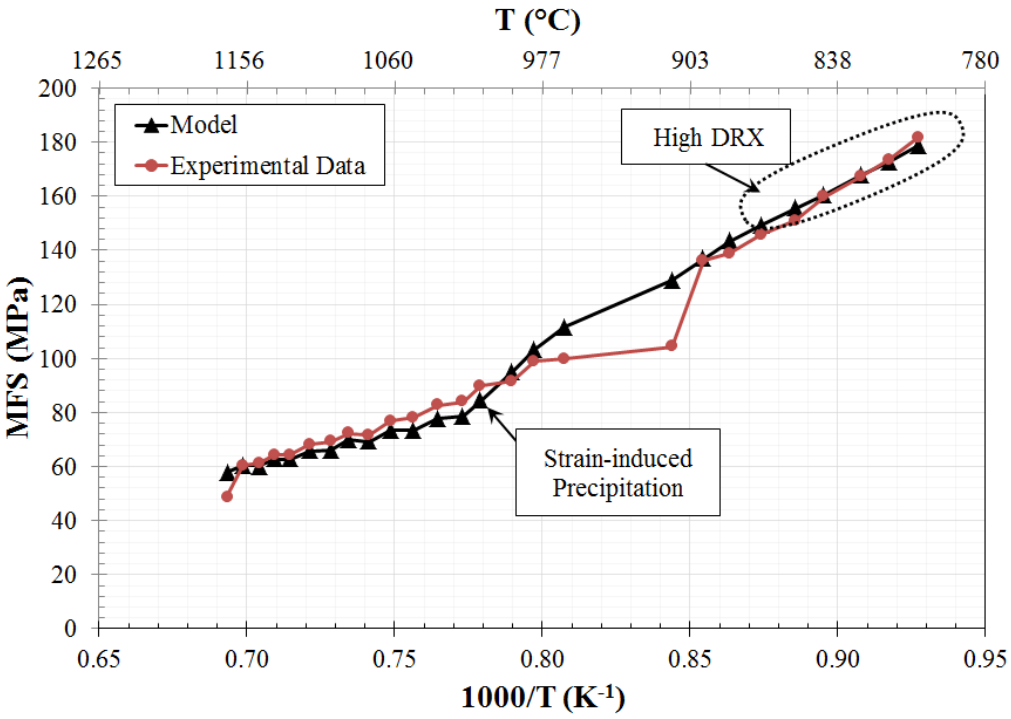

Figure A.7: MFS graph for A-TGL20-5

Table A.7: Microstructural and MFS predictions for A-TGL20-5.

Pass No.	T_{def} (°C)	t_{ip}	ε_a	ε_c	X_{DRX}	$[Nb]_{soln}$	Nb in C	X	d	1000/T	MFS (Model)	MFS (Torsion)
R01	1170	5	0.20	0.30	0.00	0.053	0.000	0.84	58.4	0.693	57.8	48.7
R02	1159	5	0.23	0.28	0.00	0.053	0.000	0.96	44.5	0.699	60.6	60.5
R03	1147	5	0.21	0.28	0.00	0.053	0.000	0.82	31.9	0.704	60.2	61.1
R04	1137	5	0.24	0.27	0.00	0.053	0.000	0.92	26.3	0.709	62.8	64.2
R05	1127	5	0.22	0.27	0.00	0.053	0.000	0.75	20.2	0.715	62.6	64.2
R06	1113	5	0.25	0.27	0.00	0.053	0.000	0.87	17.4	0.721	65.9	68.2
R07	1100	5	0.23	0.27	0.00	0.053	0.000	0.64	13.2	0.728	65.9	69.2
R08	1089	5	0.28	0.27	0.00	0.053	0.000	0.84	11.7	0.734	69.8	72.1
R09	1076	5	0.25	0.27	0.00	0.053	0.001	0.55	9.0	0.741	69.2	71.8
R10	1063	5	0.31	0.27	0.02	0.052	0.001	0.79	8.0	0.749	73.6	76.7
R11	1049	5	0.27	0.28	0.00	0.052	0.002	0.50	6.3	0.757	73.4	78.4
R12	1035	5	0.33	0.28	0.03	0.051	0.002	0.72	5.6	0.765	77.7	82.7
R13	1021	5	0.29	0.28	0.00	0.051	0.006	0.39	4.3	0.773	78.5	84.1
R14	1010	5	0.38	1.00	0.00	0.047	0.013	0.00	4.3	0.779	84.4	89.8
R15	993	5	0.58	1.02	0.00	0.040	0.021	0.00	4.3	0.790	95.1	91.8
R16	981	5	0.78	1.00	0.00	0.032	0.027	0.00	4.3	0.797	103.4	98.9
R17	965	20	0.98	1.01	0.00	0.026	0.036	0.00	4.3	0.807	111.6	99.8
F01	912	5	1.18	1.18	0.00	0.017	0.039	0.00	4.3	0.844	128.7	104.3
F02	897	5	1.38	1.23	0.14	0.014	0.042	0.00	6.6	0.854	136.7	136.5
F03	885	5	1.58	1.35	0.25	0.011	0.044	0.00	6.2	0.863	143.3	138.7
F04	871	5	1.78	1.41	0.44	0.009	0.045	0.00	5.9	0.874	149.5	145.8
F05	856	5	1.98	1.48	0.59	0.008	0.046	0.00	5.5	0.885	155.5	151.0
F06	844	5	2.18	1.54	0.72	0.007	0.047	0.00	5.2	0.895	160.6	159.9
F07	828	5	2.38	1.65	0.79	0.006	0.048	0.00	4.9	0.908	168.0	167.4
F08	817	5	2.58	1.71	0.87	0.005	0.049	0.00	4.6	0.917	172.9	173.5
F09	806	-	2.78	1.80	0.91	0.004	-	-	-	0.927	178.9	181.7

- **A-TGL45-5**

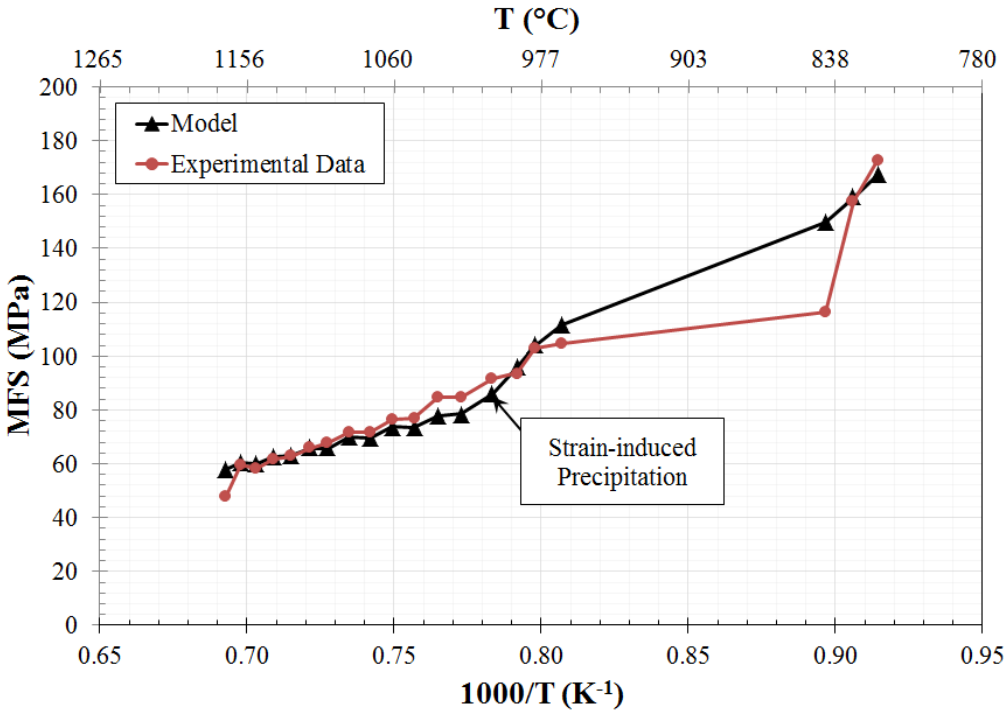

Figure A.8: MFS graph for A-TGL45-5

Table A.8: Microstructural and MFS predictions for A-TGL45-5.

Pass No.	T_{def} (°C)	t_{ip}	ε_a	ε_c	X_{DRX}	$[Nb]_{soln}$	Nb in C	X	d	1000/T	MFS (Model)	MFS (Torsion)
R01	1171	5	0.20	0.30	0.00	0.053	0.000	0.85	59.0	0.693	57.7	47.6
R02	1160	5	0.23	0.28	0.00	0.053	0.000	0.96	45.1	0.698	60.3	59.5
R03	1149	5	0.21	0.28	0.00	0.053	0.000	0.83	32.5	0.703	60.1	58.3
R04	1138	5	0.24	0.27	0.00	0.053	0.000	0.91	26.5	0.709	62.6	61.6
R05	1125	5	0.22	0.27	0.00	0.053	0.000	0.76	20.3	0.715	62.8	62.8
R06	1113	5	0.25	0.27	0.00	0.053	0.000	0.87	17.5	0.721	65.8	65.8
R07	1102	5	0.23	0.27	0.00	0.053	0.000	0.64	13.2	0.727	65.8	67.7
R08	1088	5	0.28	0.27	0.00	0.053	0.000	0.83	11.6	0.735	69.9	71.5
R09	1075	5	0.25	0.27	0.00	0.053	0.001	0.56	8.9	0.742	69.5	71.8
R10	1062	5	0.31	0.27	0.02	0.052	0.001	0.78	8.0	0.749	73.7	76.5
R11	1048	5	0.27	0.28	0.00	0.052	0.002	0.50	6.2	0.757	73.6	76.8
R12	1034	5	0.33	0.28	0.03	0.051	0.002	0.72	5.5	0.765	77.8	84.7
R13	1021	5	0.29	0.28	0.00	0.051	0.007	0.35	4.3	0.773	78.5	84.8
R14	1003	5	0.39	1.02	0.00	0.046	0.014	0.00	4.3	0.783	86.0	91.4
R15	990	5	0.59	1.02	0.00	0.039	0.021	0.00	4.3	0.792	96.1	93.7
R16	980	5	0.79	1.00	0.00	0.032	0.028	0.00	4.3	0.798	103.9	102.7
R17	966	45	0.99	1.00	0.00	0.025	0.038	0.00	4.3	0.807	111.8	104.8
F01	842	5	1.19	1.63	0.00	0.015	0.040	0.00	4.3	0.897	149.9	116.2
F02	831	5	1.39	1.69	0.00	0.013	0.042	0.00	4.3	0.906	159.0	157.4
F03	820	-	1.59	1.75	0.00	0.011	-	-	-	0.915	167.5	173.0